Table 1
Systems containing CO_2 and medium size components

2nd Component	T [K] range	P [bar] range	N	Ref.	PHCT		LCVM	
					$\Delta P\%$	$\Delta y \times 1000$	$\Delta P\%$	$\Delta y \times 1000$
Propane	274–344	7–62	45	[20]	1.1	7	0.6	6
n-Heptane	310–394	2–120	24	[20]	1.8	3	2.7	5
n-Octane	313–383	28–140	23	[21]	5.1	2	5.7	7
n-Decane	344–377	64–161	25	[22]	2.0	6	3.2	5
n-Hexadecane	463–664	20–51	44	[23]	1.1	7	10.2	35
Methylcyclohexane	311–477	4–149	31	[24]	5.1	18	7.7	11
Toluene	311–477	4–153	34	[20]	4.7	8	3.7	8
Ethylbenzene	308–328	14–84	18	[25]	5.5	1	3.3	1
Butylbenzene	273–293	10–30	14	[26]	21.2	–	19.0	–
Decaline	273–348	64–161	33	[26]	19.7	–	21.4	–

Table 2
Systems containing C_2H_6 with medium size components

2nd Component	T [K] range	P [bar] range	N	Ref.	PHCT		LCVM	
					$\Delta P\%$	$\Delta y \times 1000$	$\Delta P\%$	$\Delta y \times 1000$
n-Heptane	235–500	7–69	48	[20]	4.6	15	4.3	4
n-Octane	273–373	4–53	64	[20]	3.2	6	4.2	8
n-Decane	278–478	3–118	95	[20]	4.5	6	5.2	7
Methylcyclohexane	313–473	6–92	26	[27]	4.4	11	5.4	10
Propylcyclohexane	313–473	8–118	25	[27]	4.9	9	7.3	8
Benzene	273–533	21–83	79	[20]	1.7	9	2.1	5
Toluene	313–473	9–115	20	[27]	4.9	12	4.0	10
Propylbenzene	313–473	5–130	25	[27]	4.6	7	9.7	13
m-Xylene	313–473	5–120	27	[27]	4.8	11	5.3	12
Mesitylene	313–473	5–124	25	[27]	2.2	13	9.8	14

Table 3
Systems containing C_3H_8 with medium size components

2nd Component	T [K] range	P [bar] range	N	Ref.	PHCT		LCVM	
					$\Delta P\%$	$\Delta y \times 1000$	$\Delta P\%$	$\Delta y \times 1000$
n-Butane	353–413	21–40	30	[20]	1.7	10	0.5	10
n-Hexane	333–473	17–48	34	[20]	2.0	8	1.4	9
n-Decane	278–511	2–71	55	[20]	4.8	11	3.2	2
Methylcyclohexane	313–473	2–62	25	[27]	4.6	8	3.8	6
Propylcyclohexane	313–473	5–70	24	[27]	3.2	9	4.6	7
Benzene	311–478	1–59	73	[20]	2.5	11	4.9	12
Toluene	394–473	6–66	16	[27]	1.8	21	3.1	12
Propylbenzene	394–473	5–73	18	[27]	3.4	18	4.8	16
m-xylene	313–473	4–72	21	[27]	2.4	17	2.2	12
Mesitylene	313–473	4–74	21	[27]	2.5	16	3.2	13

Table 4
Prediction of the total liquid and vapor volumes (% deviations) for systems of CO_2 and *n*-alkanes

2nd Component	Ref.	PHCT		LCVM	
		$\Delta V^{Lo}\%$	$\Delta V^{Vo}\%$	$\Delta V^{Lo}\%$	$\Delta V^{Vo}\%$
Propane	[20]	1.8	3.1	1.4	2.3
n-Heptane	[20]	3.0	5.4	3.1	5.4
n-Octane	[21]	4.0	10.0	10.3	7.3
n-Decane	[22]	1.2	9.1	2.5	5.7

tion process involving petroleum cuts and natural products, is essential. Due to the complexity of the mixtures, which is very often in such cases, lack of experimental information is encountered. Therefore, in order to predict the phase behavior of such mixtures, fully predictive models are required. The pure component parameters should be known, either experimentally, or by using correlations or other predictive methods. The binary interaction parameters should also be known. Such models are the LCVM model [1] and the PHCT equation of state [2]. A comparison of the ability of these two models to predict the phase behavior of such systems is of great interest. The fact that the development of these two models is derived from completely different concepts makes this comparison even more interesting.

For the LCVM model, a predictive G^E model (UNIFAC-type models) has been incorporated into mixing rules expressions for the attractive parameter of cubic equation of state (EoS) and it allows description of VLE in complex systems through a simple EoS. The pure component parameters are estimated from the critical properties and the acentric factor (experimental or calculated from correlations). The binary interaction parameters that are used, either already exist (e.g. UNIFAC interaction parameter table), or new parameters are estimated from binary systems.

The PHCT EoS, considered in this work is based on the generalized van der Waals theory. The pure component properties are predicted from the molecular structure of the components of the mixture. The binary interaction parameters are

Table 5
System: CH_4/nC_{16} [28]

N	*T* [K] range	*P* [bar] range	x_2	$\Delta P\%$		
				PHCT	PR	LCVM
6	320	23–643	<0.2	–	6.21	3.7
7			>0.2	9.86	7.87	6.3
6	340	25–604	<0.2	–	>20	2.0
7			>0.2	13.21	8.52	4.2

Table 6
System: C_2H_6/nC_{16} [29]

N	*T* [K] range	*P* [bar] range	x_2	$\Delta P\%$		
				PHCT	PR	LCVM
2	320	8–69	<0.2	–	2.4	5.3
5			>0.2	10.1	7.1	6.1
2	340	10–92	<0.2	–	2.3	8.3
4			>0.2	4.8	6.9	1.6
2	360	12–114	<0.2	–	8.0	10.4
5			>0.2	4.6	8.9	0.9

Table 7
System: C_2H_6/nC_{20} [30]

N	T [K] range	P [bar] range	x_2	$\Delta P\%$		
				PHCT	PR	LCVM
6	320	3–74	<0.2	–	6.0	2.7
9			>0.2	4.3	10.9	4.2
6	340	3–106	<0.2	–	7.8	2.3
9			>0.2	5.0	11.0	3.8
4	360	15–133	<0.2	–	8.0	4.5
6			>0.2	6.2	8.5	2.1
2	400	21–168	<0.2	–	22.5	4.8
5			>0.2	6.0	8.8	2.2

Table 8
System: C_2H_6/nC_{22} [31]

N	T [K] range	P [bar] range	x_2	$\Delta P\%$		
				PHCT	PR	LCVM
8	320	7–69	<0.2	74.2	11.3	12.7
			>0.2	7.1	9.4	7.3
8	340	2–88	<0.2	39.6	11.8	11.1
			>0.2	7.6	12.9	4.6
7	360	3–93	>0.2	6.1	14.3	4.5

Table 9
System: C_2H_6/nC_{24} [32]

N	T [K] range	P [bar] range	x_2	$\Delta P\%$		
				PHCT	PR	LCVM
3	320	29–92	<0.2	–	19.9	4.2
2			>0.2	1.1	9.6	9.7
2	340	5–123	<0.2	–	17.1	14.7
5			>0.2	7.8	18.1	2.9

estimated from mixtures and they represent families of components, since they are defined as segment–segment interactions.

The common advantage of these two models is that the binary interaction parameters, which are essential for a correct prediction of the multicomponent phase behavior, can be calculated 'a priori' by knowing the functional groups of the components present in the mixture. Consequently, these two models can be used as powerful predictive tools in the study of the behavior of such complex mixtures.

Table 10
Systems of C_2H_6 with large *n*-alkanes

2nd Component	*T* [K] range	*P* [bar] range	Ref.	$\Delta P\%$		
				PHCT[a]	PR	LCVM
n-Hexadecane	320–360	8–114	29	6.8	7.1	4.5
n-Eicosane	320–400	3–168	30	5.1	10.0	3.3
n-Docosane	320–360	2–93	31	7.0	12.1	5.5
n-Tetracosane	320–340	5–123	32	4.2	13.2	4.8

[a] PHCT applies only in the far critical region ($x_2 > 0.2$)

2. Models

2.1. The LCVM model

Several equation of state/excess Gibbs energy (EoS/G^E) models have been proposed for the prediction of vapor–liquid equilibria. LCVM, [1], MHV2, [3] and PSRK, [4], [5] are three very successful models with wide range of applicability.

The main characteristic of these EoS/G^E models is that the mixing rule for the attractive parameter α of the EoS is derived by setting the expression for G^E, obtained from the EoS, equal to that from an existing G^E model. This method can be applied at infinite pressure [6], or at zero pressure [7,8]. Boukouvalas et al., [1] have developed a mixing rule that is a linear combination of the Vidal and Michelsen mixing rules. Of course, there is no need for specified reference pressure. The use of this mixing rule with the t-mPR EoS [9] and the Original UNIFAC [10] leads to the LCVM model studied here.

2.1.1. The equation of state

The EoS used is the translated and modified Peng–Robinson (t-mPR) EoS, [9]:

$$P = \frac{R\,T}{V + t - b} - \frac{a}{(V+t)\,(V+t+b)+b\,(V+t-b)} \quad (1)$$

The pure component parameter a is:

$$a = 0.45724\,\frac{R^2\,T_c^2}{P_c}\,f(T_r) \quad (2)$$

For non-polar compounds (gases and alkanes), $f(T_r)$ is related to the acentric factor ω:

$$f(T_r) = [\,1 + m\,(\,1 - \sqrt{T_r}\,)\,]^2 \quad (3)$$

$$m = 0.384401 + 1.52276\omega - 0.21380\omega^2 + 0.0346\omega^3 - 0.001976\omega^4 \quad (4)$$

Compared with the PR EoS using a single expression of $m = f(\omega)$, similar to Eqs. (1) and (4) provides similar overall vapor pressure (P^s) predictions, but better ones at low P^s levels. Additionally, it gives very good predictions of saturated liquid densities, especially for compounds with large ω values, through the introduc-

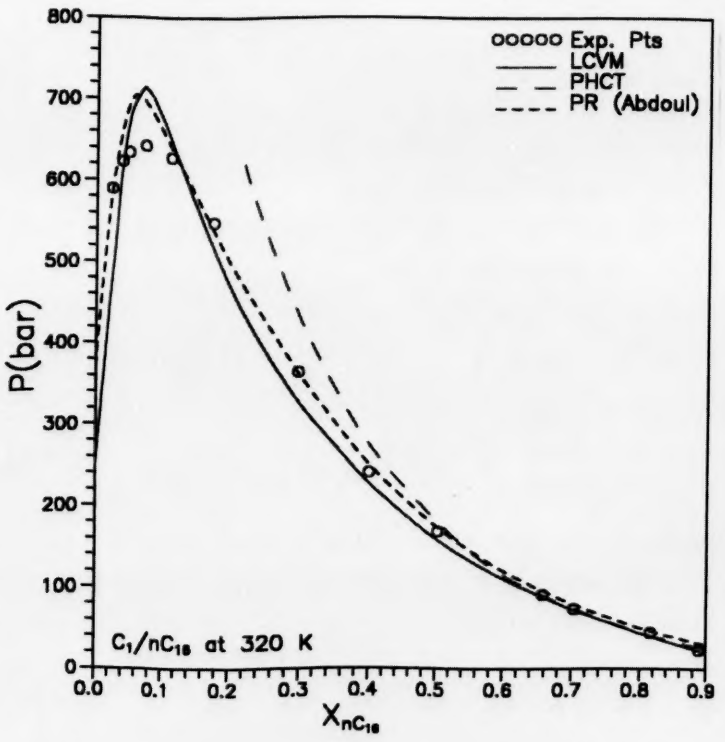

Fig. 1. Prediction of the phase behavior of CH_4/nC_{16} system at 320 K [28]; comparison between PHCT, LCVM and PR.

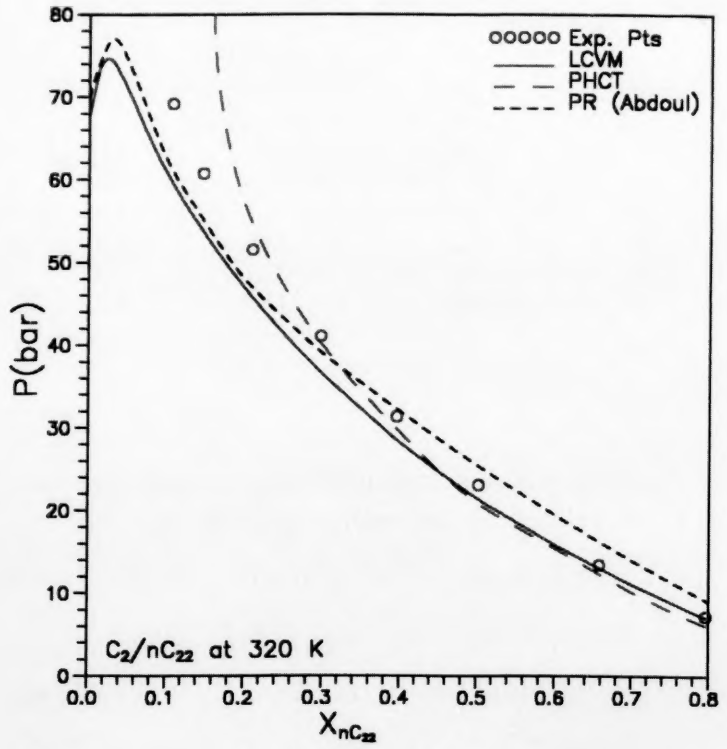

Fig. 2. Prediction of the phase behavior of C_2H_6/nC_{22} system at 320 K [30]; comparison between PHCT, LCVM and PR.

tion of the translation. The expression for translation t is given by Magoulas and Tassios [9]. The pure component parameter b is given by:

$$b = 0.0778 \frac{R\,T_c}{P_c} \tag{5}$$

2.1.2. The mixing rules

The mixing rule for the EoS parameter α ($=a/bRT$), is given by:

$$\alpha = \sum x_i\,\alpha_i + \left(\frac{\lambda}{A_V} + \frac{1-\lambda}{A_M}\right)\frac{G^E}{RT} + \frac{1-\lambda}{A_M}\sum x_i \ln\left(\frac{b}{b_i}\right) \tag{6}$$

with $\lambda = 0.36$, $A_V = -0.623$ and $A_M = -0.52$. For parameter b, the conventional linear mixing rule is used:

$$b = \sum x_i\,b_i \tag{7}$$

2.1.3. The G^E model

Original UNIFAC is used (in Eq. (6)), as it is a widely applicable G^E model, which is being updated and extended regularly. The interaction parameters used in this work, were taken from:

1. Hansen et al., [10], a recent revision of Original UNIFAC (temperature independent interaction parameters, $\Psi_{ij} = \exp\{-A_{ij}/T\}$), and
2. Voutsas et al., [13] (linear temperature dependency, $\Psi_{ij} = \exp\{-[A_{ij} + B_{ij}\cdot(T - 298.15)]/T\}$).

As demonstrated in previous publications [1,11–15] all models mentioned before present a comparable and very satisfactory behavior in the prediction of VLE in systems with components of similar size. The main application of EoS/G^E models, however, is in the prediction of high pressure VLE, where the presence of gases with medium to high molecular weight compounds (i.e. significant size difference) represents the typical case. In this case, LCVM yields very good results, while the other models perform poorly.

LCVM has been applied with considerable success to a variety of systems, such as:

- CO_2, CH_4, C_2H_6, C_3H_8, C_2H_4, N_2, H_2, H_2S with n-alkanes up to 44 carbon atoms and high pressures (up to 2000 bar).
- Other supercritical mixtures (e.g. gases with aromatics)
- Polar systems
- Multicomponent systems (ternary, gas condensates, oil systems, H_2S-rich sour natural gas, synthetic polydisperse mixtures)
- Solid–Fluid equilibria

2.2. The PHCT EoS

PHCT is an equation of state derived by Cotterman et al., [16,17] based on the generalized van der Waals theory. The model has been developed in terms of the Helmholtz function considering an attractive and a repulsive contribution. The former is made up of two terms, one for describing the high-density and one for the low-density region, the latter being based on a generalized form of the Carnahan–Starling equation. Dispersion and polar contributions to the free energy are considered in each part of the attractive term as

well as dipole and quadruple contributions. An interpolation function between the two limiting cases of a dense fluid and zero density fluid is included in the model based on empirical non-adjustable parameters. This modification of PHC theory improves agreement with experimental second virial coefficients, vapor pressures, and saturated liquid densities. Since all molecular parameters have a well-defined physical significance, they can be reliably estimated for high-molecular-weight-fluids where experimental data are scarce. More important, separation into low-density and high-density contribution allows separate mixing rules for each density region; this flexibility in mixing rules significantly improves representation of mixture properties. Detailed expressions about PHCT model are presented by Cotterman et al., [16,17].

The pure component parameters used, are predicted, on the basis of the molecular structure, by means of the generalized correlations given by Gregorovicz et al., [18]. A fine-tuning of the T^* parameter may be performed if at least a single vapor pressure datum is available.

The model includes at least three interaction parameters. One of them (that on the second virial term) becomes significant only at very low pressures, and, therefore, will be neglected in this investigation. The use of two unlike k_{ij}s is not justified by the different behavior in the two limiting regions for the systems investigated in this work, namely mixtures of hydrocarbons (non-polar) and supercritical gases. This reflects the symmetric situation of the two infinite dilution regions, which are typical for non-polar systems.

In conclusion, only one binary interaction parameter is used for a family of components, which accounts for the non-applicability of the random mixing in terms of segments making up the mixture (Fermeglia and Kikic, [2]). For polar systems at least two parameters are necessary.

This model has been applied successfully to systems:

- CO_2, C_2H_6 and C_3H_8 with medium size compounds (up to 10 carbon atoms), [2]
- CO_2, CH_4, C_2H_6 with *n*-alkanes up to 44 carbon atoms to the far-critical region, [17,19]

3. Results

The comparisons of these two models will be presented in two sections. In the first section, results for supercritical gases with medium size components will be presented. In the second one, results for supercritical gases with large *n*-alkanes will be presented.

3.1. Mixtures with light gases and medium size components

The supercritical gases are the CO_2, C_2H_6 and C_3H_8. The medium size components are alkanes (from 3 to 16 carbon atoms), methyl- and propylcyclohexane and aromatics (benzene, toluene, ethyl- and propylbenzene, *m*-xylene, mesitylene). The results that will be presented are VLE and volumetric predictions. Bubble point pressures predictions with LCVM and PHCT are presented in Tables 1–3. Volumetric predictions of these models are presented in Table 4.

The results, presented in these tables, show that both LCVM, and PHCT with interaction parameters from Fermeglia and Kikic, [2], perform very well, even in their predictions of the volumetric behavior. In general terms, PHCT is slightly better in bubble point pressure predictions than LCVM, but two points must be stressed out:

- LCVM interaction parameter have been obtained from correlation in the temperature range of 273–423 K. In some cases, it was necessary to extrapolate the use of these interaction parameters to higher and lower temperatures (from 234 up to 664 K). Although these results are not as good as the results obtained for the proper temperature range, they are also satisfactory and, therefore, the interaction parameters can be extrapolated for reasonable temperature range.
- All these systems have been used for the evaluation of the PHCT interaction parameters. On the other hand, for the evaluation of the LCVM interaction parameters only the gas/*n*-alkanes systems have been used. In the case of propane, the results with LCVM are straight predictions with the parameters suggested from

the Original UNIFAC revision by Hansen et al., [10].

3.2. Mixtures with light gases and large n-alkanes

In this section, the two models are compared in terms of VLE calculations for systems containing gases and large *n*-alkane. The gases are the CH_4, C_2H_6 and the *n*-alkanes are C_{16}, C_{20}, C_{22} and C_{24}. These results are presented in the Tables 5–10 and in the Fig. 1 and Fig. 2

In this case, the interaction parameters used with the PHCT are the parameters proposed by Cotterman et al., [17] and the results are also presented in the paper by Alessi et al., [33] under the model name of PHCT3. The comparison of these results showed that LCVM performs very well to all asymmetries and all pressures (see also concluded Table 10). On the other hand, PHCT's performance is not so straight. In the far critical region, the PHCT performs well, however, not better than LCVM. In the near critical region, the PHCT fails to give reliable results. This performance is well presented in Fig. 1 and Fig. 2. For comparison purposes, the performance of the PR EoS with conventional mixing rule (k_{ij}) is also presented in these figures. The interaction parameters used with PR EoS, were obtained by Abdoul et al., [34]. The behavior of PR EoS is very satisfactory and similar to the behavior of LCVM.

4. Conclusions

The performance of the LCVM model and the PHCT EoS is investigated in this work for binary systems of medium to large hydrocarbons with the light gases. The results indicated that the quality of their performance depends on the component size differences.

For systems with components of medium size difference, both models can be applied with significant success. No problem seems to exist in the prediction of the VLE, as well as the prediction of the volumetric behavior of such systems.

For systems with components of large size difference, in the far critical region, the general picture is almost the same. In this region, LCVM almost always predicts the behavior of the systems slightly better than PHCT. However, in the near critical region, PHCT fails to provide reliable results, or any results at all. On the other hand, LCVM behaves satisfactorily. As it is mentioned by Alessi et al., [33], it is hard for PHCT EoS to describe the retrograde condensation of natural gas. On the other hand, LCVM performs such calculations successfully enough as it is presented by Spiliotis et al., [11], Boukouvalas et al., [15].

Nomenclature

α	EoS attractive term (cohesion) parameter
b	EoS couolume parameter
G^E	Excess Gibbs free energy
T^*	Characteristic temperature (energetic pure component parameter)
k_{ij}	Binary interaction parameter

Table symbols

–	Vapor phase composition not available
x_2	Liquid concentration of component 2[mol.]
ΔV^L	Average absolute percent error in liquid volumes
ΔV^V	Average absolute percent error in vapor volumes
$\Delta P\%$	Average absolute error% in bubble- or dew-point pressure
$\Delta y \times 1000$	Average absolute error in vapor phase composition
N	Number of data points per system
Ref.	Reference number

References

[1] Ch. Boukouvalas, N. Spiliotis, P.H. Coutsikos, N. Tzouvaras, D. Tassios, Prediction of vapor–liquid equilibrium

with the LCVM model: a linear combination of the Vidal and Michelsen mixing rules coupled with the original UNIFAC and the t-mPR equation of state, Fluid Phase Equil. 92 (1994) 75.

[2] M. Fermeglia, I. Kikic, The perturbed hard chain theory for the prediction of supercritical fluid extraction: binary mixtures, Chem. Eng. Sci. 48 (1993) 3889.

[3] S. Dahl, Aa. Fredenslund, P. Rasmussen, The MHV2 model: a UNIFAC-based equation of state model for prediction of gas solubility and vapor–liquid equilibria at low and high pressures, Ind. Eng. Chem. Res. 30 (1991) 1936.

[4] K. Fischer, Die PSRK-methode: Eine Zustandsgleichung unter Verwendung des UNIFAC-Gruppenbeitradsmodells, VDI-Verlag, Düsseldorf, 1993.

[5] T. Holderbaum, J. Gmehling, PSRK: a group contribution equation of state based on UNIFAC, Fluid Phase Equil. 70 (1991) 251.

[6] J. Vidal, Mixing rules and excess properties in cubic equations of state, Chem. Eng. Sci. 33 (1978) 787.

[7] M.L. Michelsen, A method for incorporating excess Gibbs energy models in equations of state, Fluid Phase Equil. 60 (1990) 47.

[8] M.L. Michelsen, A modified Huron-Vidal mixing rule for cubic equations of state, Fluid Phase Equil. 60 (1990) 213.

[9] K. Magoulas, D. Tassios, Thermophysical properties of *n*-alkanes from C_1–C_{20} and their prediction for higher ones, Fluid Phase Equil. 56 (1990) 119.

[10] H.K. Hansen, P. Rasmussen, Aa. Fredenslund, M. Schiller, J. Gmehling, Vapor–liquid equilibria by UNIFAC group contribution. 5. Revision and extension, Ind. Eng. Chem. Res. 30 (1991) 2352.

[11] N. Spiliotis, Ch. Boukouvalas, N. Tzouvaras, D. Tassios, Application of the LCVM model to multicomponent systems: Extension of the UNIFAC interaction parameter table and prediction of the phase behavior of synthetic gas condensate and oil systems, Fluid Phase Equil. 101 (1994) 187.

[12] D. Apostolou, N. Kalospiros, D. Tassios, Prediction of gas solubilities using the LCVM Equation of State/excess Gibbs free energy model, Ind. Eng. Chem. Res. 34 (1995) 948.

[13] E. Voutsas, Ch. Boukouvalas, N. Kalospiros, D. Tassios, The performance of EoS/GE models in the prediction of Vapor–Liquid Equilibria in asymmetric systems, Fluid Phase Equil. 116 (1996) 480.

[14] I. Yakoumis, K. Vlachos, G. Kontogeorgis, Ph. Coutsikos, N. Kalospiros, F. Kolisis, D. Tassios, Application of LCVM model to systems containing organic compounds and supercritical carbon dioxide, J. Supercrit. Fluids 9 (1996) 88.

[15] Ch. Boukouvalas, K. Magoulas, S. Stamataki, D. Tassios, Prediction of vapor–liquid equilibria with the LCVM model: Systems containing light gases with medium and high molecular weight compounds, Ind. Eng. Chem. Res. 36 (1997) 5454.

[16] R. Cotterman, B. Schwarz, J. Prausnitz, Molecular thermodynamics for fluid at low and high densities. Part I: pure fluids containing small or large molecules, AIChE J. 32 (1986) 1787.

[17] R. Cotterman, J. Prausnitz, Molecular thermodynamics for fluid at low and high densities. Part II: Phase equilibria for mixtures containing components with large differences in molecular size or potential energy, AIChE J. 32 (1986) 1799.

[18] J. Gregorowicz, M. Fermeglia, G. Soave, I. Kikic, The perturbed hard chain theory for the prediction of supercritical fluid extraction: pure compound properties, Chem. Eng. Sci. 46 (1991) 1427.

[19] K. Gasem, R. Robinson, Evaluation of the simplified perturbed hard chain theory (SPHCT) for prediction of phase behavior of *n*-paraffins with ethane, Fluid Phase Equil. 58 (1990) 13.

[20] H. Knapp, R. Doring, L. Oelrich, U. Plocker, J. Prausnitz, Vapor–liquid equilibria for mixtures of low boiling substances. DECHEMA Chemistry Series, Vol. IV, Frankfurt/Main, 1986.

[21] M. King, D. Alderson, F. Fallah, D. Kassim, K. Kassim, J. Sheldon, R. Mahmud, Some vapor/liquid and vapor/solid equilibrium measurements of relevance for supercritical extraction operation, and their correlation, in: Chemical Engineering at Supercritical Conditions, Ann Arbor Science, Ann Arbor, MI, 1983.

[22] N. Nagarajan, R. Robinson, Equilibrium phase compositions, phase densities, and interfacial tensions for CO_2+ hydrocarbon systems. 2. CO_2 + n-decane, J. Chem. Eng. Data 31 (1986) 168.

[23] H. Sebastian, J. Simnick, H. Lin, W. Chao, Vapor–liquid equilibrium in binary mixtures of carbon dioxide + *n*-decane and carbon dioxide + *n*-hexadecane, J. Chem. Eng. Data 25 (1980) 138.

[24] H. Ng, D. Robinson, The equilibrium phase properties of selected naphthenic binary systems: carbon dioxide-methylcyclohexane, hydrogen sulfide-methylcyclohexane, Fluid Phase Equil. 2 (1979) 283.

[25] C. Tan, S. Yarn, J. Hsu, Vapor–liquid equilibria for the system carbon dioxide-ethylbenzene and carbon dioxide-styrene, J. Chem. Eng. Data 36 (1991) 23.

[26] D. Triffin, A. De Vera, K. Luks, J. Kohn, Phase Equilibrium Behaviour of the Binary Systems Carbon Dioxide-n-Butyl-benzene and Carbon Dioxide-trans-Decalin, J. Chem. Eng. Data 23 (1978) 45.

[27] D. Richon, S. Laugier, H. Renon, High-pressure vapor–liquid equilibria for binary mixtures containing a light paraffin and an aromatic compound or a naphthene in range 313–473 K, J. Chem. Eng. Data 36 (1991) 104.

[28] M. Glaser, C. Peters, H. van der Kooi, R. Lichtenthaler, Phase Equilibria of (methane + n-hexadecane) and (P, Vm, T) of *n*-hexadecane, J. Chem. Thermodyn. 17 (1985) 803.

[29] R. de Goede, C. Peters, H. van der Kooi, R. Lichtenthaler, Phase equlibria in binary mixtures of ethane and hexadecane, Fluid Phase Equil. 50 (1989) 305.

[30] C. Peters, J. de Roo, R. Lichtenthaler, Measurements and calculations of phase-equilibria of binary mixtures of ethane + eicosane. 1.vapor–liquid equilibria, Fluid Phase Equil. 34 (1987) 287.

[31] C. Peters, J. Spiegelaar, J. de Swan Arons, Phase-equilibria in binary-mixtures of ethane + docosane and molar volumes of liquid docosane, Fluid Phase Equil. 41 (1988) 245.

[32] C. Peters, H. van der Kooi, J. de Swan Arons, Measurements and calculations of phase-equilibria for (ethane + tetracosane) and (P, Vm-Star, T) of liquid tetracosane, J. Chem. Thermodyn. 19 (1987) 395.

[33] P. Alessi, M. Fermeglia, I. Kikic, E. Neau, Phase behavior prediction for binary volatile–nonvolatile mixtures of *N*-paraffins, J. Supercrit. Fluids 5 (1992) 151.

[34] W. Abdoul, E. Rauzy, A. Peneloux, Group contribution equation of state for correlating and predicting thermodynamic properties of weakly polar and non-associating mixtures, binary and multicomponents, Fluid Phase Equil. 68 (1991) 47.

ELSEVIER

Journal of Supercritical Fluids 19 (2001) 133–139

THE JOURNAL OF Supercritical Fluids

www.elsevier.com/locate/supflu

High-pressure solubility data of the system resveratrol (3) + ethanol (2) + CO_2 (1)

A. Berna *, A. Cháfer, J.B. Montón

Chemical Engineering Department, University of Valencia, 46100 Burjassot, Valencia, Spain

Received 14 February 2000; received in revised form 4 September 2000; accepted 15 September 2000

Abstract

Supercritical fluid extraction possesses several advantages over traditional liquid-solvent-based extraction methods, including improved selectivity, expeditiousness, automation and environmental safety. Fluid-phase equilibrium data are essential for studying the viability of supercritical extraction and the design of the extraction columns often used for this type of separation. Resveratrol has been correlated with serum lipid reduction and inhibition of platelet aggregation, and its cancer chemopreventive activity has recently been reported. The extraction of resveratrol using supercritical CO_2 is not possible; it only extracts traces of product, probably due to its polar nature. So, it is necessary to use a co-solvent. Ethanol is appropriate because it is a polar solvent permitted in the food industry. This work uses different mixtures of ethanol–CO_2, ranging from 5 to 15% of ethanol, to optimise the amount of resveratrol extracted. The solubility of resveratrol in the supercritical solvent was measured at 313 K and pressures ranging from 80 to 140 bar. In order to correlate the results obtained, two equations of state were successfully used (Peng–Robinson (PR) and Soave–Redlich–Kwong (SRK)). These equations show similar deviations, but PR shows a better correlation with experimental data. The solubility of resveratrol shows a maximum at an intermediate value of percentage of ethanol. It is roughly 7.5% of ethanol. So the optimal concentration of co-solvent was found. This solubility rises with pressure. © 2001 Elsevier Science B.V. All rights reserved.

Keywords: Carbon dioxide; Ethanol; Modelling; Resveratrol; Supercritical solubility

Nomenclature

a	parameter for cubic EOS (N m^4 mol^{-2})
b	parameter for cubic EOS (m^3 mol^{-1})
k_{ij}	binary interaction parameter in Eq. (3)
N	number of data in Eq. (5)
P	absolute pressure (Pa)

* Corresponding author. Tel.: +34-96-3864316; fax: +34-96-3864898.
E-mail address: angel.berna@uv.es (A. Berna).

0896-8446/01/$ - see front matter © 2001 Elsevier Science B.V. All rights reserved.
PII: S0896-8446(00)00088-7

R	universal gas constant (8.314 J mol^{-1} K^{-1})
T	absolute temperature (K)
v	mole volume (m^3 mol^{-1})
y	mole fraction

Greek letters

ω	acentric factor
η_{ij}	binary interaction parameter in Eq. (4)

Subscripts

c	critical property
i, j	component i, j respectively
cal	calculated results
exp	experimental data

1. Introduction

Supercritical fluids have been proposed for important application in the field of extraction, analysis, materials and reactions [1,2]. In fact, under proper conditions of pressure and temperature they have a liquid-like density and consequently quite good solvent properties. Supercritical fluid extraction presents several advantages over traditional liquid-solvent-based extraction methods [3–5], including improved selectivity, expeditiousness, automation and environmental safety. Selectivity can be significantly changed by varying both the pressure and temperature. The avoidance of organic solvents is a major goal in the isolation of natural products that may be commercialised as food additives. There are some companies in different countries that are already working with carbon dioxide extraction processes, especially in the food and pharmaceutical industries where the quality of a product is no less important than considerations of cost.

Phenolic compounds from plants are substances with the same metabolic origin; they are delivered from the shikimate pathway and phenylpropanoid metabolism [6]. The study of these compounds has gained special interest because of their pharmacological and, in some instances, cancer-preventive properties. Resveratrol has been correlated with serum liquid reduction and inhibition of platelet aggregation [7], and its cancer chemopreventive activity has recently been reported [8]. Phenolic compounds may be synthesised by plants for defence against microorganisms or strong UV radiation. For instance, t-resveratrol has been correlated with resistance to fungal infections [9,10].

t-Resvertatrol has been determined in wine, juices, berries and by-products of the grape-juice industry, including pomace, purees and seeds, by high performance liquid chromatography [11,12] and gas chromatography [13,14] in order to establish the amount of resveratrol incorporated into the human diet and to evaluate these by-products as potential ingredients in food [12]. A combination of geographical origin, variety, growing methods and winemaking procedures seems to affect the resveratrol concentration in wines and grape skin [10,11,14]. The content of t-resveratrol in berries steadily decreases during fruit ripening [13]. Grape skin is an important by-product of the wine industry. Now, it is used as animal food, but its possible use as a source of food ingredients in the human diet (as colourings, preservers or products with pharmacological interest as resveratrol) is being investigated.

High-pressure vapour–liquid equilibrium data for the CO_2 + resveratrol system are required for rational equipment design. There are some tests of supercritical extraction of resveratrol in the literature [15,16] that show the extraction of resveratrol using supercritical CO_2 was not possible. It only extracts traces of product. That is surely due to its polar nature. So, it is necessary to use a co-solvent. Ethanol is appropriate because it is a polar solvent permitted in the food industry.

This work has as its objective the determination of solubilities of resveratrol in a mixture of ethanol + CO_2. This is a preliminary step in the study of the viability of supercritical extraction of resveratrol from grape skin in order to increase its presence in wines or for pharmacological use. Also, this information is necessary in order to optimise the extraction operating conditions.

1.1. Models

In order to correlate the results obtained, two equations of state were tried: the Peng–Robinson equation of state (PR EOS) [17], Eq. (1), and the Soave–Redlich–Kwong (SRK EOS) [18], Eq. (2).

$$P = \frac{RT}{v-b} - \frac{a(T)}{v^2+2bv-b^2} \tag{1}$$

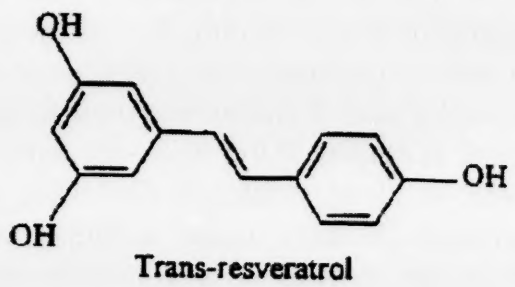

Fig. 1. Structure of resveratrol.

Table 1
Critical constants and acentric factor of pure components

Substance	T_c (K)	P_c (bar)	ω
CO_2	304.2[a]	73.7[a]	0.225[a]
Ethanol	513.92[a]	61.4[a]	0.644[a]
Resveratrol	893.8[b]	51.4[b]	0.961[c]

[a] Daubert and Danner [21].
[b] Estimated by the Ambrose method [22].
[c] Estimated by the Han and Peng method [23].

$$P = \frac{RT}{v-b} - \frac{a(T)}{v(v+b)} \tag{2}$$

where v is molar volume; a (a measure of intermolecular forces) and b (concerned with size of rigid spheres) are parameters of the equations, P is pressure, T is temperature and R is the universal gas constant.

The parameters were calculated by using the critical properties and the acentric factor of the pure components, and the following conventional mixing rules:

$$a_{ij} = \sqrt{a_i a_j}(1-k_{ij}) \tag{3}$$

$$b_{ij} = \frac{b_i + b_j}{2}(1-\eta_{ij}) \tag{4}$$

where a_i, a_j, b_i and b_j are the parameters for pure components (function of critical properties and the acentric factor), and k_{ij} and η_{ij} are binary adjustable interaction parameters.

2. Experimental section

2.1. Chemicals

Resveratrol (Fig. 1) (99 mass%, GC grade) was purchased from Aldrich Chemical Co., Inc. Ethanol absolute (99.8 mass%, GC grade) supplied by Prolabo S.A. was used as modifier and solvent to collect the extract. The reagents were used without further purification after chromatography failed to show any significant impurities. High-purity CO_2 (more than 99.9 vol% purity, SFC grade) was used as received. Calcined diatomaceous earth, extra pure (Scharlau Chimie S.A.), was utilised as a support for the products. The properties of the pure components are listed in Table 1.

2.2. Equipment and procedure

Solubilities were measured by an SFX 3560 Extractor with two Model 260D syringe pumps manufactured by ISCO (Lincoln, NE, USA). With the proper plumbing, the two-pump system can deliver modified supercritical fluid or a con-

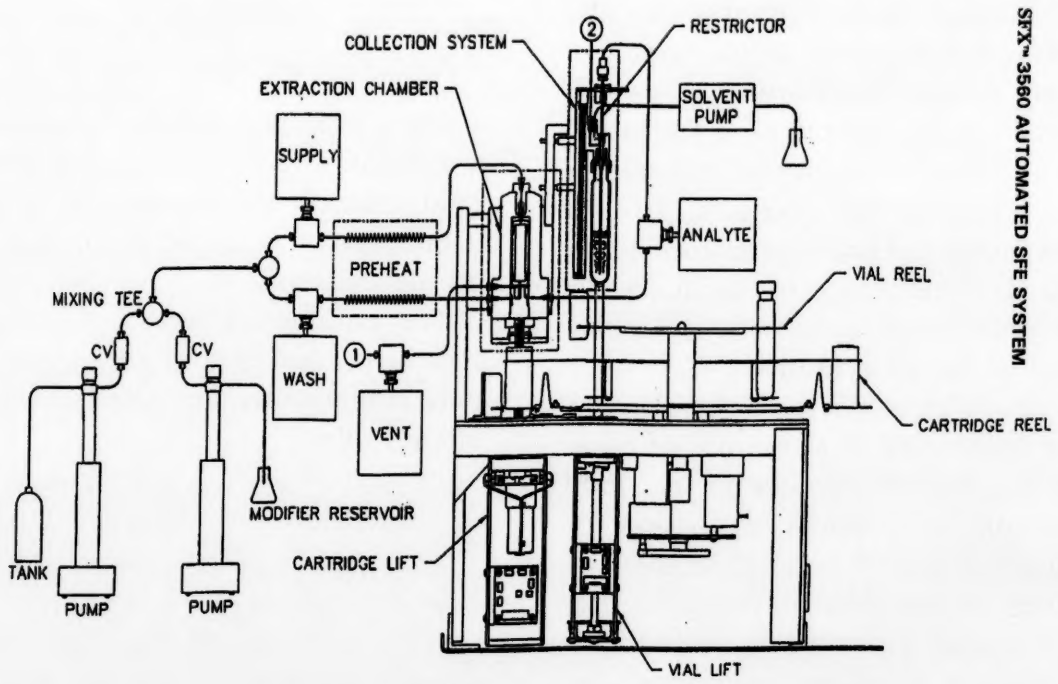

Fig. 2. Schematic diagram of SFX 3560. Supercritical fluid extraction system.

tinuous flow of supercritical fluid. The cylinder capacity of the pump is 266 ml and the maximum pressure 510 atm. The temperature can vary from 313.2 to 423.2 K, and the supercritical fluid flow between 0.5 and 5 ml/min. The SFX 3560 sample reel holds up to 24 sample cartridges and collection vials. The software supplied with the extractor employs a dynamic method programming scheme which allows entry changes to methods while a previously programmed method is running.

A schematic diagram of the apparatus is shown in Fig. 2. The sample cartridges with the product were placed in the cartridge reel, and the glass vials were taken up in the vial reel. Then the vial was raised, via a piston (vial lift), inside the collection system. Hence, the restrictor was inside the vial. After that, the cartridge lift raised the sample cartridge into the extraction chamber. Later, the vial was filled with the solvent, using the solvent pump, and simultaneously the extraction chamber was pressured with CO_2, via the supply valve and preheat. After a static time (30 s), the analyte valve was opened and the dynamic time started (4–8 min). During this time, the supercritical fluid flowed through the product in the sample cartridge. CO_2 was dissolved in the solvent (vial) to trap the product. The wash valve allows washing of the tubes, using supercritical CO_2, between the exit of the extraction chamber and vial. Finally, the vent valve was opened to decompress the extraction chamber.

The extractor measured the amount of supercritical CO_2 and modifier ethanol used during the extraction. The flow of supercritical fluid used in all experiments was 2 ml/min. This is the suitable flow to achieve the equilibrium with saturation of supercritical phase. Ethanol was used to trap the resveratrol extracted. After that, the extract was transferred to 10 ml calibrated flasks and diluted with ethanol. In some cases, a higher dilution was necessary to achieve a concentration level adequate for UV spectrometry determination.

For sample preparation, first 0.05 g of resveratrol was dissolved in 10 ml of ethanol. Second, 2 ml of solution was added of diatomaceous earth (1 g) previously weighed in the sample cartridge. Finally, the spiked solid was heated (60°C) for at least 2 h in order to evaporate ethanol and precipitate resveratrol over the surface of the solid particles. This procedure is necessary in order to avoid channelling during extraction and the formation of masses of particles.

An 8453 Hewlett-Packard diode array UV–VIS spectrophotometer was used for the determinations of resveratrol in the extract, after calibration with gravimetrically prepared standard solutions.

Solubility is measured as the slope of resveratrol moles extracted versus solvent moles (CO_2 + ethanol) at different extraction times.

3. Results and discussion

The extraction of resveratrol using supercritical CO_2 was tested. At extreme conditions of pressure and temperature it only extracts traces of product ($< 10^{-7}$ mole fraction), in accordance with Tena et al. [15]. This could be due to the polar nature of resveratrol. So, it is necessary to use a co-solvent. Ethanol is appropriate because it is a polar solvent and it is permitted in the food industry because it is harmless. Also, it is easily removed from the extract by evaporation at room temperature.

The solubilities of resveratrol in the supercritical phase were measured at 313 K, pressures ranging from 80 to 140 bar and for different mixtures of ethanol–CO_2. These results are shown in Table 2.

This study used different mixtures of ethanol–CO_2, ranging from 5 to 15% ethanol, in order to optimise the amount of resveratrol extracted with the minimal consumption of solvent. So, the extract is cleaner and the cost of the solvent and separation is smaller.

The composition of the supercritical phase was measured at 313 K. This is the minimum temperature allowed for the equipment. This figure has been selected in order to avoid the opposed effect of temperature on solubility [1].

The lower limit of 80 bar was appropriate because it was near of the CO_2 critical pressure, so the behaviour in conditions near the criticality of the system was studied. It was not possible to measure the solubility of resveratrol at pressures above 140 bar using this equipment because, at these conditions, the entire product contained in the sample cartridge was extracted.

In order to correlate the results obtained, two equations of state were successfully used: the PR EOS [17] and the SRK EOS [18]. The parameters of the equations of state were determined using the solver function of Microsoft Excel and the PE program [19]. These parameters and the average relative deviation (ARD) are shown in Table 3. The parameters estimation was performed considering all the experimental data by minimising the following objective function:

$$\mathrm{OF} = \sum\left(\frac{\mathrm{ABS}(y_{\mathrm{exp}} - y_{\mathrm{calc}})}{y_{\mathrm{exp}}}\right) \quad (5)$$

where y is the molar fraction of solute (resveratrol) in the supercritical phase.

Generally, both the PR EOS and the SRK EOS show similar deviations at different conditions of pressure and temperature, but the PR EOS [17] shows a better correlation with experimental points.

Table 2
Solubilities ($10^5 y_3$) of resveratrol expressed as mole fraction, in supercritical phase (CO_2 (1)+ethanol (2)) at 313 K and different percentages of modifier

P (bar)	Resveratrol solubility at % modifier (ethanol (2)) of:				
	5 ± 0.01	7.5 ± 0.01	10 ± 0.01	12.5 ± 0.01	15 ± 0.01
80 ± 0.1	4.64 ± 0.07	11.13 ± 0.02	9.31 ± 0.03	5.69 ± 0.07	4.14 ± 0.08
90 ± 0.1	5.41 ± 0.07	15.19 ± 0.02	12.14 ± 0.02	6.95 ± 0.06	5.10 ± 0.07
100 ± 0.1	6.33 ± 0.07	18.63 ± 0.02	15.08 ± 0.02	10.20 ± 0.03	5.94 ± 0.06
110 ± 0.1	7.35 ± 0.06	23.27 ± 0.01	19.72 ± 0.02	13.24 ± 0.04	7.59 ± 0.06
120 ± 0.1	8.47 ± 0.02		27.01 ± 0.02	19.07 ± 0.02	10.51 ± 0.05
130 ± 0.1	9.81 ± 0.02				13.66 ± 0.03
140 ± 0.1	11.24 ± 0.01				17.54 ± 0.02

Table 3
Parameters and deviations between experimental and calculated values of the system resveratrol (3)+ethanol (2)+CO_2 (1) for different equations of state at 313.15 K

Model	κ_{12}	κ_{13}	κ_{23}	η_{12}	η_{13}	η_{23}	ARD[a]
PR EOS	0.075	0.146	0.084	−0.063	−0.064	0.017	0.105
SRK EOS	0.019	0.020	0.020	−0.018	−0.018	0.197	0.116

[a] $\mathrm{ARD} = \left(\Sigma|y_{exp} - y_{cal}|/y_{exp}\right)/N.$

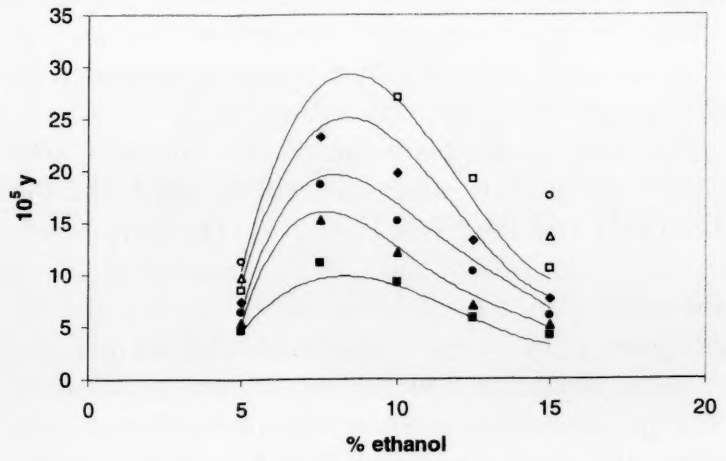

Fig. 3. Solubility y of resveratrol (3) versus ethanol (2) fraction at: (■) 80 bar, (▲) 90 bar, (●) 100 bar; (◆) 110 bar; (□) 120 bar, (△) 130 bar and (○) 140 bar. Modelling by PR EOS [17] shown by the line.

As is shown in Fig. 3, the evolution of the solubility of resveratrol versus the modifier fraction shows a maximum at roughly 7.5% ethanol. This concentration allows the amount of solvent in the extract to be small; in this way the separation process will be favoured. So the optimal concentration of co-solvent was founded. The existence of a maximum for the evolution of the solubility with co-solvent concentration has already been observed in the literature [20] in similar cases.

The solubility, as is shown in Table 2, rises with pressure. The extraction will be carried out at elevated pressure. The extraction pressure will be limited by operational costs and security cautions.

In conclusion, the present study reveals the influence of process conditions on the solubility of resveratrol in supercritical CO_2. It was necessary to use a co-solvent. Ethanol was an appropriate co-solvent and its optimal concentration was found to be about 7.5%. The solubility rises with pressure, so the extraction will be carried out at elevated pressure. Finally, the PR EOS [17] was applied successfully to the ternary system resveratrol–ethanol–CO_2.

Acknowledgements

The authors acknowledge CICYT for their financial support (project ALI97-1227-CO2).

References

[1] M.A. McHugh, V.J. Krukonis, Supercritical Fluid Extraction, Principles and Practice, Butterworths, Boston, 1986.
[2] E. Stahl, D. Gerard, Solubility behaviour and fractionation of essential oils in dense carbon dioxide, Perf. Flavor. 10 (1985) 29–37.
[3] G. Brunner, Gas Extraction, Springer, Berlin, 1994.
[4] J.C. Ely, J.K. Baker, A review of supercritical fluid extraction, N.B.S. Technical Note 1070, US Government Printing Office, Washington, 1983.
[5] D.F. Williams, Extraction with supercritical gases, Chem. Eng. Sci. 36 (11) (1981) 1769–1788.
[6] K. Robards, M. Antolovich, Analytical chemistry of fruit bioflavonoids. Review, Analyst 122 (1997) 11R–34R.
[7] H. Arichi, Y. Kimura, H. Okuda, K. Baba, M. Kozawa, S. Arichi, Studies on *Saitellariae radix*. VI. Effects of flavonone compounds on lipid peroxidation in rat liver, Chem. Pharm. Bull. 10 (1982) 218–220.
[8] M. Jang, L. Cai, G.O. Udecani, K.V. Slowing, C.F. Thomas, C.W.W. Beecher, H.H.S. Fong, N.R. Farnsworth, A.D. Kinghorn, R.G. Mehta, R.C. Moon, J.M. Pezzuto, Cancer chemopreventive activity of resveratrol, a natural product derived from grapes, Science 275 (1997) 218–220.
[9] L. Bavaresco, C. Fregoni, E. Cantu, M. Trevisan, Stilbene compounds: from the grapevine to wine, Drugs Exp. Clin. Res. 25 (2–3) (1999) 57–63.

[10] E. Revilla, E. Alonso, V. Kovac, The content of catechins and procyanidins in grapes and wines as affected by agroecological factors and technological practices, Wine 661 (1997) 69–80.
[11] K.D. McMurtrey, J. Minn, K. Pobanz, T.P. Schultz, Analysis of wines for resveratrol using direct injection high-pressure liquid chromatography with electrochemical detection, J. Agric. Food Chem. 42 (10) (1994) 2077–2080.
[12] B.J. Ector, J.B. Magee, C.P. Hegwood, M.J. Coign, Resveratrol concentration in muscardine berries, juice, pomace, seeds and wines, Am. J. Enol. Vitic. 47 (1996) 57–62.
[13] G.J. Soleas, D.M. Goldberg, E. Ng, A. Karumanchiri, E. Tsang, E.P. Diamandis, Comparative evaluation of four methods for assay of *cis*- and *trans*-resveratrol, Am. J. Enol. Vitic. 48 (1997) 169–176.
[14] D.M. Goldberg, J. Yan, E. Ng, E.P. Diamandis, A. Karumanchiri, G. Soleas, A.L. Waternouse, Direct injection gas-chromatographic–mass-spectrometric assay for *trans*-resveratrol, Am. J. Enol. Vitic. 46 (1995) 159–165.
[15] M.T. Tena, A. Rios, M. Valcarcel, Supercritical fluid extraction of *t*-resveratrol and other phenolics from a spiked solid, Fresnius' J. Anal. Chem. 361 (2) (1998) 143–148.
[16] M. Palma, L.T. Taylor, Statistical design for optimization of extraction of polyphenols from an inert matrix using carbon dioxide-based fluids, Anal. Chim. Acta 391 (3) (1999) 321–329.
[17] D. Peng, D.B. Robinson, A new two-constant equation of state, Ind. Eng. Chem. Fundam. 15 (1976) 59–64.
[18] G. Soave, Equilibrium constants from a modified Redlich–Kwong equation of state, Chem. Eng. Sci. 27 (1972) 1197–1203.
[19] O. Pfohl, St. Petkov, G. Brunner, Usage of PE. A Program to Calculate Phase Equilibria, Helbert Utz, 1998.
[20] A. Salvador, M.A. Jaime, M. De la Guardia, Study of chromatographic parameters for the supercritical fluid chromatography of benzodiazephines, Anal. Proc. (1995) 463–465.
[21] T.C. Daubert, R.P. Danner, Physical and Thermodynamic Properties of Pure Chemicals, Taylor & Francis, Washington, 1997.
[22] D. Ambrose, Vapour–liquid critical properties, National Physical Laboratory, Teddington, NPL Rep. Chem. 107, 1980.
[23] B. Han, D.Y. Peng, A group-contribution correlation for predicting the acentric factors of organic compounds, Can. J. Chem. Eng. 71 (1993) 332–334.

ELSEVIER

Journal of Supercritical Fluids 19 (2001) 141–148

THE JOURNAL OF Supercritical Fluids

www.elsevier.com/locate/supflu

Enzymatic alcoholysis of palm kernel oil in *n*-hexane and $SCCO_2$

D. Oliveira [a], J. Vladimir Oliveira [b,*]

[a] *Department of Food Engineering, URI-Erechim, 99700-000 Erechim, RS, Brazil*
[b] *Chemical Engineering Program, PEQ/COPPE/UFRJ, 21945-970 Rio de Janeiro, RJ, Brazil*

Received 21 October 1999; received in revised form 18 April 2000; accepted 6 June 2000

Abstract

The use of biocatalysts in supercritical CO_2 ($SCCO_2$) has received widespread attention in recent years. Biocatalysts have the advantage of substrate specificity under mild reaction conditions and $SCCO_2$ has several advantages over liquid solvents such as high solute diffusivities and low viscosity, which can accelerate mass transfer-limited enzymatic reactions. Concerning the enzymatic alcoholysis of vegetable oils, very little experimental data have been reported in the literature. Also, to the best of our knowledge, there is no comprehensive study available comparing conventional and supercritical media for this reaction. In this context, the main objective of this work is to compare enzymatic ethanolysis of palm kernel oil taking place in both $SCCO_2$ and in *n*-hexane as solvents. For this purpose, a Taguchi experimental design with two levels and four variables was adopted for each system to allow the investigation of the influence of process variables on the reaction conversion and on the enzyme activity. © 2001 Elsevier Science B.V. All rights reserved.

Keywords: Alcoholysis; Lipase; Experimental design; Supercritical CO_2; Reaction conversion

1. Introduction

Lipases have been extensively used in triglyceride technology, mainly for the biotransformation of oils and fats. Among several important processes for lipid modification are the hydrolysis reactions, synthesis of esters and transesterification of these materials, catalyzed by lipases. In these reactions the triglyceride reacts with a fatty acid (acidolysis), an alcohol (alcoholysis) or another ester (interesterification), resulting in a rearrangement of the triglyceride fatty acid groups to produce a new triglyceride as a consequence of the competitive hydrolysis and esterification reactions.

Esters obtained from alcohols and fatty acids have many important applications. For example, those from long chain acids (12–20 carbon atoms) and short chain alcohols (3–8 carbon atoms) have been widely employed in food, cosmetics and pharmaceutical industries [1]. Natural esters such as those from jojoba oil, carnauba wax and whale oil have also been used. However, these oils are

* Corresponding author. Fax: +55-21-5907135.
E-mail address: vladimir@peq.coppe.ufrj.br (J.V. Oliveira).

0896-8446/01/$ - see front matter © 2001 Elsevier Science B.V. All rights reserved.
PII: S0896-8446(00)00068-1

expensive, and they are not usually available in large quantities. Therefore, it is desirable to develop methods for the production of such esters using cheaper and more plentiful raw materials [2]. Among several Brazilian raw materials of interest in the production of high-value-added products, palm fruit is one of the most prominent. It is commonly used for the production of edible oil and the kernel oil is used in the manufacture of soaps. Though direct application of alkyl esters is scarce, they can be used as intermediates in the oleochemical production. Note that this product can also be used as biodiesel [3].

Several researchers have reported an alternative method to produce esters through enzymatic reactions using lipases as catalysts [4–10]. Because biocatalysts have high specific activity and a low impact on the environment, they have become increasingly important for industry. For example, immobilized lipases are used as catalysts for reactions involving biomodification of triglycerides [11]. In this case, supercritical fluids (SCF), particularly carbon dioxide, have currently received widespread attention as a possible medium for enzymatic reactions [12]. The main advantage of SCF over liquid solvents, such as *n*-hexane, is that the high diffusivity, low viscosity and low surface tension of SCF can speed up mass transfer-limited enzymatic reactions.

Nevertheless, enzymatic ethanolysis of vegetable oils has hardly been discussed in the literature. Furthermore, no comprehensive study comparing conventional and supercritical media has been reported for this type of reaction. In this context, our main objective is to provide a comparison between an organic liquid solvent and $SCCO_2$ for the enzymatic alcoholysis of palm kernel oil. For this purpose, a two-level Taguchi experimental design was adopted so as to investigate the influence of process variables, namely temperature (T), water and enzyme concentrations (denoted by [W] and [E], respectively) and oil/ethanol molar ratio (R) for *n*-hexane and temperature, water concentration, oil/ethanol molar ratio and pressure (P) for CO_2 system on the reaction conversion. The loss of enzyme activity for each experimental condition is also reported as well as the unusual effect of pressure on the initial reaction rate.

2. Materials and methods

2.1. Chemicals

Palm kernel oil was used as purchased without any pre-treatment. Fatty acid composition of palm kernel oil was determined using a gas chromatograph (HP 5890) with flame ionization detector. The following instrumentation and conditions were used: H_2 as carrier gas, modified polyethylene glycol column (FFAP 2–25 m × 0.20 mm i.d. × 0.30 μm film), column temperature: 180–210°C (2°C/min), injector temperature: 250°C and detector temperature: 280°C. The fatty acid composition in palm kernel oil was determined to be 9% caprylic acid, 47% lauric acid, 15% myristic, 9% palmitic acid and 20% oleic acid, resulting in an average molecular weight of the oil as 701.9 g/gmol. Ethyl alcohol and *n*-hexane, both analytical grade, were used as substrate and organic solvent, respectively. Carbon dioxide with purity higher than 99.99%, was used as solvent in the high-pressure reactions.

2.2. Enzymes

Two commercial immobilized lipases were kindly supplied by NOVO Nordisk Bioindustrial, Brazil (Araucária, PR): *Rhizomucor miehei* (Lipozyme IM) immobilized on a macroporous anion exchange resin (0.15 U/g, 4% water and diameter in the range of 0.2–0.6 mm) and *Candida antarctica* (Novozym 435) immobilized on a macroporous anionic resin (0.12 U/g, 1.4% water and diameter in the range of 0.3–0.9 mm). The optimum activities for both enzymes are achieved at 40–60°C for Novozym 435 and 30–70°C for Lipozyme IM (Novo Nordisk, Technical Report A-05948, 1992).

2.3. Analytical method

The glycerol content evolved during enzymatic alcoholysis was determined using the method described by Cocks and van Rede [13]. The reaction conversion was then calculated by determining the glycerol concentration assuming a maximum glycerol yield at the end of the reaction of 12% of the mass of oil [14].

Table 1
Process conversions obtained for the enzymatic alcoholysis of palm kernel oil in *n*-hexane

Exp.	Experimental conditions[a]				Conversion (%)	
	T (°C)	[E]	[W]	*R*	Lipozyme IM	Novozym 435
1	40	5	0	1:3	77.5	34.7
2	40	5	10	1:10	52.1	42.1
3	70	20	0	1:3	28.9	54.5
4	70	20	10	1:10	37.7	35.1
5	40	20	10	1:3	62.2	41.5
6	40	20	0	1:10	34.2	58.3
7	70	5	10	1:3	29.8	35.2
8	70	5	0	1:10	31.9	29.2
9	55	12.5	5	1:6.5	32.9	33.5

[a] [E], enzyme concentration, wt.% of substrates; [W], water concentration, wt.% of substrates; *R*, oil/ethanol molar ratio.

2.4. Apparatus and experimental procedure

2.4.1. Conventional solvent

The experiments were performed in stoppered 125-ml Erlenmeyer flasks. Lipase at pre-established concentrations was added to the mixture of oil (1 g)–ethanol and *n*-hexane (40 ml) and the flasks were agitated at 200 rev./min for 6 h in a controlled-temperature shaker. The organic solvent was chosen based on preliminary experiments with *n*-hexane and petroleum ether, which presented practically the same reaction conversion. The former solvent was then used as reaction medium due to its higher normal boiling point thus facilitating the experimental execution. The agitation level and the reaction time are suitable values obtained after a number of experimental tests. Indeed, an enhancement of these two operational variables meant negligible changes in observable conversions. A Taguchi experimental planning with two levels and four variables (temperature, water and enzyme concentrations and the oil/ethanol molar ratio) was adopted. The experimental planning, covering the variable ranges commonly employed in the literature [15], is presented in Table 1, columns 1 to 5. The experiments were accomplished randomly, and duplicate runs were carried out for each experimental condition resulting in a reproducibility better than 5%. The process conversion was then modeled by an empirical expression.

2.4.2. $SCCO_2$

The experimental set-up, as shown in Fig. 1, consists basically of a CO_2 cylinder, a high pressure pump (ISCO 260D), a liquid pump (Thermo Separation Products, model constaMetric 4100) and a 300-ml reactor (Autoclave Engineers, model 300BG) equipped with a mechanical stirrer (MagneDrive II), a heating mantle, an internal cooling loop, capable of keeping the temperature constant within 0.1°C, a pressure transducer and a sampling tube. Palm kernel oil at pre-established concentrations, enzyme (5 wt.% of substrates) and water (0–10 wt.% of substrates), were placed in the reactor. Afterwards, the reactor was closed, flushed and pressurized with CO_2. Before reaching

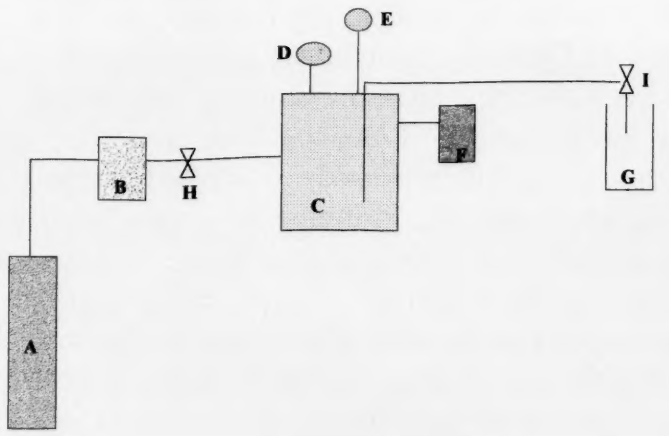

Fig. 1. Schematic diagram of the experimental apparatus: A, CO_2 cylinder; B, syringe pump; C, reactor; D, temperature controller; E, pressure transducer; F, liquid pump; G, cold trap; H, check valve; I, micrometering valve.

Table 2
Process conversions obtained for the enzymatic alcoholysis of palm kernel oil in $SCCO_2$

Exp.	Experimental conditions				Conversion (%)	
	T (°C)	P (bar)	[W]	R	Lipozyme IM	Novozym 435
1	40	73	0	1:3	7.7	54.5
2	40	73	10	1:10	16.7	63.2
3	70	200	0	1:3	11.9	24.7
4	70	200	10	1:10	14.2	35.4
5	40	200	10	1:3	11.7	14.1
6	40	200	0	1:10	25.4	21.3
7	70	73	10	1:3	15.5	12.1
8	70	73	0	1:10	18.4	42.9
9	55	136	5	1:6.5	26.4	20.4

the desired pressure, a pre-established amount of ethanol was fed into the reactor through the use of the metering liquid pump. The substrates and enzyme were then continuously mixed with an agitation level of 1000 rev./min in order to provide a proper homogenization of the reacting mixture. Moreover, it was experimentally observed that the degree of agitation did not affect sensibly the enzyme activity. The amount of allowable reactants were determined based on the phase equilibrium data from Bharath et al. [17] by performing simple approximate calculations so as to increase the liquid phase volume thus avoiding unnecessary ethanol charges and to permit reliable samplings — these data are reported elsewhere [16].

To assess the influence of process variables on the reaction conversion, the reaction time was set at 4 h. Typically, samples of approximately 2 ml were withdrawn after the reaction completion, or at the beginning of the reaction, and then analyzed using the previously described method. A Taguchi experimental design with two levels and four variables (temperature, water and enzyme concentrations and oil/ethanol molar ratio) was adopted. The experimental design along with the variable ranges is presented in Table 2, columns 1–5. Duplicate runs were made for all experimental conditions and the variations around the average values were typically about 3%. The process conversion was then modeled by empirical expressions.

3. Results and discussion

The experimental results using n-hexane and $SCCO_2$ are presented in Tables 1 and 2, respectively. One can see from these tables that the highest conversion (63.2%) in $SCCO_2$ was obtained using Novozym 435 as catalyst while in n-hexane Lipozyme IM provided the best achievement (77.5%). These results might be very important from an economic standpoint since a by-product can be used to produce high-value-added substances at near room temperature. Moreover, besides the good conversion obtained in $SCCO_2$, it might be relevant to call attention to the much lower expense of solvent in supercritical medium, 2 ml CO_2/g oil, compared with conventional solvent, 40 ml n-hexane/g oil.

From the results obtained in the experimental design, a standard statistical modeling technique, using the Statistica® software, was employed in constructing empirical models in order to evaluate the effect of process variables on the reaction conversion. The empirical models were built assuming that all variable interactions were significant, estimating the parameters related to each variable interaction and main variable effects and discarding the meaningless parameters by using the Student's t-test considering a confidence level of 95%. The objective of using the Student's t-test is to evaluate if the parameters were significantly different from zero. This test takes into account the S.D. of each parameter according to a well

known procedure available in many textbooks [18]. The parameters were estimated through the maximum likelihood method [19]. With regard to the parameter analysis, it is important to mention that a parameter with a negative value implies a negative effect of the variable on the process.

3.1. Conventional medium

It can be noticed from Table 3 that for the system containing Novozym 435, temperature, water and enzyme concentrations and also the cross interaction between temperature and oil/ethanol molar ratio significantly affect the process conversion. Though the optimum temperature for this enzyme is about 70°C, a negative effect is observed on the conversion. The added water also presented a negative effect, corroborating that water excess may change the reaction equilibrium, diminishing the formation of esters. As expected, the enzyme concentration, within the range studied, presented a positive effect on the conversion. Besides the isolated effects of these variables, cross interactions should also be taken into account, since cross interaction between temperature and oil/ethanol molar ratio had a negative effect on the conversion. It can be concluded that an excess of alcohol at higher temperatures leads to a decrease in conversion.

With regard to the system containing Lipozyme IM, temperature and oil/ethanol molar ratio have the most pronounced effects. Temperature presented a negative effect on the reaction conversion, the lowest value (40°C) being the condition in which the enzyme presents the best performance, according to the manufacturer. In this case, the enzyme concentration showed a negative effect on the reaction conversion. Table 3 also shows for this system that an excess of ethanol may inhibit the enzymatic reaction. It is also worth noticing the influence of the cross interactions on conversion, namely temperature–oil/ethanol molar ratio and temperature–enzyme concentration. The cross interactions are very important since from a practical standpoint the analysis of only isolated (main) effects may lead to unexpected/undesirable results.

3.2. $SCCO_2$

Based on the results obtained in conventional solvent, the first system investigated in $SCCO_2$ was the alcoholysis of palm kernel oil catalyzed by Lipozyme IM. However, by comparison of Tables 1 and 2, the conversions obtained in this case were, for all experimental conditions, lower than those obtained in a conventional solvent. For this system, it can be observed from Table 4 that the oil/ethanol molar ratio was the variable that more positively affected the process conversion. For the conventional medium, this was an expected result, since in supercritical medium, the ethanol is more susceptible to migrate to the gas phase. The cross interactions between tempera-

Table 3
Regression results ($\eta = a_0 + a_1T + a_2[E] + a_3R + a_4[W] + a_5T[E] + a_6TR$) for the system containing Novozym 435 and Lipozyme IM in *n*-hexane[a]

Novozym 435			Lipozyme IM		
Effect	Parameter	σ	Effect	Parameter	σ
–	(a_0) 41.03	0.46	–	(a_0) 43.89	1.00
T	(a_1) −3.15	0.41	T	(a_1) −12.05	1.12
[E]	(a_2) 6.01	0.56	[E]	(a_2) −3.23	0.87
R	(a_3) −0.09	0.56	R	(a_3) −5.07	1.10
[W]	(a_4) −2.66	0.53	[W]	(a_4) 1.39	0.94
T[E]	(a_5) 0.38	0.55	T[E]	(a_5) 4.69	1.10
TR	(a_6) −6.31	0.55	TR	(a_6) 8.09	1.10

[a] η, calculated conversion; σ, parameter S.D.

Table 4
Regression results for the system containing Novozym 435 and Lipozyme IM in $SCCO_2$

Lipozyme IM $\eta = a_0+a_1P+a_2R+a_3[W]+a_4TP+a_5TR+a_6PR+a_7T^2$			Novozym 435 $\eta = a_0+a_1T+a_2P+a_3R+a_4[W]+a_5TP+a_6TR+a_7T^2$		
Effect	Parameter	σ	Effect	Parameter	σ
–	(a_0) 24.27	0.54	–	(a_0) 20.12	1.58
P	(a_1) 0.61	0.19	T	(a_1) −2.39	0.55
R	(a_2) 3.48	0.19	P	(a_2) −11.29	0.55
[W]	(a_3) −0.66	0.19	R	(a_3) 4.83	0.55
TP	(a_4) −2.57	0.19	[W]	(a_4) −0.72	0.55
TR	(a_5) −2.19	0.19	TP	(a_5) 8.76	0.55
PR	(a_5) 0.51	0.19	TR	(a_6) 1.80	0.55
T^2	(a_7) −9.1	0.57	T^2	(a_7) 14.83	1.67

Table 5
Observed activity losses for the enzymatic alcoholysis of palm kernel oil in $SCCO_2$

Exp.	Experimental conditions				Loss of enzyme activity (%)	
	T (°C)	P (bar)	[W]	R	Lipozyme IM	Novozym 435
1	40	73	0	1:3	11.88	23.05
2	40	73	10	1:10	25.05	4.91
3	70	200	0	1:3	35.81	41.23
4	70	200	10	1:10	58.39	49.00
5	40	200	10	1:3	38.35	38.74
6	40	200	0	1:10	31.66	44.31
7	70	73	10	1:3	41.74	35.31
8	70	73	0	1:10	20.06	28.86
9	55	136	5	1:6.5	74.26	45.61

ture–pressure and temperature–oil/ethanol molar ratio also had a significant effect on the reaction conversion, both of them showing a negative effect. From this comparative study, it becomes clear that enzymes may exhibit different behaviors depending on the solvent medium and thereby affecting the process conversion.

In a second step, the same procedure was adopted using Novozym 435 as catalyst. After carrying out all the experiments, an empirical model was built for this system. It can be noted from Table 4 that the pressure was the variable that more strongly affected the process conversion, revealing that this variable has a negative effect on the conversion for this enzyme, probably causing enzyme activity loss. The oil/ethanol molar ratio also had a significant effect, similar to the Lipozyme IM. Temperature also presented a significant negative effect and hence an increase in this variable may lead to inactivation of the enzyme. The interaction between temperature and pressure also had an important effect on the conversion. Regarding the reaction conversion, as noted for *n*-hexane, different values have been recorded when using Lipozyme IM and Novozym 435 in $SCCO_2$.

While for the conventional medium no loss of enzyme activity was experimentally observed, the same was no longer valid for the $SCCO_2$ system. Steinberger and Marr [20] have recently pointed out that the stability of an enzyme in $SCCO_2$ depends on both its tertiary structure and on several parameters during exposure to high-pressure CO_2. They contend that high temperature,

the water content in CO_2 and pressurization/depressurization steps can cause enzyme inactivation. In fact, as presented in Table 5, in most of the experimental conditions considerable losses of enzyme activity have been observed. An attempt at explaining this is very difficult taking into account a complex reaction medium where many parameters are simultaneously involved. Thus, it seems difficult in this case to ascertain a relationship between enzyme activity and process conversions.

Another interesting aspect is the effect of pressure on the enzyme-catalyzed reactions in supercritical fluids. It has been observed by Cernia et al. [21] that the initial reaction rate generally exhibits an unusual behavior in the range of 6–25 MPa. This curious phenomenon was explored in this work using Novozym 435 as catalyst at the optimized values of process variables ($T = 40°C$, [W] = 0 and $R = 1{:}9.8$). As shown in Fig. 2, in the subcritical region a rise in pressure leads to a sharp increase in the reaction rate and then a gradual decrease at higher pressures. The rate of glycerol production rapidly increases from 13.09 (60 bar) and 16.08 (73 bar) up to 28.15 at 90 bar and then dramatically decreases to 6.66 at 200 bar. The fact that the initial rate of enzyme-catalyzed reactions is SCF is maximized near the solvent critical region has just been corroborated in the literature [21]. Though the role of $SCCO_2$ molecules during enzymatic reactions is far from understood, it has been argued that the pressure could induce modifications of both structure and function of enzyme leading to a change in the enzyme activity [21].

4. Conclusions

In this work, Lipozyme IM and Novozym 435 were used as catalysts in the ethanolysis of palm kernel oil in *n*-hexane and $SCCO_2$. The use of an experimental design for the production of esters from enzymatic reactions of vegetable oils proved to be a rational basis to assess the influence of process variables on the conversion. From this study one can verify that depending on the enzyme and solvent used, different results can be obtained. The main interest of this work lies in the fact that it is the first study comparing conventional and supercritical media for the alcoholysis of vegetable oils. From these results an investigation concerning the kinetics of the reaction in conventional and supercritical media can be carried out. Despite enzyme activity losses, $SCCO_2$ seems to be an appropriate solvent for enzymatic alcoholysis, very similar to an organic liquid solvent with regard to process conversion. Moreover, an advantage of supercritical fluids, considering the complete process, is that after the

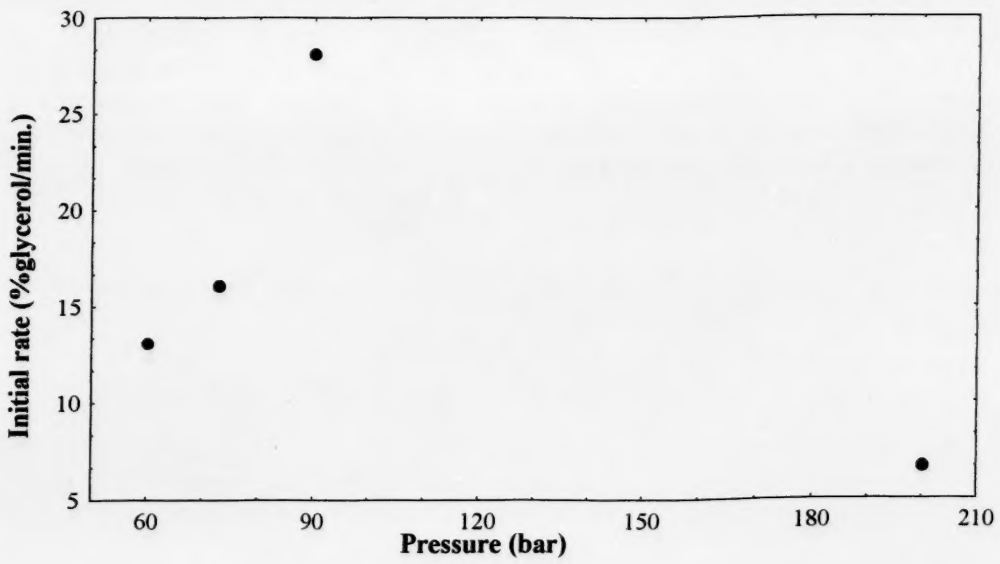

Fig. 2. Effect of pressure on the initial reaction rate of palm kernel oil catalyzed by Novozym 435 at $T = 40°C$, [W] = 0 and $R = 1{:}9.8$.

system depressurization, a mixture of products and non-reacted substrates may be obtained without traces of solvent.

Acknowledgements

The authors would like to thank FAPERJ and CNPq for financial support.

References

[1] G. Carta, J.L. Gainer, A. Zaidi, Fatty acid esterification using nylon immobilized lipase, Biotechnol. Bioeng. 48 (1995) 601.
[2] M. Martinez, E. Torrano, J. Aracil, An analogue of jojoba oil. A statistical approach, Ind. Eng. Chem. Res. 27 (1988) 2179.
[3] L.A. Nelson, T.A. Foglia, W.N. Marmer, Lipase catalyzed production of Biodiesel, J. Am. Oil Chem. Soc. 73 (1996) 1191.
[4] D.A. Abramowicz, C.R. Keese, Enzymatic transesterification of carbonates in water restricted environments, Biotechnol. Bioeng. 33 (1989) 149.
[5] E. Barzana, M. Karel, A.M. Klibanov, Enzymatic oxidation of ethanol in the gaseous phase, Biotechnol. Bioeng. 34 (1989) 1178.
[6] J.V. Brunt, Coaxing enzymes to act in organic solvents, Biotechnology 4 (1986) 611.
[7] J.S. Dordick, Enzymatic catalysis in monophasic organic solvents, Enzyme Microb. Technol. 11 (1989) 194.
[8] D.E. Stevenson, A.C. Storer, Papain in organic solvents: Determination of conditions suitable for biocatalysis and the effect on substrate specificity and inhibition, Biotechnol. Bioeng. 37 (1991) 519.
[9] T. Yamane, Importance of moisture content control for enzymatic reactions in organic solvents: A novel concept of microaqueous biocatalysis, Biocatalysis 2 (1988) 1.
[10] T. Yamane, T. Ichiryu, M. Nagata, A. Ueno, S. Shimizu, Intramolecular esterification by lipase in microaqueous benzene: Effect of moisture content, Biotechnol. Bioeng. 36 (1990) 1063.
[11] M. Basri, W.M.W. Yunus, C.N.A. Razak, A.B. Salleh, W.S. Yoong, Immobilization of lipase from *Candida rugosa* on synthetic polymer beads for use in the synthesis of fatty esters, J. Chem. Technol. Biotechnol. 66 (1996) 169.
[12] M. Habulin, V. Krmelj, Z. Knez, Alternative media for enzymatic reactions, in: A. Bertucco (Ed.), Proceedings of the 5th Conference on Supercritical Fluids and their Applications, Verona, Italy, 1999, p. 331.
[13] L.V. Cocks, C. van Rede, Laboratory Handbook for Oils and Fats Analysis, Academic Press, London, 1966.
[14] L.C. Monaco, Produção de Combustíveis Líquidos a partir de Óleos Vegetais, MIC/STI, 277, Brasília (in Portuguese), 1985.
[15] M. Mittelbach, Lipase catalyzed alcoholysis of sunflower oil, J. Am. Oil Chem. Soc. 67 (1990) 168.
[16] D. Oliveira, Estudo comparativo da produção enzimática de ésteres a partir de óleos vegetais em solvente orgânico e CO_2 supercrítico, D.Sc. Thesis (in Portuguese), PEQ/COPPE/UFRJ, 1999.
[17] R. Bharath, H. Inomata, T. Adschiri, K. Arai, Phase equilibrium study for the separation and fractionation of fatty acid oil components using supercritical carbon dioxide, Fluid Phase Equil. 81 (1992) 307.
[18] D.M. Himmelblau, Process Analysis by Statistical Methods, Wiley, New York, 1970.
[19] J.C. Pinto, F.B. Noronha, J.L. Monteiro, M.W. Lobão, T.J. Santos, ESTIMA: Um Pacote Computacional para Estimação de Parâmetros e Projeto de Experimentos, PEQ/COPPE/UFRJ (in Portuguese), 1987.
[20] D.J. Steinberger, T.G.R. Marr, Enzyme inactivation and prepurification effects of supercritical carbon dioxide, in: A. Bertucco (Ed.), Proceedings of the 5th Conference on Supercritical Fluids and their Applications, Verona, Italy, 1999, p. 339.
[21] E. Cernia, C. Palocci, E.C. Celia, S. Soro, Effect of pressure on enzymatic reactions in a supercritical fluid, in: A. Bertucco (Ed.), Proceedings of the 5th Conference on Supercritical Fluids and their Applications, Verona, Italy, 1999, p. 325.

ELSEVIER

Journal of Supercritical Fluids 19 (2001) 149–159

THE JOURNAL OF Supercritical Fluids

www.elsevier.com/locate/supflu

Mathematical modeling of extraction of egg yolk oil with supercritical CO_2

Weize Wu [a,*], Yucui Hou [b]

[a] *State Key Laboratory of Coal Conversion, Institute of Coal Chemistry, Chinese Academy of Sciences, Taiyuan 030001, People's Republic of China*

[b] *Biochemistry Department, Taiyuan Teacher College, Taiyuan 030001, People's Republic of China*

Received 8 March 2000; received in revised form 4 September 2000; accepted 15 September 2000

Abstract

Extraction of egg yolk oil (EYO) from egg yolk powder (EYP) with supercritical CO_2 was performed on a laboratory apparatus. Solubility of EYO in supercritical CO_2 was measured. The external diffusion and the equilibrium between solid and fluid phases were experimentally found to be the controlling steps during the extraction process. Based on this mechanism, a mathematical model for this extraction process was developed. The model parameters, adsorption equilibrium constant (k_p), EYO concentration in solid controlling the transition in the equilibrium (x_k) and the overall volumetric mass transfer coefficient ($K_f a_p$), were obtained by simulation. The simulation results indicated that x_k is 0.56, $K_f a_p$ is directly proportional to CO_2 flow rate with an exponent of 0.548, and the adsorption heat of EYO is 6–9 kJ mol^{-1}. The model was verified by concentration profiles of solid. The extraction process of EYO with supercritical CO_2 was conducted on a pilot plant and the developed model could predict satisfactorily the process. © 2001 Elsevier Science B.V. All rights reserved.

Keywords: Extraction; Supercritical CO_2; Egg yolk oil; Mathematical model

1. Introduction

Egg yolk powder (EYP) contains abundant phospholipid, which is of high value in food, medicine and cosmetics. It also contains cholesterol, glyceride, phospholipid, protein and moisture. The high level of cholesterol in EYP is the major problem that limits the EYP application [1]. Therefore it is important to remove cholesterol before obtaining high purity phospholipid. Traditionally phospholipid is extracted from EYP with organic solvent, such as acetone, ethanol and hexane [2]. However, this method has its inevitable disadvantages such as organic solvent residues in products and degeneration of active components by the required high temperature.

Recently, supercritical carbon dioxide (SC-CO_2) extraction is applied in separation of EYP [3–6]. In this process, cholesterol, glyceride and moisture, called egg yolk oil (EYO), are dissolved in

* Corresponding author. Tel.: +86-351-4048571; fax: +86-351-4050320.

E-mail address: wzwu@ms.sxicc.ac.cn (W. Wu).

0896-8446/01/$ - see front matter © 2001 Elsevier Science B.V. All rights reserved.

PII: S0896-8446(00)00089-9

SC-CO_2, and phospholipid and protein, called 'matrix', leave in the solid phase. Using this technique, Froning et al. [3] and Hung et al. [4] reported cholesterol removal efficiency of about 70% and Wu et al. [5] achieved a complete separation under optimal separation conditions of 55°C and 28–36 MPa. The merits of this method are not only avoiding disadvantages mentioned in organic solvent extraction, but also not impairing the functional properties and taste of EYP [3,4]. Hence this technology has potential application in commercial plant. Up to now, no model has been built for SC-CO_2 extraction of EYO from EYP. Therefore it is necessary to study the mass transfer mechanism and to build a mathematical model for this process.

A few models had been established for supercritical fluid extraction (SFE) of other materials. For building models, different mass transfer mechanisms had been hypothesized and most models proposed were built on different mass balance integration. Lee et al. [7], Bulley et al. [8] and Fattori et al. [9] assumed that mass transfer resistance occurred only in fluid phase when they set up models of SC-CO_2 extraction of canola seed oil. Reverchon et al. [10,11] found that the controlling step was the internal diffusion in solid phase during extraction of herbaceous essence and sage oil. Roy et al. [12] made a distinction in solid phase between broken cells and intact cells, which were considered with different mass transfer resistance: when extracting oil in broken cells the resistance occurred in fluid phase and when in intact cells it did in solid phase. An extraction model with a shock transition concentration and variable mass transfer resistance was proposed for fractionation of flower concrete using SC-CO_2 [13]. Roy et al. [14] adopted the shrinking core model for extraction of ginger oil. Desorption equilibrium was considered as the limiting step during SC-CO_2 extraction of essential oils [15]. Based on above reviews, different models were built for SFE from different materials.

The objectives of this work are: (1) to study the mass transfer mechanism of SC-CO_2 extraction of EYO from EYP; (2) to build a mathematical model for this process; and (3) to verify the model and to apply it to a pilot plant.

2. Experimental

2.1. Materials

EYP, obtained from Beijing International Egg Products, contains EYO of 43.3 wt.%. EYP was stored in a refrigerator and was extruded into three grades of bars with diameters of 1.2, 2.0, and 3.0 mm, respectively, before fed into extractor. CO_2, bought from Shanxi fertilizer factory, China, has a purity of more than 99%.

2.2. Experimental apparatus

The experimental apparatus is shown in Fig. 1, which mainly consists of an extractor (E) and two separators (S1, S2). The extractor is 4.4×10^{-2} m in diameter and 1.2×10^{-3} m^3 in volume. Each of the two separators in series, with a volume of $0.5 \times 10^{-3} m^3$, has a conical bottom connected with a regulating valve. A high-pressure plunger pump (PU) (Benxi water pump factory, Benxi China) is equipped for operating at pressure up to 40 MPa and at CO_2 delivering flow up to 15 kg h^{-1}. The flow rate of CO_2 was controlled by adjusting the pump speed and monitored by an electronic high-pressure rotameter (R) (Beijing forth automation meter factory, Beijing, China). Pressures in extractor and separators were controlled by means of manually adjusted micrometering valves (Funing Gauge and Valve Factory, Funing, China). Temperatures in heat exchangers,

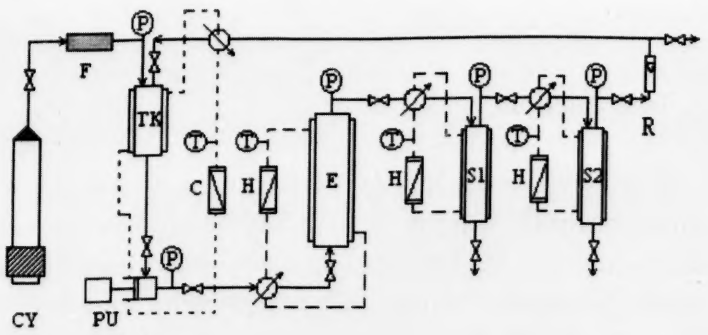

Fig. 1. Schematic diagram of the extraction of EYO from (EYP) with SC-CO_2. C, Cooler; CY, CO_2 cylinder; E, extractor; F, filter; H, heater; PU, high pressure pump; Ⓟ, pressure gauge; R, rotameter; S1, separator 1; S2, separator 2; Ⓣ, thermocouple; TK, CO_2 tank. – – – heated water circle; ----- cooled water circle; —— CO_2 circle.

extractor, separators and tank were controlled by water bathes that maintained the operating temperature within ± 0.5°C. Extractor temperature was monitored continuously with a thermocouple in extractor exit. The pressures, monitored at pump exit and at extractor exit, did not give a meaningful difference. Consequently the pressure monitored at extractor exit was considered as the operating pressure.

2.3. Experimental procedure

A desired sample was fed in extractor after some glass beads were put at the bottom of the extractor for uniform distribution of CO_2 flow. Air in the extractor was removed by CO_2. Then the desired temperatures of extractor, separators, CO_2 tank and heat exchangers were maintained by water bathes, respectively. Liquid CO_2 from the CO_2 tank was pumped into the extractor through the heat exchanger. When reaching the desired value, the extractor pressure was controlled by adjusting the micrometering valve at the separator entrance and CO_2 was passed through the extractor column to start the extraction of EYO from EYP. CO_2 bearing EYO expanded through the valve and lost its solution power to EYO. Then EYO extracted by CO_2 was precipitated at the separators and discharge of the separators was performed at fixed time intervals. CO_2 free EYO flowed into the heat exchanger through a rotameter, which measured the CO_2 flow rate, and became liquid CO_2 and returned into the liquid CO_2 tank.

2.4. Analysis

Content of EYO in EYP was analyzed using the method in reference [5]. The determination of cholesterol content in EYO follows a method as described in the literature [16]. The content of moisture was measured by a vacuum oven drying procedure (16.002, AOAC, 1984). The composition of fatty acids in EYO was analyzed using a gas chromatograph (GC-14B Shimadzu, Japan) equipped with a flame ionization detector. The column is 1 m long, 3 mm internal diameter, carried polyethylene glycol succinate supported on white diatomaceous earth. Saponification and methylation of samples were based on method 969.33, AOAC (1990). The methylated samples were analyzed under the column temperature of 180°C, the injection temperature of 250°C and the detector temperature of 250°C. The fatty acid peaks were identified by comparison with the retention times of standard fatty acids assayed under identical conditions.

3. Mathematical model

3.1. Extraction mechanism

Since the employed CO_2 flow rate is very low ($< 5 \times 10^{-3}$ ms^{-1}), the EYP particles in extractor can be considered to be stationary, and the extraction process is similar to a fixed-bed process. When CO_2 flows in the void of EYP particles in the extractor, EYO molecule is dissolved in SC-CO_2. The extraction of EYO from EYP is an unsteady process. The extraction mechanism for a single particle is described by the following steps in series: (1) EYO molecules are desorbed from matrix, and dissolved in SC-CO_2, which is called dissolution equilibrium process; (2) EYO molecules dissolved in SC-CO_2 diffuse through the solid holes to external surface, which is called internal diffusion; (3) EYO molecules diffuse from external surface through the SC-CO_2 film to fluid body, which is called external diffusion.

3.2. General hypotheses

To simplify mathematical model, following hypotheses are needed: (a) temperatures and pressures at all parts of the extractor are uniform; (b) axial dispersion of EYO is negligible; (c) EYO is uniformly distributed in EYP particle; (d) the volume fraction of extraction bed, $\bullet$, is not influenced by the weight loss of EYP during the extraction; (e) although several components are involved in the extract, their mass transfer behaviors are supposed to be similar and to be described as a single pseudocomponent, which is partly based on the experimental results that the different components in the extract are not separated during the extraction (see Table 1).

Table 1
Composition of egg yolk oil (EYO) extracted during different extraction periods[a]

Sample[b]	Composition of fatty acid in EYO/wt.%								Cholesterol/wt.%	Moisture/wt.%
	C14:0	C14:1	C16:0	C16:1	C18:0	C18:1	C18:2	C18:3		
S-1	0.50	0.20	25.26	5.02	6.81	45.45	15.84	0.92	6.99	2.3
S-2	0.27	0.09	24.08	3.43	9.40	48.02	13.87	0.84	5.03	1.9
S-3	0.41	0.14	24.63	4.54	7.26	47.57	14.43	0.92	6.59	2.2

[a] Extraction conditions: 28 MPa, 55°C, 7.0 kgCO_2 h^{-1}, 0.250 kg of EYP with a particle size of 1.2 mm.
[b] S-1, sample collected at first 30 min; S-2, at last 30 min; S-3, average sample.

3.3. Mass balance equations

According to the above hypotheses, the differential balance of EYO in the fluid phase along the extraction bed is

$$\rho \cdot \varepsilon \cdot \frac{\partial y}{\partial t} + \rho \cdot U \cdot \frac{\partial y}{\partial h} = J(x, y) \quad (1)$$

and that in the solid phase is

$$-\rho_s \cdot (1-\varepsilon) \cdot \frac{\partial x}{\partial t} = J(x, y) \quad (2)$$

where ? is the fluid density, which is supposed not to be influenced by the presence of EYO; ●$_s$ is the density of the matrix (free EYO); y is the concentration of EYO in SC-CO_2; t is the consumed time; U is superficial velocity of CO_2 through the extractor; h is bed length; x is the concentration of EYO in EYP; J is overall volumetric mass transfer rate.

The initial condition on x and y and the boundary conditions on y for finding the solution of Eqs. (1) and (2) are following:

$$\begin{cases} x(h, t=0) = x_0 \\ y(h, t=0) = 0 \\ y(t, h=0) = 0 \end{cases}$$

3.4. Overall volumetric mass transfer rate, J

The expression of J is experimentally determined, but it is strongly dependent on the structure of matrix and the behavior of EYO transfer in the solid and fluid. Therefor, it is first to understand the dependence.

The effect of the external mass transfer on the extraction was studied via some experiments of fixing contact time (fixing the ratio of EYP amount to flow rate of CO_2). The results is shown in Fig. 2, which shows that the rate of EYO extraction increases with increasing flow rate of CO_2, and then suggests that the external mass transfer of EYO should be considered when J expression is built.

Fig. 3 shows the effect of particle size on the extraction rate of EYO. There is no obvious change in the extraction rate of EYO at different particle sizes, which suggests that the internal

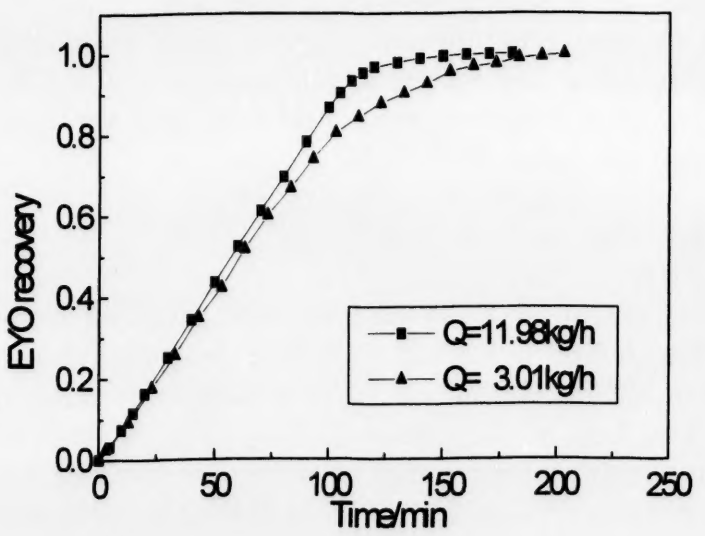

Fig. 2. Effect of flow rate of CO_2 on extraction under the fixing contact time. Conditions: temperature, 45.0●; pressure, 32.0 Mpa; particle size, 1.2 mm in diameter; CO_2 flow rate, 3.01 kg h^{-1} and 11.98 kg h^{-1} for 0.125 kg and 0.500 kg EYP, respectively.

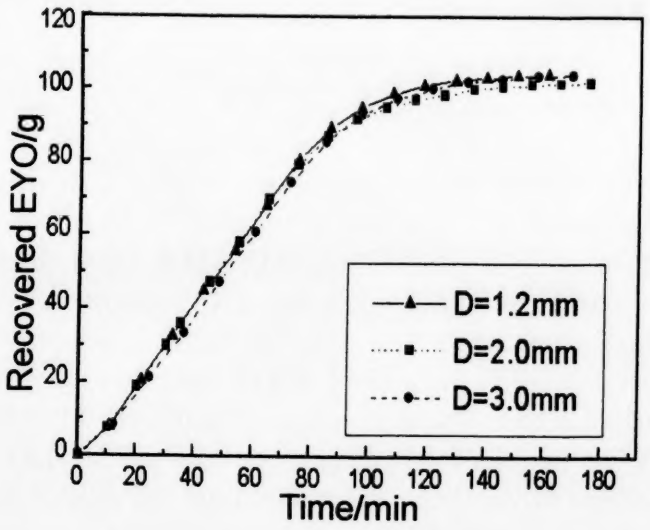

Fig. 3. Effects of particle size of EYP on extraction. Conditions: temperature, 45.0●; pressure, 32.0 Mpa; CO_2 flow rate, about 7.0 kg h^{-1}; EYP, 0.250 kg.

mass transfer of EYO have little influence on the extraction process.

In order to characterize the equilibrium of EYO dissolution between the two phases, the experiments at different CO_2 flow rates were performed and the results are shown in Fig. 4. The four sets of data exhibit no clear difference, which suggests that the amount of extracted EYO is constant when the amount of fed CO_2 is given and extraction rate is dependent on the CO_2 flow rate. It means that there is a relationship of concentrations between the two phases [11].

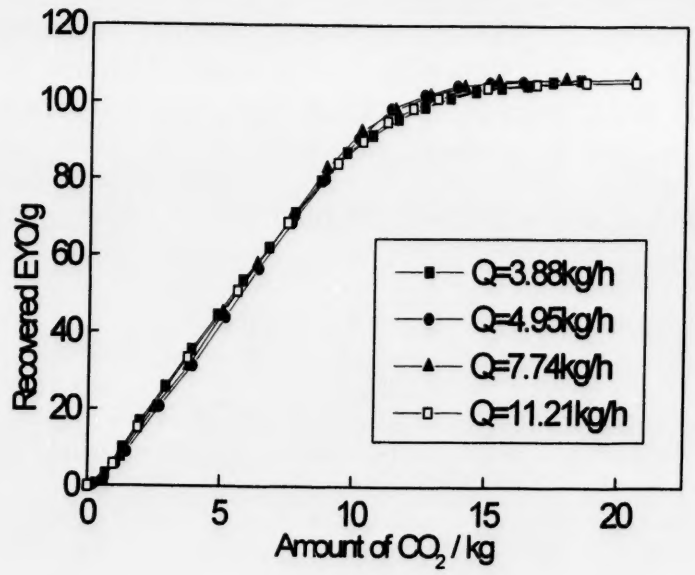

Fig. 4. Effect of CO_2 flow rate on extraction. Conditions: temperature, 45.0●; pressure, 32.0 Mpa; particle size, 1.2 mm in diameter; EYP, 0.250 kg.

To determine the relationship, it is supposed that there are two forms of EYO molecular in EYP: one is strongly adsorbed on the matrix molecular, the other is weakly adsorbed on EYO molecular, and the extraction of the latter is prior to the former. The concentration of strongly adsorbed EYO is expressed as x_k, then the concentration of the weakly adsorbed EYO is (x_0-x_k), where x_0 is the initial concentration of EYO in EYP. When the concentration of EYO in EYP, x, is greater than x_k, the fluid concentrations at the contact face of solid, y^*, reach the solubility of EYO, y_r. That is

$$y^* = y_r. \tag{4}$$

when x is less than or equal to x_k, to evaluated the equilibrium relationship between y^* and x, a linear dependence on solid concentration, x, is adopted,

$$y^* = \frac{x}{k_p} \tag{5}$$

where k_p is the adsorption constant of EYO between the solid and the fluid phases at equilibrium.

Based on the description above, J can be expressed as follows

$$J = K_f a_p \rho (y^* - y) = \begin{cases} K_f a_p \rho (y_r - y) & \text{at } z > x_k \\ K_f a_p \rho (x/k_p - y) & \text{at } x \le x_k \end{cases}, \tag{6}$$

where a_p is the specific surface area of EYP particle, K_f is the external mass transfer coefficient. Substitution of (6) into (1) and (2) leads to a partial differential equation system:

$$\begin{cases} \rho \cdot \varepsilon \cdot \dfrac{\partial y}{\partial t} + \rho \cdot U \cdot \dfrac{\partial y}{\partial h} = K_f a_p \rho (y^* - y) \\ -\rho_s (1-\varepsilon) \dfrac{\partial x}{\partial t} = K_f a_p \rho (y^* - y) \end{cases}$$

$$y^* = \begin{cases} y_r & \text{at } x > x_k \\ x/k_p & \text{at } x \le x_k \end{cases}, \tag{7}$$

After treated dimensionlessly, the equation system can be numerically solved with finite element

Table 2
Solubilities of egg yolk oil (EYO) in SC–CO_2 (g of EYO/kg of CO_2)

Pressure (MPa)	Temperature (°C)				
	35.0	45.0	55.0	65.0	75.0
25.0	5.9	5.7	5.6	4.7	3.8
28.0	6.9	6.9	7.4	6.8	6.6
32.0	8.6	9.6	10.0	9.5	9.4
36.0	9.9	11.4	13.1	13.2	13.4

method using the boundary and initial conditions (3).

As a result, two function, $y = y(t, h)$ and $x = x(t, h)$, can be obtained by solving Eq. (7) numerically. Therefore it is possible to calculate the EYO recovery, $E(t)$:

$$E(t) = \frac{Q}{WX_0} \int_0^t y(t, H)\, dt, \tag{8}$$

where Q is the CO_2 flow rate and W is the amount of EYP fed in extractor (kg). X_0 is the concentration of EYO in raw material. Thus $E(t)$ is the ratio of the amount of EYO extracted to the amount of EYO in raw material.

3.5. Determination of parameters for mathematical model

Experimental extraction curves for measuring solubility of EYO in SC-CO_2 can be divided into two parts, named fast extraction and slow extraction periods. The former process is controlled by the solubility of EYO in SC-CO_2. The latter process maybe controlled by mass transfer or desorption velocity. Solubility, y_r, was evaluated from the slope of the extraction curve in the initial period [17–19]. The solubility of EYO in SC-CO_2 was measured with the same apparatus. The results show in Table 2, which was carried out at a flow rate of about 4.0 kg h^{-1} and at various pressures and temperatures.

Three unknown parameters x_k, k_p, $K_f a_p$ in the model equations were simulated by minimizing errors between experimental data and model results.

4. Modeling results and discussion

4.1. Estimation of x_k

All values of x_k, partition factor of strongly adsorbed EYO, are nearly equal to 0.56 by simulation at 35.0–75.0°C and 25.0–36.0 MPa. It can be reasoned that x_k is an EYP characteristic, which represents the concentration relation between weakly adsorbed EYO and strongly adsorbed EYO. The percentage of strongly adsorbed EYO in EYP is $x_k/x_0 \times 100\% = 0.56/0.85 \times 100\% = 66\%$, then the percentage of weakly adsorbed EYO in EYP is $100 - 66\% = 34\%$.

4.2. Estimation of $K_f a_p$

In Eqs. (6) and (7), K_f is external mass transfer coefficient and a_p is specific surface area of EYP particles. Because a_p is difficult to be measured accurately, a_p and K_f put together were $K_f a_p$, which is called overall volumetric mass transfer coefficient. This value is of important for the scale-up of this extraction process. The factors that influence the value of $K_f a_p$ are the velocity of CO_2 through the extractor and the size and the shape of EYP particle. $K_f a_p$ at different CO_2 flow rate is shown in Table 3, where experimental conditions are 45.0°C temperature, 32.0 MPa pressure, 1.2 mm particle size, 250 g of EYP fed. In Fig. 5, $\ln(K_f a_p)$ is found to have a linear relation with CO_2 flow rate through extractor, Q. By linear regression method, the relation between $K_f a_p$ and Q is represented by

$$\ln K_f a_p = -4.172 + 0.548 \ln Q \tag{9}$$

Table 3
Simulation results of $K_f a_p$ at different flow rates of CO_2

Q (kg h^{-1})	$K_f a_p$ (s^{-1})	RAAD[a]
4.95	0.03776	0.011
7.19	0.04562	0.012
7.19	0.04370	0.010
11.76	0.06030	0.015
11.91	0.05993	0.015

[a] RAAD, Relative absolute averages deviation between experimental data and calculated values.

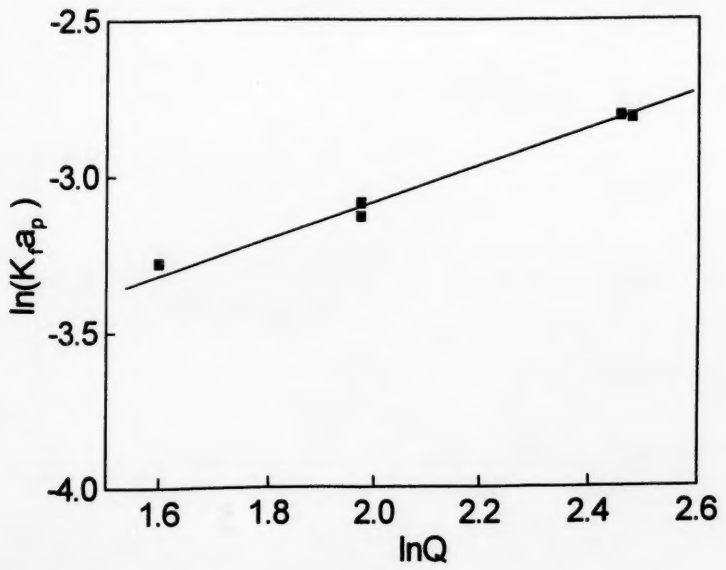

Fig. 5. Volumetic mass transfer coefficient ($K_f a_p$) vs. flow rate of CO_2.

or

$$K_f a_p = 0.01542 Q^{0.548} \quad (10)$$

If the flow rate of CO_2, Q, is substituted by the interstitial velocity of CO_2 through extractor, u, $u = Q/S \bullet \varepsilon$, where S is the area of extractor section, Eq. (10) is replaced by

$$K_f a_p = 1.17 u^{0.548} \quad (11)$$

The exponent in (10) or (11) lies between the value of 0.33 reported for mass transfer liquid [20,21] and 0.6 reported for mass transfer in gases [22] at comparable Reynolds numbers. Since supercritical fluids have physical and transport properties, such as diffusion and viscosity, which fall between those of liquid and gases. The exponent of 0.548 in Eqs. (10) and (11) is plausible.

4.3. Estimation of adsorption equilibrium constants, k_p

k_p is affected by temperature and pressure of SC-CO_2. Table 4 shows adsorption equilibrium constant, k_p, simulated by the model. k_p increases with increase of temperature and decreases with increase of pressure. At a constant temperature, the density of SC-CO_2 increases with increase of pressure, resulting in solution power increases [23,24]. Hence k_p decreases with pressure. But it seemly violates the principle of decrease of k_p with increase of temperature. Following two aspects control the solution power of EYO in SC-CO_2: density of SC-CO_2 and volatility of EYO, which increase resulting in increase of solubility. But at a constant pressure, increase of temperature causes two controversial effects, i.e. decrease of density of SC-CO_2 and increase of volatility of EYO. As a result, solution power of EYO is determined by the larger contribution one. In the range of temperatures used in this work, decrease of SC-CO_2 density as increase of temperature is the larger contribution one, causing decrease of solution power of EYO in SC-CO_2. Therefore increase of temperature causes increase of k_p.

Table 4
Simulated adsorption equilibrium constants k_p at different temperatures and pressures[a]

Temperature (°C)	Pressure (MPa)			
	25.0	28.0	32.0	36.0
35.0	76.22	64.52	54.64	48.15
45.0	76.28	73.69	55.65	53.11
55.0	90.09	72.36	57.84	55.93
65.0	90.91	90.01	81.97	57.14
75.0	100.00	92.00	73.69	65.62

[a] The other extraction conditions are particle size of 1.2 mm in diameter, CO_2 flow rate of about 7 kg h^{-1}.

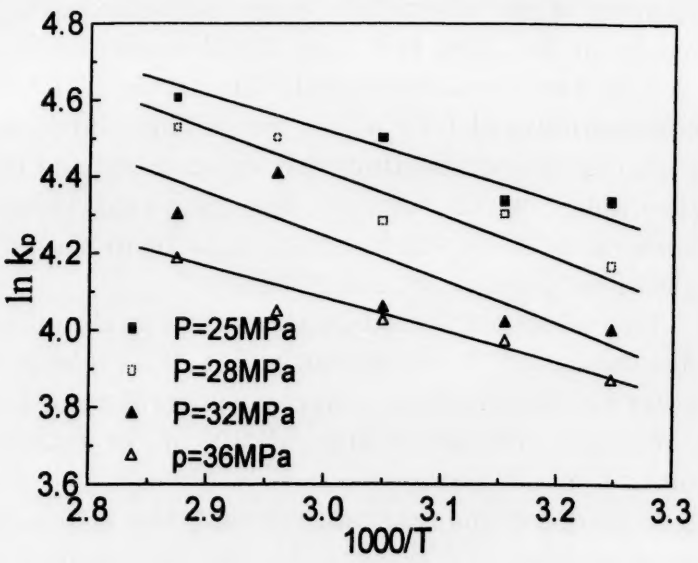

Fig. 6. Relation of adsorption equilibrium constants with temperature.

The adsorption equilibrium constants are also shown on a van't Hoff plot in Fig. 6. The slopes obtained by linear regression method at pressures of 25.0, 28.0, 32.0, 36.0 MPa are −758, −917, −1054, −753, respectively. The van't Hoff equation is

$$\ln k_p = \ln A - \frac{\Delta H}{RT} \tag{12}$$

where A is pre-exponential factor, ●H is heat of adsorption, R is the perfect gas constant, T is the temperature. The heats of EYO adsorption on the matrix at different pressures are 6.3 kJ mol^{-1} (25.0 MPa), 8.2 kJ mol^{-1} (28.0 MPa), 8.8 kJ mol^{-1} (32.0 MPa), 6.3 kJ mol^{-1} (36.0 MPa). Consequently the heat of EYO adsorption is 6–9 kJ mol^{-1}, which belongs to physical adsorption. Using a similar method, Goto et al. [15] obtained adsorption heat of peppermint oil.

4.4. Verification of the model

All parameters of the mathematical model have already been determined. Therefore the model can be used to predict the concentration of EYO in fluid or solid as a function of time or height of extraction bed and compare it with experiment for verification of the model. Extraction process was terminated after a given time. In other wards, the CO_2 flow was then stopped and extractor pressure reduced to atmospheric pressure. Aliquot EYP samples were abstracted from extractor along height of the fixed bed, then EYO concentration of each sample was analyzed. The profile of EYO concentration of EYP along the bed are shown in Figs. 7 and 8, comparing with values predicted by the model, which suggests that predicted values coincide with the experimental data from the angle of solid concentration profiles.

The values calculated by the model at different flow rates of CO_2 are shown in Fig. 9, in which it gives good agreement with experimental results.

Further evidence of the validity of the mathematical model is provided by Fig. 10, in which the feed loaded is changed and recovered oil is shown as a function of time. Fig. 10 also represents the predicted values by mathematical model in which the parameters $K_f a_p$ (determined by Eq. (10)), x_k and k_p are 0.04545 s^{-1}, 0.56 and 55.65, respectively. There is a good agreement between the experimental data and calculated values.

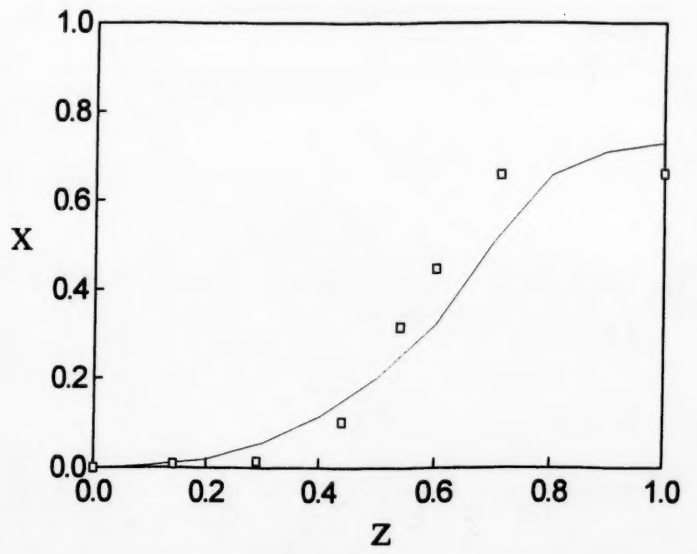

Fig. 7. EYO concentration of EYP as a function of reduced bed length after 38 min. Dots: experimental data; line: predicted value. Conditions: temperature, 45.0●; pressure, 32.0 MPa; CO_2 flow rate, 12.4 kg h^{-1}; particle size, 1.2 mm in diameter; EYP, 0.300 kg.

4.5. Application of the model on a pilot plant

This mathematical model was applied on a pilot plant of extraction of EYO with SC-CO_2.The

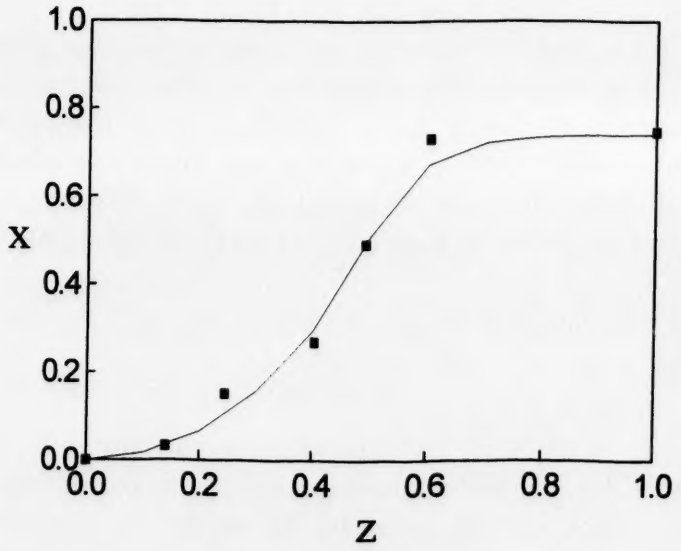

Fig. 8. EYO concentration of EYP as a function of reduced bed length after 46 min. Dots: experimental data; line: predicted value. Conditions: temperature, 45.0●; pressure, 32.0 MPa; CO_2 flow rate, 7.2 kg h^{-1}; particle size, 1.2 mm in diameter; EYP, 0.300 kg.

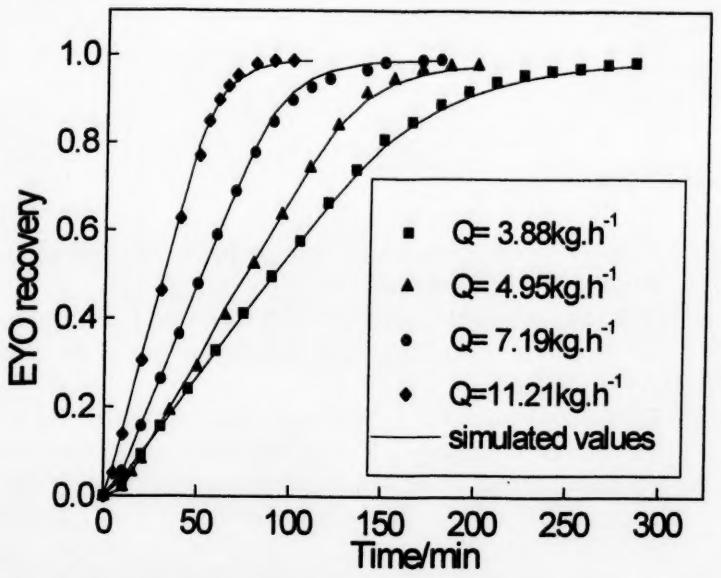

Fig. 9. EYO recovery versus time obtained by experiment and simulation at different flow rates of CO_2. Conditions: temperature, 45.0●; pressure, 32.0 MPa; particle size, 1.2 mm in diameter; EYP, 0.250 kg.

pilot plant extractor is 5×10^{-3} m^3 in internal volume. The pilot plant ran at a temperature of 45.0°C, a pressure of 32.0 MPa and a CO_2 flow rate of 22.3 kg h^{-1}, using a particle size of 1.2 mm in diameter. The pilot plant was fed 1.650 kg of EYP. The values of the mathematical

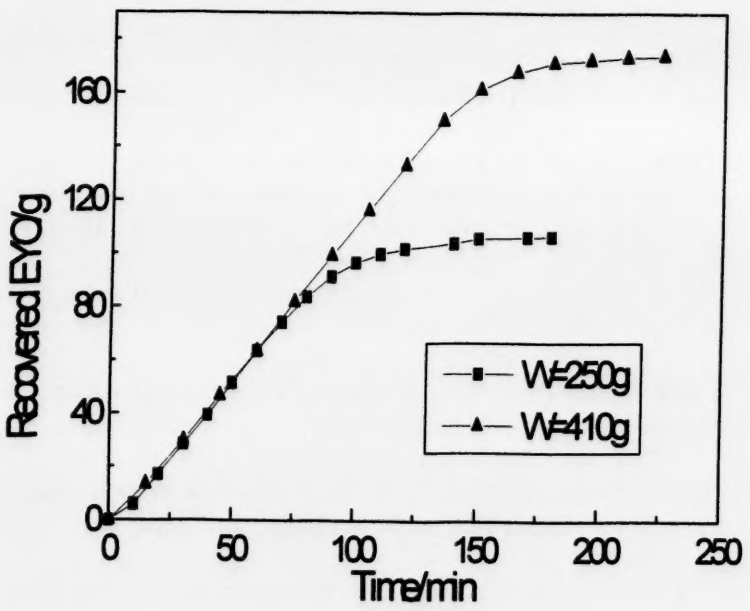

Fig. 10. Extraction rate with different amounts of feed. Conditions: temperature, 45.0●; pressure, 32.0 MPa; particle size, 1.2 mm in diameter; CO_2 flow rate, 7.19 kg h^{-1};

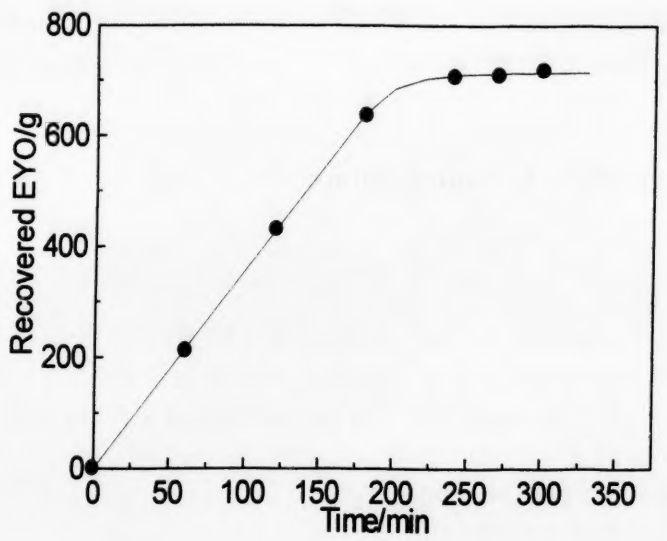

Fig. 11. EYO extracted in the pilot plant as a function of time and compared with value predicted by the mathematical model. Dots: pilot plant data; line: predicted value.

model parameters $K_f a_p$ (calculated by Eq. (11)), x_k, and k_p are 0.08453 s^{-1}, 0.56, 55.56, respectively. Both pilot plant experimental data and values predicted by the model are all shown in Fig. 11, in which recovered oil is plotted as a function of time. The model can fairly simulate and predict the extraction process in pilot plant.

5. Conclusion

According to experiments the controlling steps of SC-CO_2 extraction of EYO from EYP are the external mass transfer and the equilibrium between two phases. Based on above mechanism, a mathematical model was proposed. The parameters of the model, obtained by simulation, indicated that: (a) there are 34 wt.% of EYO adsorbed weakly on the matrix and 66 wt.% strongly; (b) overall volumetric mass transfer coefficient is directly proportional to CO_2 flow rate through extractor with an exponent of 0.548. The correlation of the coefficient as the function of flow rate of CO_2 was obtained; (c) the model simulated adsorption equilibrium coefficients of EYO in the matrix. The heat of adsorption, ●H, is 6–9 kJ mol^{-1}.

The mathematical model was verified and applied on pilot plant. The results indicated that the mathematical model could simulate the ex-

traction process of EYO with SC-CO_2 in a satisfactory degree.

Appendix A. Nomenclature

a_p specific surface area of EYP, m^{-1}
D particle size of EYP in diameter, m
E EYO recovery, (kg of extracted EYO) (kg of EYO in feed)$^{-1}$
H overall bed length, m
h bed length, m
J overall volumetric mass transfer rate, kg m^{-3} s^{-1}
K_f external mass transfer coefficient, m s^{-1}
k_p the adsorption constant of EYO between the solid and the fluid phases at equilibrium, $k_p = x/y^*$
Q mass flow rate of CO_2, kg s^{-1}
S area of extractor section, m^2
t time consumed in extraction, s
U superficial velocity of CO_2 through extractor, ms^{-1}, $U = Q/\rho S$
u fluid interstitial velocity, m s^{-1}, $u = U/\varepsilon$
W amount of EYP loaded in extractor, kg
X_0 initial EYO concentration of feed, (kg of EYO) (kg of EYP)$^{-1}$
x EYO concentration in EYP, (kg of EYO) (kg of matrix)$^{-1}$
x_k strongly adsorbed EYP concentration in EYP, (kg of EYO) (kg of matrix)$^{-1}$
x_0 initial EYO concentration in EYP, (kg of EYO) (kg of matrix)$^{-1}$, $x_0 = 0.851$
y EYO concentration in SC-CO_2, (kg of EYO) (kg of CO_2)$^{-1}$
y_0 initial EYO concentration in SC-CO_2, (kg of EYO) (kg of CO_2)$^{-1}$
y^* EYO concentration in the solvent in equilibrium with EYP (kg of EYO) (kg of CO_2)$^{-1}$
y_r the solubility of EYO in SC-CO_2, (kg of EYO) (kg of CO_2)$^{-1}$
z reduced bed length, $z = h/H$
ρ SC-CO_2 density, kg m^{-3}
ρ_s particle density of the matrix part of EYP, kg m^{-3}
ε fluid volume fraction

References

[1] K.R. Seather, Successes and failures in Australia, Paultry Int. 31 (1992) 60.
[2] Y.E. Larsen, G.W. Froning, Extraction and processing of various components from egg yolk, Poutry Sci. 60 (1981) 160.
[3] G.W. Froning, R.L. Wehling, S.L. Cuppett, M.M. Pierce, L. Niemann, D.K. Siekman, Extraction of cholesterol and other lipids from dried egg yolk using supercritical carbon dioxide, J. Food Sci. 55 (1) (1990) 95.
[4] T.V. Hung, M.A. Unger, Cholesterol reduced egg yolk by supercritical fluid extraction, Food Australia 47 (5) (1995) 227.
[5] W.Z. Wu, X.X. Cui, L.Z. Wu, Supercritical carbon dioxide extraction of yolk oil, China Surfactant Detergent Cosmetics 2 (1999) 13.
[6] L.Z. Wu, A method of preparation of high purity phospholipid from egg yolk powder, Chinese Patent ZL 94102372.9, 1994.
[7] A.K.K. Lee, N.R. Bulley, M. Fattori, A. Meisen, Modeling of supercritical carbon dioxide extraction of Canola seed oil in fixed beds, JAOCS 63 (1986) 921.
[8] N.R. Bulley, M. Fattori, Supercritical fluid extraction of vegetable oil seeds, JAOCS 61 (1984) 1362.
[9] M. Fattori, N.R. Bulley, A. Meisen, Carbon dioxide extraction of canola seed oil solubility and effect of seed treatment, JAOCS 65 (1988) 968.
[10] E. Reverchon, G. Donsi, S. Osseo, Modeling of supercritical fluid extraction from herbaceous matrices, Ind. Eng. Chem. Res. 32 (1993) 2721.
[11] E. Reverchon, Mathematical modeling of supercritical extraction of sage oil, AIChE J. 42 (1996) 1765.
[12] B.C. Roy, M. Goto, T. Hirose, O. Navaro, O. Hortacsu, Extraction rates of oil from tomato seeds with supercritical carbon dioxide, J. Chem. Eng. Jpn. 27 (1994) 768.
[13] E. Reverchon, M. Poletto, Mathematical modeling of supercritical CO_2 fractionation of flower concretes, Chem. Eng. Sci. 51 (1996) 3741.
[14] B.C. Roy, M. Goto, T. Hirose, Extraction of ginger oil with supercritical carbon dioxide: experiments and modeling, Ind. Eng. Chem. Res. 35 (1996) 607.
[15] M. Goto, M. Saot, T. Hirose, Extraction of peppermint oil by supercritical carbon dioxide, J. Chem. Eng. Jpn. 26 (1993) 401.
[16] P.L. Yeh, J.H. Liang, L.S. Hwang, Separation of fatty acids esters from cholesterol in esterified natural and synthetic mixtures by supercritical carbon dioxide, JAOCS 68 (14) (1991) 224.
[17] B.C. Roy, M. Goto, T. Hirose, O. Navaro, O. Hor-

tacsu, Extraction rates of oil from tomato seeds with supercritical carbon dioxide, J. Chem. Eng. Jpn. 27 (1994) 768.

[18] M. Fattori, N.R. Bulley, A. Meisen, Carbon dioxide extraction of canola seed oil and effect of seed treatment, JAOCS 65 (1988) 968.

[19] F. Favati, J.W. King, M. Mazzanti, Supercritical carbon dioxide extraction of evening primrose oil, JAOCS 68 (1991) 422.

[20] P.W. Appel, J. Newman, Application of the limiting current method to mass transfer in packed beds at very low Reynolds number, AIChE J. 22 (1976) 979.

[21] E.J. Wilson, C.J. Geankoplis, Liquid mass transfer at very low Reynolds numbers in packed beds, Ind. Eng. Chem. Fund. 5 (1966) 9.

[22] N. Wakao, T. Funazkari, Effect of fluid dispersion coefficients on particle-to-fluid mass transfer coefficients in packed beds, Chem. Eng. Sci. 33 (1978) 1375.

[23] J.P. Friedrich, E.H. Pryde, Supercritical CO_2 extraction of lipid-bearing materials and characterization of the products, JAOCS 61 (2) (1984) 223.

[24] M.A. Ribeiro, M.G. Bernardo-Gil, Solubilities of triolein in supercritical carbon dioxide, J. Chem. Eng. Data 40 (6) (1995) 119.

ELSEVIER

Journal of Supercritical Fluids 19 (2001) 161–175

THE JOURNAL OF Supercritical Fluids

www.elsevier.com/locate/supflu

Modeling and simulation of the supercritical CO_2 extraction of vegetable oils

E. Reverchon *, C. Marrone

Dipartimento di Ingegneria Chimica a Alimentare, Università di Salerno, Via Ponte Don Melillo, 84084 Fisciano (SA), Italy

Received 11 March 2000; received in revised form 7 August 2000; accepted 11 September 2000

Abstract

The model of broken and intact cells has been applied to the experimental results on oil seed supercritical extraction obtained by various authors and on several species of seeds. The results analyzed are related to various extraction apparatus ranging from very low laboratory scale to pilot plants. Moreover, a wide range of operating conditions has been covered, CO_2 flow rates ranging between 1.5 and 750 g/min, extraction pressures from 240 to 550 bar, temperatures between 25 and 50°C and particle diameters from 0.25 to 4 mm have been considered. Besides, the experimental results existing in the literature, systematic scanning electron microscope (SEM) analysis have been performed on seed particles belonging to the different seed species studied, thus obtaining data about the microscopic cells that bear the oil that are characteristic of the different seed structures. Operating in this manner the differential mass balances that characterize this kind of models have been supported by microscopic information on seed structure and the number of adjustable parameters in the model has been reduced to only one, the internal mass transfer coefficient (k_i). A fair good fitting of all the available experimental results has been obtained using best fit k_i values ranging between 2.4×10^{-7} and 9.2×10^{-8} m/s and producing a coherent description of the extraction process. Some simulation tests have also been performed that evidenced the role of particle size and of internal mass transfer and of their interaction on the overall performance of the extraction process. © 2001 Elsevier Science B.V. All rights reserved.

Keywords: Supercritical extraction; Seed oil; Modeling; Simulation

1. Introduction

Vegetable oils are one of the most interesting products proposed for supercritical fluid extraction (SFE). Indeed, in these cases supercritical fluid processing is very promising for improving the traditional industrial techniques that are based on hexane extraction for vegetable oils.

SFE of seed oil has been studied by several authors from the processing point of view and a wide range of seed species has been explored, wheat germ [1]; oats [2]; corn germ [3]; cottonseed [4,5]; soybean [5,6]; rice bran [7]; evening primrose [8]; jojoba [9]; rapeseed [6]; peanut [10] and grape seed [11].

* Corresponding author. Tel.: +39-089-964116; fax: +39-089-964057.

E-mail address: reverch@dica.unisa.it (E. Reverchon).

0896-8446/01/$ - see front matter © 2001 Elsevier Science B.V. All rights reserved.
PII: S0896-8446(00)00093-0

However, despite the relatively large number of species processed, only some models of the SFE of seed oil have been published.

The mathematical models proposed are generally based on differential mass balance integration. Bulley et al. [12] Lee et al. [13] and Fattori et al. [14] assumed that mass transfer resistance was only in the solvent phase. In other models, the authors considered an internal mass transfer resistance. King and Catchpole [15] used a shrinking core model to describe a variable external mass transfer resistance where the solute balance on the solid phase determines the thickness of the mass transfer layer in the external part of the particles.

A first attempt at the introduction of a physical description of vegetable substrate was proposed by Sovovà. Indeed, Sovová [16] and Sovová et al. [17,18] considered the solid phase as divided between broken and intact cells containing the vegetable oil. The merit of this model is to use a realistic description of the vegetable structure. Its major drawback is the large number of adjustable parameters it contains (four in the case of sea buckthorn and three in the case of grape seed). At least three independent data sets are required to proper modeling (for example, three different CO_2 flow rates with all the other process parameters set at a fixed value) to obtain from least squares analysis the set of parameter values that validates the model. Moreover, the authors only tested simplified forms of this model. The hypothesis of Sovovà about vegetable microstructure was verified by scanning electron microscope (SEM) for almond and fennel particles by our research group [19,20]. The internal mass transfer coefficient was the only one adjustable parameter remaining in the model since all the other parameters were calculated from data and from vegetable microstructure.

However, only limited set of data have been used until now, that are applicable only to the specific material studied and no attempts were made to extensively test a mathematical model on several seed species.

Therefore, the scope of this work is to try to extend the broken–intact cells model plus microstructure analysis to all the seed oils obtained by SFE using the data sets available in the literature and the SEM image analysis of seed microstructures.

2. General description of the SFE experiments

The extraction apparatus used for the SFE of seed oils usually consists of an extractor (internal volume V, internal diameter D_i) filled with seed particles and one or more separators operated in series. The separators are equipped with a device that allows the discharge of the extracts at fixed time intervals. CO_2 is delivered by a high pressure pump. The instantaneous CO_2 flow rate and the total quantity of CO_2 used are usually measured by calibrated rotameters and test meters, respectively.

When an extraction experiment starts, the extractor is pressurized with CO_2 first, then, when the operating pressure has been reached, CO_2 is allowed to flow continuously through the extractor at the set flow rate.

Before extraction, seeds are milled down to different mean particle sizes d_p. This operation is essential for the efficiency of the extraction process — we will see that particle size is one of the controlling parameters on the extraction rate and on the asymptotic yield of oil. The seed quantity loaded in the extractor is indicated by m_0 and the weight flow rate of supercritical CO_2 is indicated by W. The asymptotic yield of oil is the total quantity of oil extractable from the seed.

The main components of vegetable oils are triglycerides whose solubility in supercritical CO_2 becomes appreciable at 40°C for pressures around 200 bar [21].

A useful feature that can be added to the extraction process is the fractional separation of the extracts to isolate seed oil from waxes [22,23].

3. Mathematical model

The modeling of the extraction process is based on the following hypotheses.

1. We suppose that the behavior of all compounds extracted is similar and can be described by a single pseudo-component with respect to the mass transfer phenomena.

2. Concentration gradients in the fluid phase develop at larger scales than the particle size.
3. The solvent flow rate, with superficial velocity u, is uniformly distributed in all the sections of the extractor.
4. The volume fraction of the fluid, ε, is not affected by the reduction of the solid mass during extraction.

   Further hypotheses regard the natural matrix.
5. The solute in the solid is present in two separate phases. One phase includes the solute contained inside the internal structure of the particles (the 'tied solute' phase). It fills a fraction ϕ_t of the overall volume occupied by the seed particles. This value does not change during the extraction process and, therefore, ϕ_t is considered constant. The average tied solute concentration is called P. The other phase is made of the solute freely available on the particle surface. The concentration here is always the same and, according to our hypotheses, it is equal to the pure solute density ρ_o.
6. The fraction of the seed volume filled by the free solute before extraction is $\phi_f = 1 - \phi_t$.
7. The fraction of the seed occupied by the free solute during the extraction is $\psi\phi_f$ where is $\psi \leq 1$.
8. A linear equilibrium relationship applies between phases.

More details on model hypothesis have been previously published [19,20].

During the extraction, both the free solute and the tied solute move from the seed particles to the solvent. This flux might reduce the volume occupied by the seed particles and probably change ϕ_f and ϕ_t values. In particular, during the extraction, the volume occupied by the free solute phase in the untreated particles is filled by the solvent. The small value of ϕ_f makes negligible the effective increase of the volume fraction occupied by fluid in the extractor (ε) due to the reduction of the volume occupied by the free solute phase during the extraction. The inclusion of ε and ϕ changes in a mathematical model would make its resolution considerably harder; we avoided it according to hypothesis d).

According to the above hypotheses, the mass balance on the solute in the extractor is:

$$\varepsilon \cdot \rho_f \cdot D_L \cdot \frac{\partial^2 C}{\partial z^2} + \varepsilon \cdot \rho_f \cdot \frac{\partial C}{\partial t} + \rho_f \cdot u \cdot \frac{\partial C}{\partial z} + (1-\varepsilon)\phi_t \cdot \rho_s \cdot \frac{\partial P}{\partial t} + (1-\varepsilon)\phi_f \cdot \rho_0 \cdot \frac{\partial \psi}{\partial t} = 0 \quad (1)$$

where D_L is the axial dispersion, u the superficial velocity, ρ_f the fluid density, which we suppose is not affected by the presence of the solute, ρ_s the bulk density of the non-soluble solid that is the mass of non-soluble solids in the seeds per unit of filled particle volume, that is the total volume of the particle minus the volume of broken cells.

The general mass balance on the phase of the free solute alone is:

$$\rho_o \frac{\partial \Psi}{\partial t} = -\frac{k_f a(\rho_o - K_\psi C)}{(1-\varepsilon)\phi_f} \quad \text{until } \Psi > 0,$$

$$\text{otherwise } \frac{\partial \Psi}{\partial t} = 0 \quad (2)$$

where a is the specific surface of the seed particles and k_f is the external mass transfer resistance.

We simulated the initial equilibrium regime that has been experimentally observed by the authors in the literature by using very large values of k_f in Eq. (2). The correctness of this procedure was verified by changing these k_f values and observing that no significant variations occurred in the modeled extraction kinetics.

The mass balance on tied solute is:

$$\frac{\partial P}{\partial t} = -\frac{k_i \cdot a(P - K_p C)}{(1-\varepsilon)\phi_t} \quad (3)$$

where k_i is the internal mass transfer resistance.

In Eqs. (2) and (3) the same mass transfer area a was included. This assumption is not strictly true since the mass flux might affect different area partitions of the particle surface. This model however is unable to make a distinction between the effect of a mass transfer area change and that of a mass flux change. For this reason, the exchange area was conventionally put equal to a.

The system of equations from Eq. (1) to Eq. (3) has a unique solution when the initial conditions (i.c.) on C, P and ψ and the boundary condition (b.c.) on C are given:

(i.c.) At $t=0$: $C=C_0$; $P=P_0$; $\Psi=\Psi_0$; for each z (4)

(b.c.) At $z=0$: $\frac{u}{\varepsilon}\cdot C - D_L\cdot\frac{\partial C}{\partial z}=0$ for each t (5)

(b.c.) At $z=L$: $\frac{\partial C}{\partial z}=0$ for each t (6)

We preliminary performed some tests to evaluate the influence of the axial dispersion on the SFE process. The value of D_L we used was obtained from the correlations proposed by Funazukuri et al. [24] and Catchpole et al. [25] using two different experimental methods. These two correlations give similar D_L values [24]. However, the presence of D_L practically did not affect the modeling results; i.e. the same results were obtained with and without inserting the axial dispersion. Therefore, we decided to perform modeling omitting the axial dispersion in Eq. (1). The corresponding boundary conditions 4 and 5 were substituted by:

(b.c.) At $z=0$: $C=0$ for each t (7)

We also supposed that the loading time of the solvent into the extractor is long enough to enable the fluid to reach the equilibrium concentration before the extraction started. Therefore, from hypothesis h) we have:

$$\rho_o = K_\psi C_0 \tag{8}$$

where K_ψ is the equilibrium constant between the solvent and the free solute phase. This means that, before the extraction starts, a part of the oil present in the seed saturates the fluid. This condition, together with Eq. (8), implies that the tied solute phase and the solvent are at equilibrium at the extraction start and, therefore, after hypothesis h):

$$P_0 = K_p C_0 \tag{9}$$

where K_p is the equilibrium constant between these two phases. As a consequence of this hypothesis, free solute alone participates to the initial saturation of the solvent. This condition is necessary for Eq. (8) to apply. Therefore, the volume fraction ψ_0 of the free solute at the extraction start is different from unit that is the value of ψ in the untreated seed.

Both Eqs. (8) and (9) are valid under the hypothesis of a linear equilibrium relationship between the solvent and any of the solute phases. This provides a simplified view of the system. However, we do not have more accurate information on thermodynamic behavior, to confidently assume more complex equilibrium models.

The value of C_0 can be calculated from the experimental plot of the oil yield as a function of the mass of solvent flowed, m_s:

$$C_0 = \frac{m_e}{m_s} = \frac{m_e}{m_0}\cdot\frac{m_0}{m_s} = Y/\frac{m_s}{m_0} \tag{10}$$

where m_e is the mass of the extracted oil and m_0 is the initial mass of seed. The last term of Eq. (10) is the slope of the linear section of the yield curve.

The values ϕ_f and ϕ_t can be determined from SEM images of the seed particles and the values Ψ_0, P_0 and ρ_s can be determined from the following mass balances. The free oil mass balance that relates C_0 and ψ_0 to the loading of the untreated solid:

$$\rho_o(1-\varepsilon)\phi_f = \rho_o(1-\varepsilon)\phi_f\psi_0 + C_0\rho_f\varepsilon \tag{11}$$

mass balance on the total free oil:

$$\rho_e Y_\infty = \rho_o\phi_f + P_0\rho_s\phi_t \tag{12}$$

mass balance on the non-soluble solids

$$\rho_s\phi_t = \rho_e(1-Y_\infty) \tag{13}$$

where Y_∞ is the value of the asymptotic extractable oil yield and ρ_e is the density of seeds.

From Eqs. (11)–(13) we can calculate Ψ_0, P_0 and ρ_s, respectively.

The set of differential Eqs. (1)–(3) was numerically integrated using a finite difference method. A Wendroff numerical cell was used. This method is characterized by an implicit computational cell that assures calculation stability whichever is the interval (of time and of space) used. We also selected the computation intervals to set the Courant number equal to 1 to minimize the computational error. The solution was performed in an explicit manner (calculus simplicity) but the method maintains the advantage of the implicit cell (calculus stability). This method has been described in detail in Lapidus and Pinder [26].

4. Results and discussion

A scanning of the scientific literature revealed that there is enough information (data, experimental apparatus and vegetable charge characteristics) to model SFE for the extraction of vegetable oil of sunflower [27], tomato [28], coriander [29] and grape seed [18]. Almond [19] and fennel oil extraction [20] that has been previously modeled using the same model have also been taken into account. Moreover, liquid SFE extraction of peanut seeds [30] was also considered. Some other papers that could have been of interest for our work were discarded since they contain not enough information about the experimental conditions or about the experimental apparatus or the experiments were performed only at different pressures, whereas, the other relevant process parameters were not varied at all.

The relevant experimental data for the various works in the literature has been summarized in Table 1. In the case of tomato oil extraction, the value of m_0 was not reported in the paper [28]. However, we assumed that the volume fraction of the fluid phase in the extractor (ε) was 0.4 that is a usual value for this parameter and, since the extractor volume was given in the paper, we calculated for m_0 (1.26 g) as reported in Table 1.

The second kind of information requested to apply the proposed mathematical model is related to seed microstructure, particularly to the geometric characteristics of the oil-bearing cells. These cells should not be confused with biological cells that are much smaller. Systematic SEM analysis of seed particles has been performed to obtain this data. The analysis of seed structures showed that the oil-bearing cells of the various seeds studied have different shape and size but shape and size are fixed for a given species of seed. This last observation means that SEM images are required only at one time for each seed species. Some examples of SEM images of seed particles are shown in Figs. 1 and 2 and are related to coriander and grape seed, respectively. In these cases, cells are spherical and do not contain any oil since images have been produced from SFE processed material. However, some starch aggregates are still present and form small spherical particles located inside the vegetable structure, since this last material is not extractable by supercritical CO_2. SEM images of non-spherical seed cells were previously published for fennel seed [20].

To evaluate the total volume of the broken cells on the particle surface, we first determined their number as the ratio between the area of the particle surface (spherical particles) and the area of the single broken cell, obtained from SEM images. From this value, and making simple geometric considerations on the shape of the cell, we obtained the volume of the cell. The total volume occupied by broken cells on particle surface is, then, approximately one half of the total volume of broken cells since only part of these cells is available on the particle surface. From these calculations we obtained ϕ_f for the various seed species and for the used particle sizes, as reported in Table 3.

In Table 2 the characteristic parameters of the oil-bearing cells for the various seeds are shown.

Using the experimental data taken from the literature and from microscopic image analysis it has been possible to calculate all the parameters to be used in the proposed mathematical model, except the internal mass transfer coefficient that has been used as the only adjustable parameter in the model. Table 3 summarizes the values of parameters used in the mathematical modeling of the various seeds.

First of all, it is possible to discuss modeling results for the single data sets and single seed.

Sunflower seed oil extraction was performed by Perrut et al. [27] using a laboratory and a pilot extraction plant. The experiments were performed operating at 280 bar and 40°C using CO_2 flow rates ranging from 83.3 to 750 g/min and a particle size of 3 mm. The authors modeled the experimental results assuming that two different extraction regimes characterize the process, which were related to two differently bonded fractions of the solute. They also used a non-linear equilibrium curve and found a best fit value for k_i of 2.2×10^{-5} m/s.

SEM analysis of sunflower seed particles showed that the oil-bearing cells were ellipsoidal. The refit of the experimental data gave us a best fit value of k_i of 4.0×10^{-7} m/s. The experimental data and the model curves are shown in Fig. 3.

Coriander seed oil supercritical extraction was performed by Catchpole et al. [29]. They did the experiments at 250 bar and 40°C using two different CO_2 flow rates (86 and 213 g/min) and particle sizes (0.56 and 0.92 mm). The authors adopted a model based on the solid phase mass balance performed on a spherical particle (shrinking core) using some simplifications that produced an equations system with an analytical solution. The best fit value of k_i they obtained was 9×10^{-9} m/s.

We used the model with the data reported in Tables 1–3 obtaining a best fit value of k_i of 5.4×10^{-8} m/s. The experimental data and the model curves were reported in Figs. 4 and 5 where

Table 1
Experimental conditions in the literature for the SFE of oil from different seeds

	P (bar)/T (°C)	D_i (cm)	H (cm)	m_0 (g)	d_p (mm)	W (g/min)
Sunflower						
Test 1	280/40	8.2	28	500	3	750
Test 2	280/40	8.2	28	500	3	416.6
Test 3	280/40	8.2	28	500	3	166.6
Test 4	280/40	8.2	28	500	3	83.3
Coriander						
Test 1	250/40	10	27	1050	0.56	86
Test 2	250/40	10	27	1050	0.92	86
Test 3	250/40	10	27	1050	0.56	213
Test 4	250/40	10	27	1050	0.92	184
Grape						
Test 1	280/40	0.8	12.2	4.5	0.36	0.9
Test 2	280/40	0.8	15.5	0.57	0.36	1.7
Test 3	280/40	0.8	14.5	5.32	0.81	1.7
Test 4	280/40	0.8	14.6	5.38	0.73	1.7
Test 5	280/40	0.8	15.2	5.58	0.45	1.7
Tomato						
Test 1	240/40	0.75	5	1.26	0.25	1.5
Test 2	240/40	0.75	5	1.26	0.25	3.18
Test 3	240/40	0.75	5	1.26	0.25	5.88
Test4	240/40	0.75	5	1.26	1.02	3.42
Test5	240/40	0.75	5	1.26	0.65	3.42
Test 6	240/40	0.75	5	1.26	0.46	3.42
Test 7	240/40	0.75	5	1.26	0.25	3.42
Peanut						
Test 1	550/25	5	38	500	1.1	72
Test 2	550/25	5	38	500	1.4	72
Test 3	550/25	5	38	500	2	72
Test 4	550/25	5	38	500	2.8	72
Test 5	550/25	5	38	500	4	72
Almond						
Test 1	300/50	4	16	160	0.30	12
Test 2	300/50	4	11.5	72	0.70	23.3
Test 3	300/50	4	11.5	84	0.30	23.3
Fennel						
Test 1	200/40	5.5	16.5	281	0.372	8.3
Test 2	200/40	5.5	16.5	304	0.372	16.6
Test 3	200/40	5.5	16.5	275	0.372	24.9

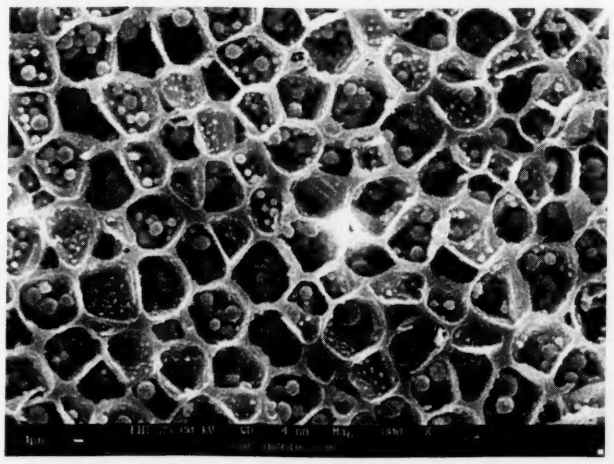

Fig. 1. SEM image of coriander seed particle. Broken cells are evidenced.

the influence of different particle sizes and of different CO_2 flow rates is reported, respectively.

Very different oil yields were obtained for the process times used for the supercritical extraction. In the extraction of the larger particles, the most inner part of the solid is not efficiently reached by the solvent and can participate only in part to the extraction process. However, when the extraction time is sufficiently long, also in the case of large particles the oil yield curves may approach a value corresponding to the complete extraction. As we will see in the following discussion, this phenomenon is not limited to coriander seed extraction experiments but is a general feature of the extraction process when large particles are used.

Grape seed oil was extracted by Sovovà et al. [18] operating at 280 bar and 40°C. They studied

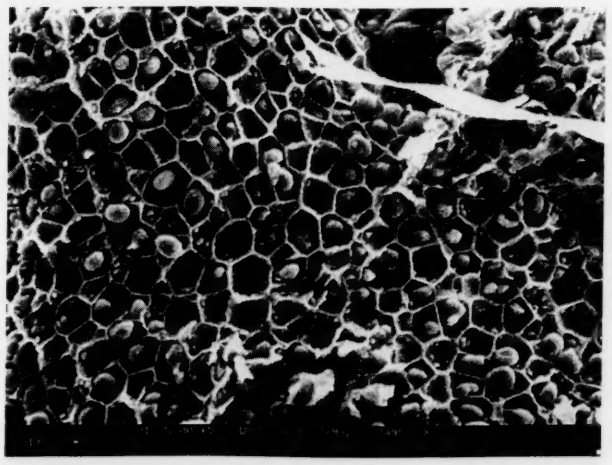

Fig. 2. SEM image of grape seed particle. Broken cells are evidenced.

Table 2
Shape and characteristic dimensions of the oil-bearing cells for the different kind of seeds studied

Seed	Cells shape	Mean cell dimensions (μm)
Sunflower	Ellipsoidal	$D_1 = 60$; $D_2 = 10$
Coriander	Spherical	$D = 15$
Grape	Spherical	$D = 20$
Tomato	Spherical	$D = 25$
Peanut	Cylindrical	$L = 20$; $D = 18$
Almond	Spherical	$D = 20$
Fennel	Hexagonal	$L = 90$; $D = 10$

the process behavior for different particle sizes (between 0.45 and 0.81 mm) and different CO_2 flow rates (between 0.9 and 1.7 g/min). They modeled the experimental results using the broken and intact cells model (that, indeed, was first proposed by Sovovà [16]); however, in their version this model had at least three adjustable parameters, since microscopic information was not available. The use of five parameters means that three or more independent data sets are required to obtain a single set of parameter values that are the best fit of the experimental data. If less than three independent data sets are used there will be an indefinite number of parameter sets that verify the best fit. However, they obtained a best fit value of k_i of 6×10^{-10} m/s.

Using the same procedure explained in the previous paragraphs, we modeled the experimental results on grape oil obtaining a best fit k_i value of 2.4×10^{-7} m/s. The model curves together with the experimental data are reported in Figs. 6 and 7 related to the experiments performed at different particle sizes and different CO_2 flow rates, respectively.

Also in this case the experiments at different particle sizes evidenced the yield reduction for larger particles in a fixed extraction time (see Fig. 6) as discussed in the case of coriander seed oil extraction.

Tomato seed oil extraction was studied by Roy et al. [28]. They studied the oil yield of the process operating at 240 bar and 40°C using various particle sizes (between 0.25 and 1.02 mm) and different CO_2 flow rates (between 1.5 and 5.88 g/min). A high pressure UV–vis spectrophotome-

ter was installed at the extractor outlet for the continuous monitoring of the extract content in the solvent. For this reason, the experimental data related to these experiments are practically continuous and are reported as dotted lines in Fig. 8. These authors also proposed the concept of two different extraction rates along the process time considering broken and unbroken structures. They used a model based on differential mass balances in which the term related to convective mass transfer (in the fluid phase mass balance) was substituted with C/t where t is the residence time. This simplification transformed the equation system from PDEs to ODEs. The best fit value of

Table 3
Parameters used in the mathematical modeling of the various seeds studied

	ϕ_f	C_0 (g/g)	ρ_s (g cm^{-3})	P_0 (g/g)	ψ_0	K_p	K_ψ	Y_∞
Sunflower								
Test 1	0.03	0.011	0.66	0.42	0.36	38.9	81.8	0.35
Test 2	0.03	0.011	0.66	0.42	0.36	38.9	81.8	0.35
Test 3	0.03	0.011	0.66	0.42	0.36	38.9	81.8	0.35
Test 4	0.03	0.011	0.66	0.42	0.36	38.9	81.8	0.35
Coriander								
Test 1	0.01	0.004	1.03	0.06	0.50	14.1	209	0.065
Test 2	0.01	0.004	1.06	0.03	0.13	7.2	209	0.065
Test 3	0.01	0.004	1.03	0.06	0.50	14.1	209	0.065
Test 4	0.01	0.004	1.06	0.03	0.13	7.2	209	0.065
Grape								
Test 1	0.034	0.007	1.00	0.09	0.09	14.1	132	0.11
Test 2	0.034	0.007	1.00	0.09	0.09	14.1	132	0.11
Test 3	0.015	0.007	1.05	0.03	0.77	5.0	132	0.05
Test 4	0.017	0.007	1.04	0.04	0.80	6.5	132	0.06
Test 5	0.028	0.007	1.01	0.08	0.88	12.0	132	0.10
Tomato								
Test 1	0.044	0.008	0.81	0.33	0.84	42.2	112.5	0.28
Test 2	0.044	0.008	0.81	0.33	0.84	42.2	112.5	0.28
Test 3	0.044	0.008	0.81	0.33	0.84	42.2	112.5	0.28
Test 4	0.010	0.008	0.99	0.09	0.30	11.2	112.5	0.09
Test 5	0.016	0.008	0.92	0.17	0.51	19.7	112.5	0.16
Test 6	0.023	0.008	0.86	0.25	0.62	34.9	112.5	0.22
Test 7	0.044	0.008	0.81	0.33	0.84	42.2	112.5	0.28
Peanut								
Test 1	0.013	0.018	0.64	0.70	0.013	39.1	52.8	0.42
Test 2	0.013	0.018	0.68	0.62	0.005	34.5	52.8	0.39
Test 3	0.013	0.018	0.78	0.41	0.005	22.9	52.8	0.30
Test 4	0.013	0.018	0.82	0.33	0.005	18.6	52.8	0.26
Test 5	0.013	0.018	0.91	0.20	0.005	11.4	52.8	0.18
Almond								
Test 1	0.033	0.011	0.54	0.98	0.88	89.2	86.3	0.51
Test 2	0.014	0.011	0.62	0.73	0.14	66.6	86.3	0.43
Test 3	0.033	0.011	0.54	0.98	0.71	89.2	86.3	0.51
Fennel								
Test 1	0.02	0.002	1.08	0.1	0.93	49.7	474	0.09
Test 2	0.02	0.002	1.08	0.1	0.95	52.4	474	0.09
Test 3	0.02	0.002	1.08	0.1	0.93	49.7	474	0.09

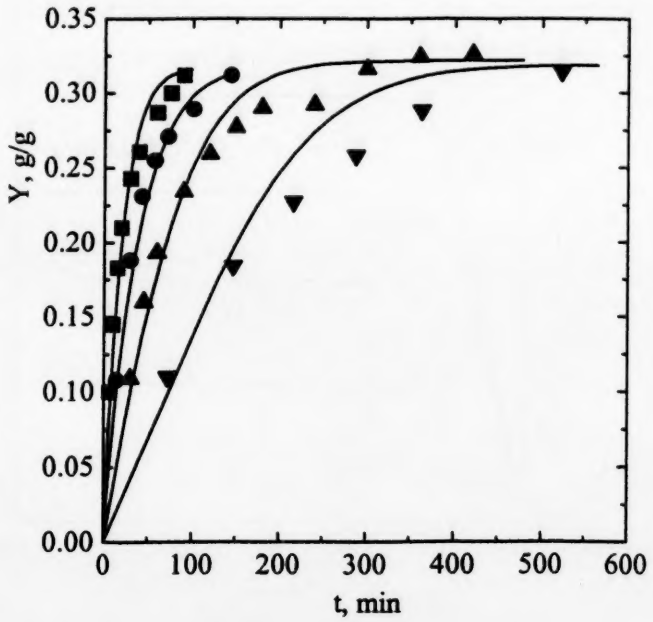

Fig. 3. Yield curves of sunflower oil at various flow rate of CO_2, $d_p = 3$ mm; ■, $W = 750$ g/min; ●, $W = 416.6$ g/min; ▲, $W = 166.6$ g/min; ▼, $W = 83.3$ g/min.

k_i resulted 4.1×10^{-7} m/s. In this case too the oil yield obtained in the used extraction time decreased with the increase of seed particle size (see Fig. 9) confirming the conclusions reached in the previous paragraphs.

We modeled tomato extraction yield data in the same manner as previously described and obtained a best fit value of k_i of 3.0×10^{-7} m/s.

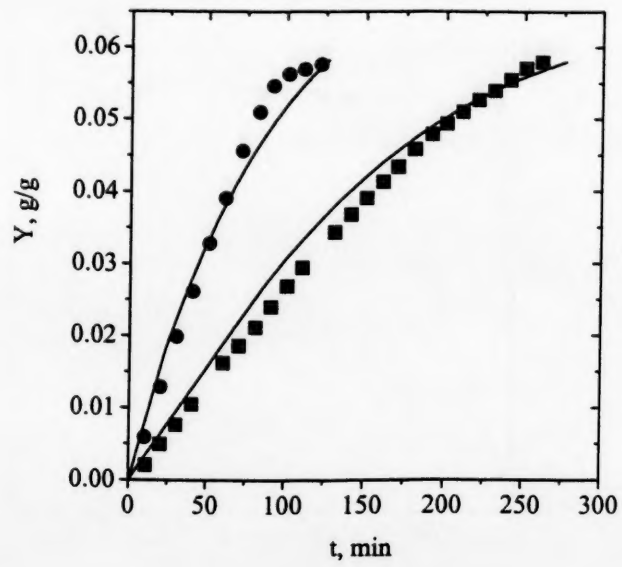

Fig. 5. Yield curves of coriander oil at various CO_2 flow rates, $d_p = 0.56$ mm; ■, $W = 213$ g/min; ●, $W = 86$ g/min.

Peanut oil was extracted by Goodrum et al. [30] using liquid CO_2 at 550 bar and 25°C. They used a flow rate of 72 g/min and particle diameters between 1 and 4 mm. Though liquid and not supercritical CO_2 was used in these experiments, we decided to use this data since we expect that liquid CO_2 can show a behavior similar to supercritical CO_2 in this kind of processes. Fitting of the experimental results was performed using an

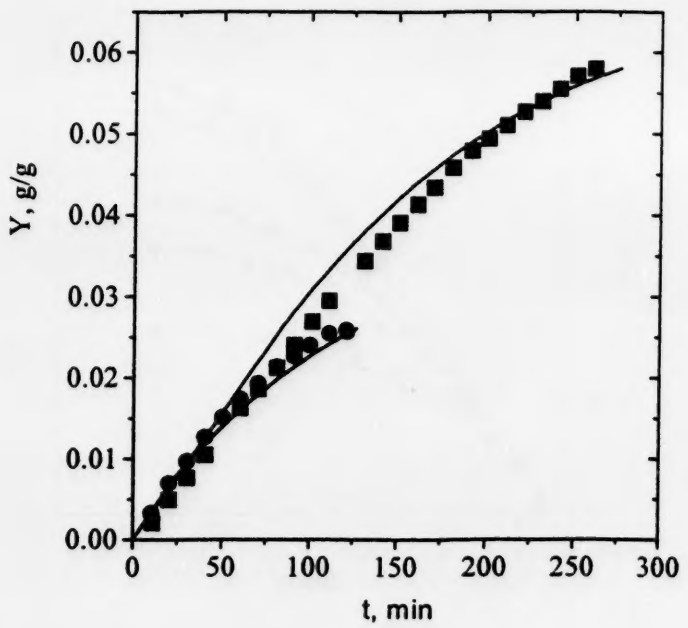

Fig. 4. Yield curves of coriander oil at various average particle diameters, $W = 86$ g/min; ■, $d_p = 0.56$ mm; ●, $d_p = 0.92$ mm.

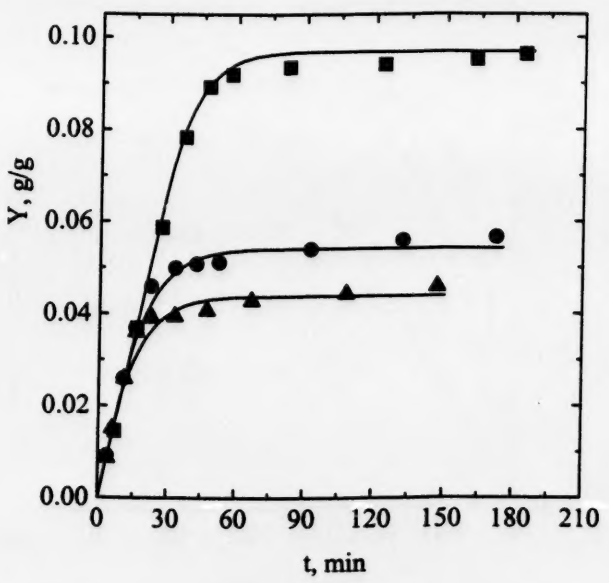

Fig. 6. Yield curves of grape oil at various average particle diameters, $W = 1.7$ g/min; ■, $d_p = 0.45$ mm; ●, $d_p = 0.73$ mm; ▲, $d_p = 0.81$ mm.

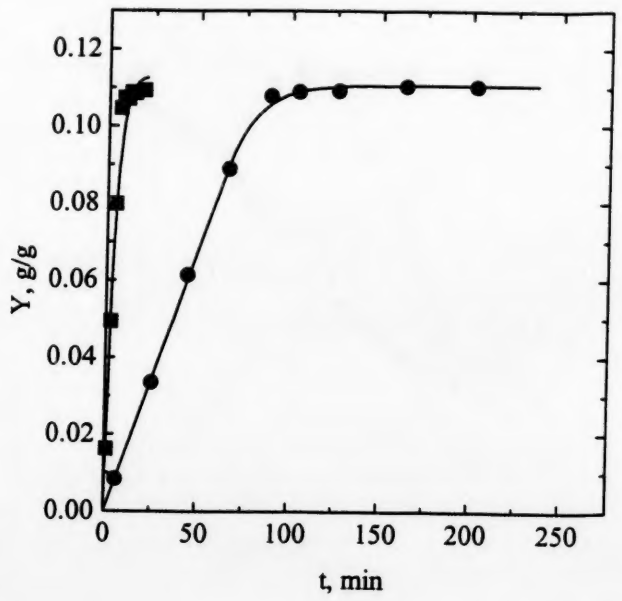

Fig. 7. Yield curves of grape oil at various CO_2 flow rates, $d_p = 0.36$ mm; ■, $W = 1.7$ g/min; ●, $W = 0.89$ g/min.

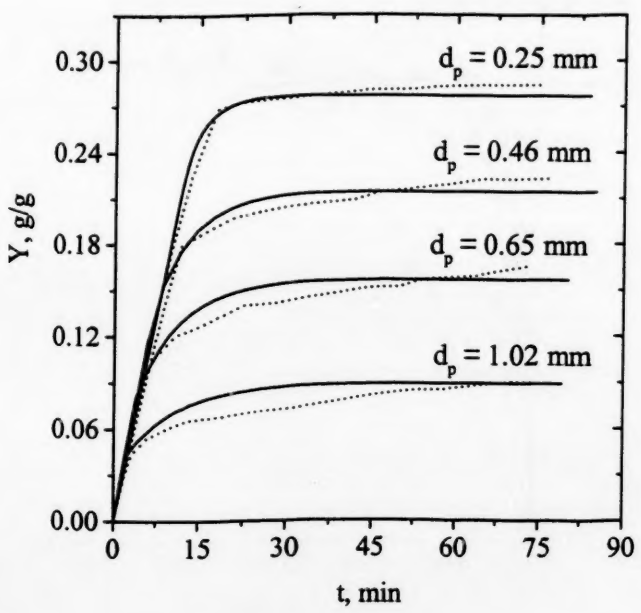

Fig. 9. Yield curves of tomato oil at various particle diameters, $W = 3.42$ g/min.

empirical equation. Therefore, no value of k_i was found in this case.

In this case large particles diameters (tests 2–5) give very low values of free oil and very different asymptotic oil yields for the given extraction time were obtained. This fact confirms the influence of particle size on the efficiency of the extraction process also when liquid CO_2 is used.

Our modeling results have been obtained in the usual manner and are reported in Fig. 10 together with the experimental data. In this case the best fit value of k_i is 3.0×10^{-7} m/s.

Almond oil supercritical extraction was performed by our research group [19] operating at 300 bar and 50°C at two different particle diameters (0.3 and 0.7 mm) and at two different CO_2 flow rates (12 and 23.3 g/min). The same model as the one proposed in this work was used with only one adjustable parameter. However, we refit the

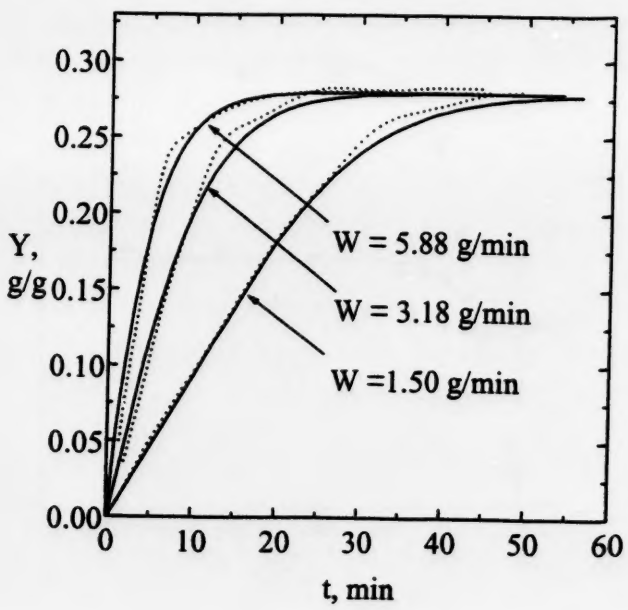

Fig. 8. Yield curves of tomato oil at various CO_2 flow rates, $d_p = 0.25$ mm.

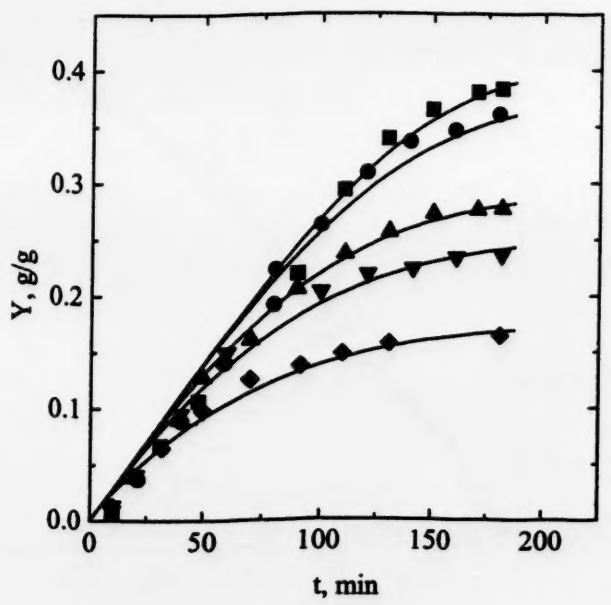

Fig. 10. Yield curves of peanut oil at various average diameters, $W = 72$ g/min; ■, $d_p = 1.1$ mm; ●, $d_p = 1.4$ mm; ▲, $d_p = 2$ mm; ▼, $d_p = 2.8$ mm; ◆, $d_p = 4$ mm.

experimental results since now we are using a more efficient numerical routine. We obtained a different best fit value for k_i with respect to our previous work with k_i is 9.2×10^{-8} m/s. The decrease of oil yield with particle size was observed also in this case. No figures are proposed for almond oil extraction since similar modeling results were previously published [19].

Fennel oil extraction was also performed by our research group [20] operating at 200 bar and 40°C using 0.372 mm particle and various CO_2 flow rates (between 8.3 and 24.9 g/min). The model used is the one proposed in this work. No refit of the experimental data was necessary in this case since the same numerical routines were used. The best fit value of k_i is 8.0×10^{-8} m/s. No figures are proposed for this case since the same results have been previously published [20]. This case has been added in the work only for sake of completeness of the comparison.

Some general characteristics emerge from an overall analysis of the experimental data and of the modeling results.

Solubility (C_0) values calculated from the initial slope of the experimental data are similar to the ones obtained using the Del Valle and Aguilera correlation [30]. These authors proposed the following equation:

$$C_s = \frac{(\exp(40.361 - 18708/T + 2186840/T^2) * (0.001\rho)^{10.724})}{\rho} \quad (14)$$

to describe the oil solubility in supercritical CO_2. The correlation is valid in a range of pressures between 150 and 800 bar. Where C_s is the solubility of oil in supercritical CO_2 expressed in g/g, T the temperature in Kelvin and ρ is the density of the supercritical fluid in kg/m^3. Table 4 shows the comparison between the values of C_0 and those evaluated using Del Valle and Aguilera correlation [31].

As it can be seen from Table 4, the values of C_0 and C_s are in good agreement, the maximum deviation between solubility values calculated from the experimental data and from correlation was obtained for tomato seed oil, where C_0 is two times larger than C_s. We used this correlation also to evaluate peanut oil solubility in liquid CO_2. Also in this case, the correlation gives a solubility value in reasonable agreement with the experimental data. These results confirm that the seed oil located on the particle surface is not connected (for example, adsorbed) on the solid structure and solubility equilibrium controls the first part of the SFE process. These conclusions are in agreement with some of the hypothesis of the proposed model.

Table 4
Equilibrium oil concentration at different extraction conditions[a]

Seed	C_0 (g/g)	C_s (g/g)
Sunflower	0.011	0.006
Coriander	0.004	0.005
Grape	0.006	0.006
Tomato	0.008	0.004
Peanut	0.018	0.015
Almond	0.011	0.007
Fennel	0.002	0.002

[a] C_0 has been calculated from the initial slope of the experimental data, whereas, C_s has been evaluated using the Del Valle and Aguilera [31] correlation.

A second general conclusion is that the use of particle diameters larger than about 0.5 mm, in connection with internal mass transfer resistance values and with the extraction time, produces an apparent or real reduction of the asymptotic oil yield. This phenomenon has been attributed to a low efficiency of the solvent access to the inner part of the particles. Indeed, for very long extraction times similar asymptotic oil yields should be obtained also for very large particle sizes despite the low efficiency of the solvent penetration in the core of larger particles. When the different sets of experiments have been performed at the same particle size, as in the case of sunflower (3 mm particles), this phenomenon is obviously not evidenced.

Moreover, the experimental results for larger particles practically do not show the first linear part of the extraction yield. It can mean that the quantity of broken cells on the particle surface is negligible when compared with the intact cells or

the quantity of oil contained in broken cells is not sufficient to reach equilibrium conditions. This phenomenon is particularly evident in the case of peanut oil extraction in which experiments were performed using particles with mean diameters up to 4 mm (see Fig. 10).

However, the production of very small particles can largely increase the grinding costs and could produce bed caking with the formation of channels along the extraction bed in which the supercritical solvent can preferentially flow, thus reducing the extraction efficiency. Therefore, an optimization of particles diameter is necessary.

The limit behaviors of very large particles with very reduced quantities of free oil and of very small particles with practically all freely available oil are correctly described by the proposed mathematical model. Indeed, if very large particles are used the free oil quantity becomes negligible and $\phi_f = 0$ and $\Psi = 0$. Therefore, Eq. (2) is automatically excluded from the computation. When the seed particles are very small it results $\phi_t = 0$ and $P = 0$ and Eq. (3) is automatically excluded from the computation.

We obtained a fair good modeling in all the studied cases. Though better fittings have been in the case of seeds with the higher oil content. However, the comparison of our modeling results with those obtained by the referenced authors, shows that they also obtained a general fair good modeling of the experiments. Indeed, the superiority of our model when compared with the ones proposed by the other authors does not rely on a better fitting of experimental results, but its major merits descend on the overall coverage of results; the consistent physical hypothesis and the consistent calculation of k_i values for the various seeds.

To support this last consideration in Table 5, we summarized the best fit values of the internal mass transfer coefficient k_i for the various seeds obtained in this study and those obtained by the other authors.

The best fit values of k_i found for the various seeds in this work span along less than two orders of magnitude whereas, the values obtained by the other authors cover about five orders of magnitude. This result means that a more consistent evaluation of k_i has been obtained in our study.

Another point to be discussed is the influence of the seed structure on the internal mass transfer resistance. The seed structure can be described as formed by cellulose and lignin. Lignin is a very compact natural polymer with a higher degree of polymerization than cellulose. Therefore, lignin could be practically inaccessible to the supercritical fluid and lignin content of the various kind of seed can strongly influence mass transfer resistance, i.e. the internal mass transfer resistance increases with lignin content of the seed. The existence of lignin structures can also give another explanation for the oil yield reduction for the larger seed particles, in these particles some of the seed lignin structures could not be destroyed by grinding; therefore, there will be some internal part of the particle that cannot be accessed by the solvent. Consequently, the aliquot of oil contained into these inaccessible structures is not extracted at all and a real oil yield reduction is obtained.

Table 5
Best fit values of the internal mass transfer coefficient k_i for the various seeds proposed in this study and by the other authors that performed seed oil supercritical extraction modeling

Seed	P (bar)/T (°C)	k_i (m/s)	k_i (m/s)	References
Sunflower	280/40	4.0×10^{-7}	2.2×10^{-5}	Perrut et al. [27]
Coriander	250/40	4.0×10^{-8}	9×10^{-9}	Catchpole et al. [29]
Grape	280/40	2.4×10^{-7}	6×10^{-10}	Sovovà et al. [18]
Tomato	240/40	3.0×10^{-7}	4.1×10^{-7}	Roy et al. [28]
Peanut	550/25	3.0×10^{-7}	–	–
Almond	300/50	9.2×10^{-8}	7.5×10^{-9}	Marrone et al. [19]
Fennel	200/40	8.0×10^{-8}	8.0×10^{-8}	Reverchon et al. [20]

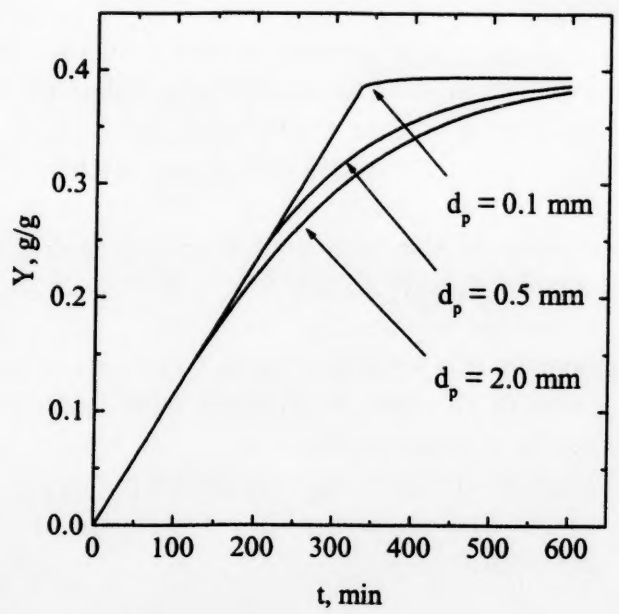

Fig. 11. Simulation of oil yield curves from a generic seed at different values of the particle diameter for $k_i = 3 \times 10^{-8}$ m/s.

At this point, we tried to simulate the oil yield behavior for a generic seed assuming that supercritical extraction has been performed at 280 bar and 40°C using a CO_2 flow rate of 25 g/min and that the oil-bearing cells are spherical with a mean diameter of 20 μm. The oil content is the seed was fixed at 40% by weight. Then, we used the mathematical model for three particle diameters (0.1, 0.5 and 2 mm) and with two different internal mass transfer coefficients, 3×10^{-8} and 3×10^{-9} m/s. The resulting oil yield simulated curves are reported in Figs. 11 and 12.

The first linear part of the oil yield curves is showed to depend not only on the free oil extraction but also on the extraction of tied oil located near the particle surface and is related to the value used for the internal mass transfer coefficient. It indicates that equilibrium conditions are reached also during the extraction of oil from unbroken cells located immediately under the particle surface. Indeed, from the comparison of Figs. 11 and 12 it is possible to see that very different extraction kinetics are obtained when the same particle size (and, thus, the same quantity of broken cells) is used with different values of k_f. The increase of the particle diameter together with the increase of mass transfer resistance is also demonstrated to control the shape and the attainment of the complete oil extraction. The increase of particle size in Fig. 11 with a k_i value of 3×10^{-8} produces a smooth transition between the two extraction regimes and the attainment of a quasi asymptotic oil yield for all the considered particle sizes within 600 min extraction. The use of the same particle sizes with a k_i value of 3×10^{-9} produce very different results. A sharp transition between the linear part and the mass transfer controlled part of the extraction process can be observed for 0.5 and 2 mm particles. Also the extraction yields obtained in 600 min for the same particle sizes are very far from the complete extraction value.

No inaccessible volume has been introduced in the simulations performed. Nevertheless, very different yields at 600 min have been simulated as reported in Fig. 12. Though this result is not conclusive about the existence or not of a non-accessible volume inside the larger particles, it demonstrates that a combination of particle diameter and mass transfer resistance is sufficient to produce lower yields with respect to the effective oilseed content for the extraction times selected for simulation.

A final question is, can this model be valid for all seed structures existing in the nature? Vegetable structures are not only very complex but also plants have been adapted to different condi-

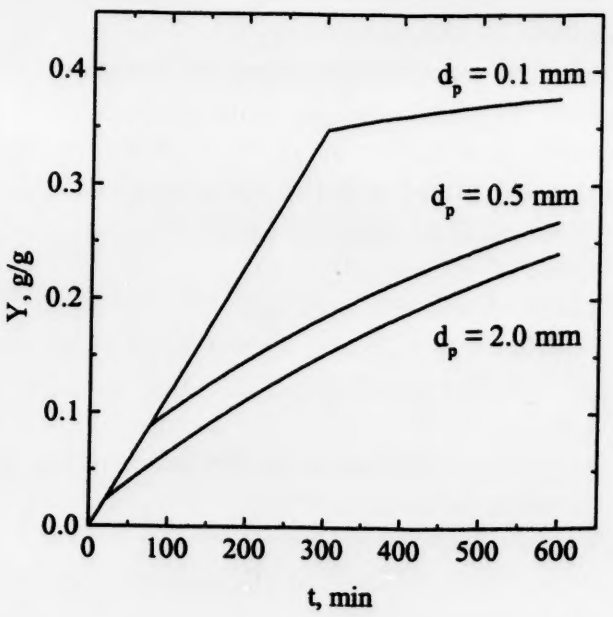

Fig. 12. Simulation of oil yield curves from a generic seed at different values of the particle diameter for $k_i = 3 \times 10^{-9}$ m/s.

tions. Therefore, it happened that we found an exception for seed structure when we studied hiprose seed oil supercritical extraction. This seed is characterized by a very low oil content and SEM analysis of its microstructure showed that it did not develop specialized oil-bearing structures. In this case, seed oil is contained in very long channels that form the vascular structure of the seed. The oil is still present in aliquots of free oil and difficult to be extracted oil, therefore, a different model was applied to explain all the experimental evidences [32].

5. List of symbols

a specific surface of the solid (1/cm)
C solute concentration in the solvent in terms of mass of solute per unit mass of solvent (g/g)
C_0 solute concentration in the solvent at the beginning of extraction (g/g)
D_L axial dispersion (m^2/s)
d_p particle diameter (cm)
k_f mass transfer coefficient from the free oil phase to the solvent (m/s)
k_i mass transfer coefficient from the tied oil phase to the solvent (m/s)
K_p seed oil equilibrium constant between the tied oil phase and the solvent (g/g)
K_ψ seed oil equilibrium constant between the free oil phase and the solvent (g/cm^3)
m_0 mass of seed charged (g)
m_e mass of extracted oil (g)
m_s mass of solvent used (g)
P solute concentration in the solid in terms of mass of solute per unit mass of non-soluble solid (g/g)
P_0 solute concentration in the solid at the beginning of extraction (g/g)
t extraction time (min)
u superficial velocity of the solvent (cm/min)
Y extraction yield (−)
Y_∞ asymptotic extractable oil yield (−)
z axial coordinate in the extractor (cm)

Greek letters

ε voidage of the extraction bed (−)
ϕ_f fraction of the particle volume filled by the free oil phase (−)
ϕ_t fraction of the particle volume filled by the tied oil phase (−)
ρ_e density of the untreated particles (g/cm^3)
ρ_f solvent density (g/cm^3)
ρ_o vegetable oil density (g/cm^3)
ρ_s density of the non-soluble solid (g/cm^3)
ψ ratio of the free oil volume with respect to the broken cells (−)
ψ_0 ratio of the free oil volume with respect to the broken cells at the beginning of extraction (−)

References

[1] M. Taniguki, T. Tsuji, M. Shibata, T. Kobayashi, Extraction of wheat germ with supercritical carbon dioxide, Agric. Biol. Chem. 49 (1985) 2367.
[2] S.M. Fors, C.E. Ericksson, Characterization of oil extracted from oats by supercritical carbon dioxide, Lebensmittel Wiss. U. Technol. 23 (1990) 390.
[3] D.D. Christianson, J.P. Friedrich, G.R. List, K. Warner, E.B. Bagley, A.C. Stringfellow, G.E. Inglett, SFE of dry milled corn germ with carbon dioxide, J. Food Sci. 49 (1984) 229.
[4] G.R. List, J.P. Friedrich, J. Pominsky, Characterization and processing of cottonseed oil obtained by extraction with supercritical carbon dioxide, J. Am. Oil Chem. Soc. 61 (1984) 1847.
[5] J.M. Snyder, J.P. Friedrich, D.D. Christianson, Effect of moisture and particle size on the extractability of oils from seed with supercritical CO_2, J. Am. Oil Chem. Soc. 61 (1994) 1851.
[6] R. Eggers, U. Sievers, W. Stein, High-pressure extraction of oil seed, J. Am. Oil Chem. Soc. 62 (1985) 1222.
[7] M.E. Ramsay, J.T. Hsu, R.A. Novak, W.J. Reigtler, Processing rice bran by SFE, Food Technol. (1991) 98.
[8] F. Favati, J.W. King, M. Mazzanti, Supercritical carbon dioxide extraction of evening primerose oil, J. Am. Oil Chem. Soc. 68 (1991) 422.
[9] E. Stahl, K.W. Quirin, R.J. Blagrove, Extraction of seed oils with supercritical carbon dioxide: effect on residual proteins, J. Agric. Food Chem. 32 (1984) 938.
[10] J.M. Snider, J.P. Friedrich, D.D. Christianson, Effect of moisture and particle size on the extractability of oils from seeds with supercritical CO_2, J. Am. Oil Chem. Soc. 61 (2) (1984) 1851.

[11] A. Molero Gomez, W. Huber, C. Pereyra Lopez, E. Martinez de la Ossa, Extraction of grape seed oil with liquid and supercritical carbon dioxide, in: M. Perrut, G. Brunner (Eds.), Proceedings of the Third Symposium on Supercritical Fluids, Strasbourg, vol. 2, 1994, p. 413
[12] N.R. Bulley, M. Fattori, A. Meisen, Supercritical fluid extraction of vegetable seeds, J. Am. Oil Chem. Soc. 61 (1984) 1362.
[13] A.K.K. Lee, N.R. Bulley, M. Fattori, A. Meisen, Modelling of supercritical carbon dioxide extraction of canola oilseed in fixed beds, J. Am. Oil Chem. Soc. 63 (7) (1986) 921.
[14] M. Fattori, N.R. Bulley, A. Meisen, Carbon dioxide extraction of canola seed: oil solubility and effect of seed treatment, J. Am. Oil Chem. Soc. 65 (6) (1988) 968.
[15] M.B. King, O.J. Catchpole, Physico-chemical data required for the design of near-critical fluid extraction process, in: M.B. King, T.R. Bott (Eds.), Extraction of Natural Products Using Near-Critical Solvents, Blakie Professional, 1993, p. 184.
[16] H. Sovovà, Rate of vegetable oil extraction with supercritical CO_2 — I. Modelling of extraction curve, Chem. Eng. Sci. 49 (1994) 409.
[17] H. Sovovà, J. Kucera, J. Jez, Rate of the vegetable oil extraction with supercritical CO_2 — II. Extraction of grape oil, Chem. Eng. Sci. 49 (1994) 415.
[18] J. Stastova, J. Jez, M. Bartlova, H. Sovovà, Rate of the vagetable oil extraction with supercritical CO_2 — III. Extraction from sea buckthorn, Chem. Eng. Sci. 51 (1996) 4347.
[19] C. Marrone, M. Poletto, E. Reverchon, A. Stassi, Almond oil extraction by supercritical CO_2: experiments and modelling, Chem. Eng. Sci. 53 (1998) 3711.
[20] E. Reverchon, J. Daghero, C. Marrone, M. Mattea, M. Poletto, Supercritical fractional of fennel seed oil and essential oil: experiments and mathematical modeling, Ind. Eng. Chem. Res. 38 (1999) 3069.
[21] T. Bamberger, J.C. Erickson, C.L. Cooney, Measurement and model prediction of solubilities of pure fatty acids, pure tryglicerides, and mixtures of tryglicerides in supercritical carbon dioxide, J. Chem. Eng. Data 33 (1988) 327.
[22] E. Reverchon, Fractional separation of SCF extracts from marjoram leaves: mass transfer and optimization, J. Supercrit. Fluids 5 (1992) 256.
[23] E. Reverchon, Supercritical fluid extraction of essential oils and related materials, J. Supercrit. Fluids 10 (1997) 1.
[24] T. Funazukuri, C. Kong, S. Kagei, Effective axial dispersion coefficients in packed bed under supercritical condition, J. Supercrit. Fluids 13 (1998) 169.
[25] O.J. Catchpole, R. Berning, M.B. King, Measurement and correlation of packed bed axial dispersion coefficient in supercritical carbon dioxide, Ind. Eng. Chem. Res. 35 (1996) 824.
[26] L. Lapidus, G.F. Pinder, Numerical Solution of Partial Differential Equation in Science and Engineering, Wiley-Interscience/Wiley, New York, 1982.
[27] M. Perrut, J.Y. Clavier, M. Poletto, E. Reverchon, Mathematical modeling of sunflowers seed extraction by supercritical CO_2, Ind. Eng. Chem. Res. 36 (1997) 430.
[28] B.C. Roy, M. Goto, T. Hirose, Extraction rates of oil from tomato seeds with supercritical carbon dioxide, Jpn. J. Chem. Eng. 27 (1994) 768.
[29] O.J. Catchpole, J.B. Grey, B.M. Smalfield, Near-critical extraction of sage, celery and coriander seed, J. Supercrit. Fluids 9 (1996) 273.
[30] J.W. Goodrum, M.K. Kilgo, C.R. Santerre, Oilseed solubility and extraction modelling, in: J.W. King, G.R. List (Eds.), Supercritical Fluid Technology in Oil and Lipid Chemistry, AOCS Press, 1996, p. 101.
[31] J.M. Del Valle, J.M. Aguilera, An improved equation for predicting the solubility of vegetable oils in supercritical CO_2, Ind. Eng. Chem. Res. 27 (1988) 1551.
[32] E. Reverchon, A. Kaziunas, C. Marrone, Supercritical CO_2 extraction of hiprose seed oil: experiments and mathematical modelling, Chem. Eng. Sci. 55 (2000) 2195.

ELSEVIER

Journal of Supercritical Fluids 19 (2001) 177–185

THE JOURNAL OF Supercritical Fluids

www.elsevier.com/locate/supflu

Incorporation of disperse dye in *N*,*N*-dimethylacrylamide modified poly(ethylene terephthalate) fibers with supercritical CO_2

W.L.F. Santos [a], M.F. Porto [a], E.C. Muniz [a], N.P. Povh [b], A.F. Rubira [a,*]

[a] *Departamento de Química, Universidade Estadual de Maringá, Av. Colombo, 5790, 87020-900, Maringá PR, Brazil*
[b] *Departamento de Engenharia Química, Universidade Estadual de Maringá, Av. Colombo, 5790 87020-900, Maringá PR, Brazil*

Accepted 4 August 2000

Abstract

The effects of modifying agents and dyeing conditions of dispersed dyes for PET films and fibers has been thoroughly studied. This research reports on the dye incorporation process of non-modified and *N*,*N*-dimethylacrylamide modified PET fibers with supercritical CO_2. Spectral analysis in the infrared region to the modified PET fibers showed peaks of the modifier, but the thermal stability of the modified fiber did not show variation when compared with the non-modified. The amount of disperse dye incorporated in the PET fibers was determined by UV–Vis spectroscopy at 579 nm through the dye extraction using *N*,*N*-dimethylformamide. A 2^4 factorial design was realized with the purpose to study the influence of variables in the dye incorporation process as well as their interaction effects. The pre-treatment of the PET fibers with *N*,*N*-dimethylacrylamide increases the amount of incorporated dye 3.8 times, in average. The main effect on the dye incorporation was the dyeing time for the modified fibers, but for the non-modified fibers, the pressure and the temperature presented analogous main effect © 2001 Elsevier Science B.V. All rights reserved.

Keywords: Poly(ethylene terephthalate); *N*,*N*-dimethylacrylamide; Disperse dye; Supercritical CO_2; Factorial design

1. Introduction

Woven fibers of poly(ethylene terephthalate), PET, represent the largest percentage among synthetic fibers in the market [1], and are used as pure material or mixed with cellulose. It is utilized in the making of different articles, like, curtains, caps and others. In order to have a better appearance and due to the utilization of these articles, addition of dyes in the manufacturing process is required.

Among synthetic fibers, PET has the most compact and crystalline [2] structure, except for some kinds of polyester, of low commercial use. These fibers are dyed with disperse dyes, insoluble in water (5–30 mg/l), which are applied with dispersing agents to achieve stable dispersions [2].

* Corresponding author.
E-mail address: afrubira@uem.br (A.F. Rubira).

0896-8446/01/$ - see front matter © 2001 Elsevier Science B.V. All rights reserved.
PII: S0896-8446(00)00083-8

Several authors [2–8] have studied the effects of modifying agents and dyeing conditions of dispersed dyes for PET films and fibers. According to Stinson and Obendorf [6], non-modified PET absorbs only 0.4% of water, and does not swell in water. This lack of interaction between PET and the aqueous dyebath requires either the use of high temperature or high-pressure systems. These conditions allow the dyeing with disperse dyes to achieve industrially acceptable dyeing rates. In addition, low molecular weight organic compounds, called carriers (phenols, amines, aromatic hydrocarbons, esters, etc.), which are rapidly absorbed, have been used to accelerate the dyeing rate [2].

Saligram and collaborators [7], report a dyeing using sonication in order to form and break small bubbles, resulting in a temperature and pressure increase at a microscopic level. This cavitation causes agitation, making the dyeing better at low temperatures achieving levels comparable with dyeing at boiling using carriers.

Knittel and collaborators [8], showed that synthetic fibers like PET can be dyed using carbon dioxide in supercritical state as solvent, avoiding the water pollution and the need of drying with excellent firmness levels.

The use of supercritical fluid in the dye impregnation of textile materials have been studied due to its excellent properties like density, viscosity, diffusivity and dielectric constant. The dielectric constant of supercritical fluids can be significantly changed in the supercritical region and generate solvent properties in substances that do not exhibit such properties in their liquid or gaseous state [9].

According to Valldeperas [10], dyeing studies carried out in polyester and carbonic anhydride at 140°C and 250 bar, using a series of disperse dyes, showed that the dye absorption level and the fastness property obtained are comparable with the ones of the conventional dyes at high temperatures, without the need of the redox process on the batch preparation. Although there are no studies concerning the economical viability, its ecological implications are evident. Valldeperas [10] has shown the advantages of the use of supercritical CO_2 in dyeing processes in comparison with the conventional ones.

Studies on the solubility of azo and anthraquinone disperse dyes have been published and may be used as additional information to the studies of PET dyeing in supercritical CO_2 [11].

N,*N*-dimethylacrylamide has been used in the biomaterials area, due to its hydrophilic character, in the obtention of polymeric materials compatible to blood and tissue. The grafting of the *N*,*N*-dimethylacrylamide monomer in polymeric substrates like poly(dimethylsiloxane), to be applied as catheter [12], and the obtention of selective semipermeable amphiphilic membranes [13], used to determine the diffusional characteristics of glucose, insulin and albumin, are applications indicating that the *N*,*N*-dimethylacrylamide is not harmful to human body.

In previous work [14,15] we showed that the pre-treatment of the PET films with *N*,*N*-dimethylacrylamide, favors the dye incorporation in the fiber during the dyeing in an aqueous medium. The use of this pre-treatment decreases the dyeing time and increases the dyeing incorporation in approximately three times, in comparison with the non-modified PET dyeing process.

The objective of this study was the investigation of the supercritical CO_2-aided dye incorporation process in non-modified and *N*,*N*-dimethylacrylamide modified PET fibers. By using a fatorial design, the variables of time, temperature and pressure of dyeing, as well as treatment with modifier, were investigated.

2. Experimental

2.1. Materials

The commercial dye used was Samaron HGS (Dy Star)® (Disperse Blue 79) ($C_{23}H_{25}BrN_6O_9$). The solvent (modifier) was *N*,*N*-dimethylacrylamide(C_5H_9NO) (Aldrich). Commercial samples of PET fibers were kindly supplied by COCAMAR, Maringá, Brazil. *N*,*N*-dimethylformamide was also used to extract the dye from the fiber after dyeing process. Fig. 1 shows the polymer, dye and modifier structures.

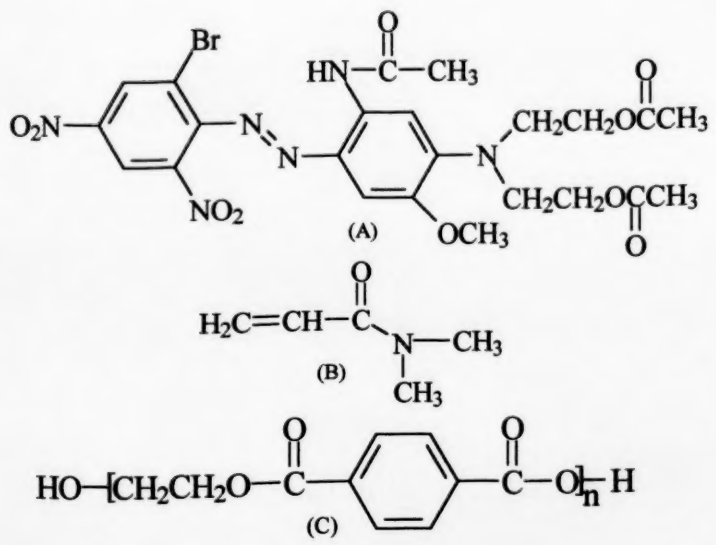

Fig. 1. (A) Dye, Samaron HGS (Dy Star)® (C I Disperse Blue 79); (B) Modifier, *N*,*N*-dimethylacrylamide; (C) Polymer, Poly(ethylene terephtalate).

2.2. Procedures

PET fibers in coil form were immersed in *N*,*N*-dimethylacrylamide modifier solvent, under agitation at 90°C for 15 min. Afterwards the modified fiber was centrifuged to eliminate the excess of *N*,*N*-dimethylacrylamide. In the dyeing experiments, it was used 3 wt.% of dye in relation to the mass fiber. The dyestuff amount is then in large excess compared with average solubility of disperse dyes in supercritical CO_2 [16–18]. The excess of dyestuff amount is in the range 4–95 times compared with the total amount absorbed from the PET fiber.

Modified and non-modified PET fibers were placed in a dyeing cell with supercritical CO_2 as schematized in Fig. 2. CO_2 coming from the storage tank (A) is compressed by a piston (B) until reaches the requested pressure. The gas goes through: a solenoid valve (C); a one-way valve (D); a flow distributor (E) and reaches the infusion cell (F) in the thermostatized bath; (G) maintained at the requested temperature. By using two thermocouples (one in the bath and the other in the infusion cell) the requested temperature in the infusion cell inner region is controlled. There is a

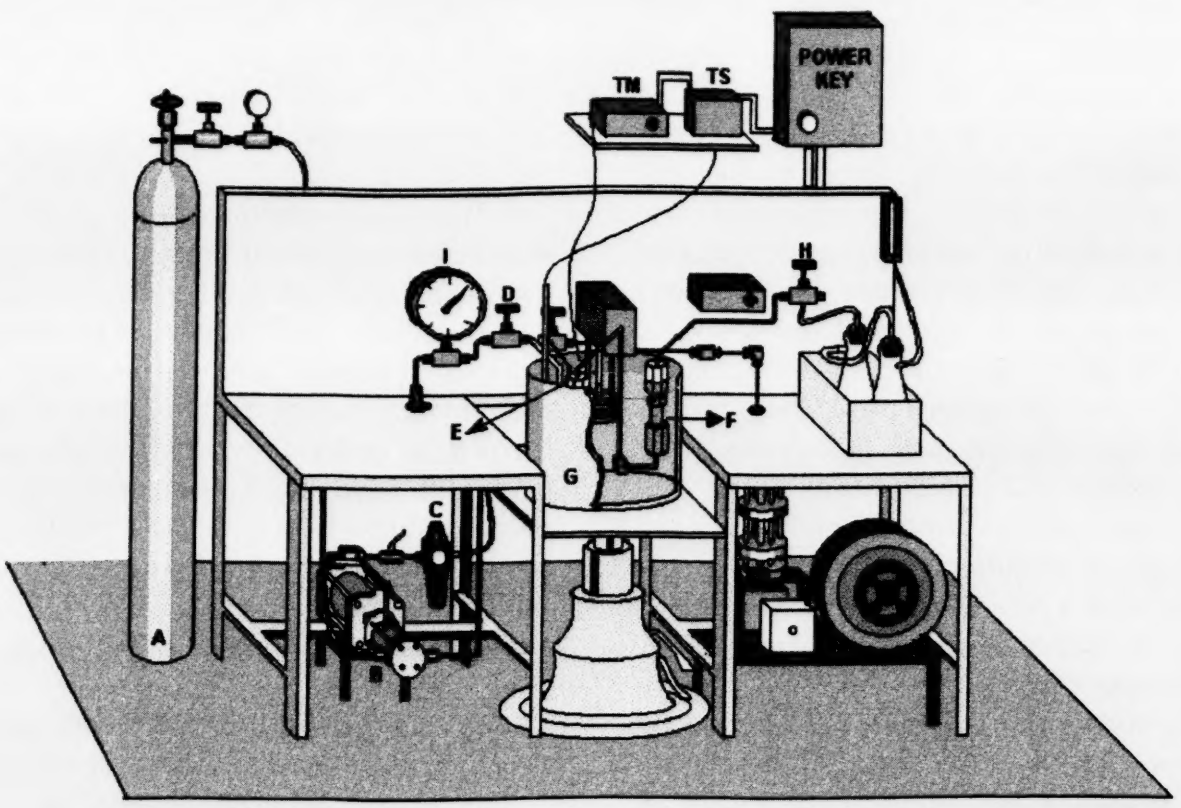

Fig. 2. Supercritical fluid equipment scheme; storage tank (A); piston (B); solenoid valve (C); one way valve (D); flow distributor (E); infusion cell (F); thermostatized bath (G); pressure valve (H) and manometers (I). TM, temperature measurer; TS, temperature set.

Table 1
Codified variables of each experiment of the 2^4 factorial design

Test	Dyeing temperature[a]	Dyeing pressure[b]	Dyeing time[c]	Pre-treatment with DMACr[d]
1	−	−	−	+
2	−	−	+	+
3	−	+	−	+
4	−	+	+	+
5	+	−	−	+
6	+	−	+	+
7	+	+	−	+
8	+	+	+	+
9	−	−	−	−
10	−	−	+	−
11	−	+	−	−
12	−	+	+	−
13	+	−	−	−
14	+	−	+	−
15	+	+	−	−
16	+	+	+	−

[a] Dyeing temperature (°C), (50 (−); 65(+).
[b] Dyeing pressure (kgf cm^{-2}), (140(−); 250(+)).
[c] Dyeing time, (30 min.(−); 3 h(+)).
[d] Pre-treatment, (without(−); with (+)).

pressure reducer valve in the exit (H). A manometer (I) measures the pressure drop in the line before the one-way valve. The sample and the dye were placed in individual supports inside the infusion cell. After, the temperature of bath was adjusted to the requested value and the exit valve was shut. With the compressor already regulated, the entrance valve is opened and the timer is trigged after the infusion cell has reached the requested pressure and temperature. After this operation, the exit valve is opened and the CO_2 is liberated to the atmosphere.

A factorial design was used with the purpose of analyzing the influence of each variable studied in the dye incorporation process as well as their interaction effects. The variables studied are the following — dyeing time, dyeing temperature, and pressure of CO_2 — in the dyeing process. Each variable was maintained in two levels. Table 1 shows the codified variables and the levels of the factorial design.

2.3. Measurements

Differential scanning calorimetry (DSC) measurements were performed in order to determine the glass transition temperature of modified and non-modified PET fibers. Thermogravimetric analysis (TGA) of non-modified and *N*,*N*-dimethylacrylamide modified PET fibers were performed in order to verify the thermal stability. The DSC and TGA measurements were made using a Shimadzu equipment, model 50. IR-ATR spectra of non-modified and *N*,*N*-dimethylacrylamide modified samples were obtained in the infrared region using a FTIR Bomen equipment. Scanning electron microphotographs (SEM) were taken using a JEOL JSM-6340F field emission scanning electron microscopy (FESEM).

The amount of absorbed dye on non-modified and *N*,*N*-dimethylacrylamide modified PET fibers was determined by UV–Vis spectroscopy at 579 nm[15], through the dye extraction using *N*,*N*-

dimethylformamide (DMF) and posterior measurement of dye absorption intensity. The samples were weighted, and then immersed in an extraction cell with *N*,*N*-dimethylformamide at 80°C. The extraction was carried out in three steps of 30 min each, using, respectively, the following solvent volumes 20, 20 and 10 ml.

3. Results and discussion

Fig. 3 shows FTIR spectra of PET fibers before (A) and after immersion in *N*,*N*-dimethylacrylamide (B). Spectral analysis of modified PET fibers, showed peaks of the modifier at 1647, 1612 and 1175 cm^{-1} (Fig. 3B) which were, respectively, attributed to carbonyl stretching, C=C stretching and C–N stretching of the modifier [19]. By comparison of spectra (A) and (B), the absorption bands can be attributed to *N*,*N*-dimethylacrylamide showing an evidence of it incorporation in the PET fibers. These peaks indicate the absence of a chemical interaction between the modifier and PET, as already observed by Ershov and collaborators [20] in studies using polyester fibers and acrylic copolymers.

The analysis of DSC data from non-modified (Fig. 4A) and *N*,*N*-dimethylacrylamide modified PET fibers (Fig. 4B) show that melting temperature (253°C) is not changed with the treatment process. A better defined glass transition temperature at about 70°C was observed in the curve of the modified PET fibers (B). The same behavior was found by Rubira and collaborators with PET films [15].

The decomposition temperature, at a 10% level, determined by TGA, for non-modified (Fig. 5B) and modified PET fibers (Fig. 5B) was 387 and 379°C, respectively. It is an evidence that the treatment does not alter the thermal stability of the polymer.

The scanning electronic microphotographs of the non-modified (Fig. 6A) and *N*,*N*-dimethylacrylamide modified PET fibers (Fig. 6B) show alterations in the modified fiber surface due to the *N*,*N*-dimethylacrylamide treatment. The modified fiber shows flatter surface than the non-modified fiber, probably due to the surface corrosion, but it was not possible to quantify the corrosion level.

The amount of dye absorbed is shown in Table 2. In order to highlight the data, they were divided in two groups. One of the groups is related

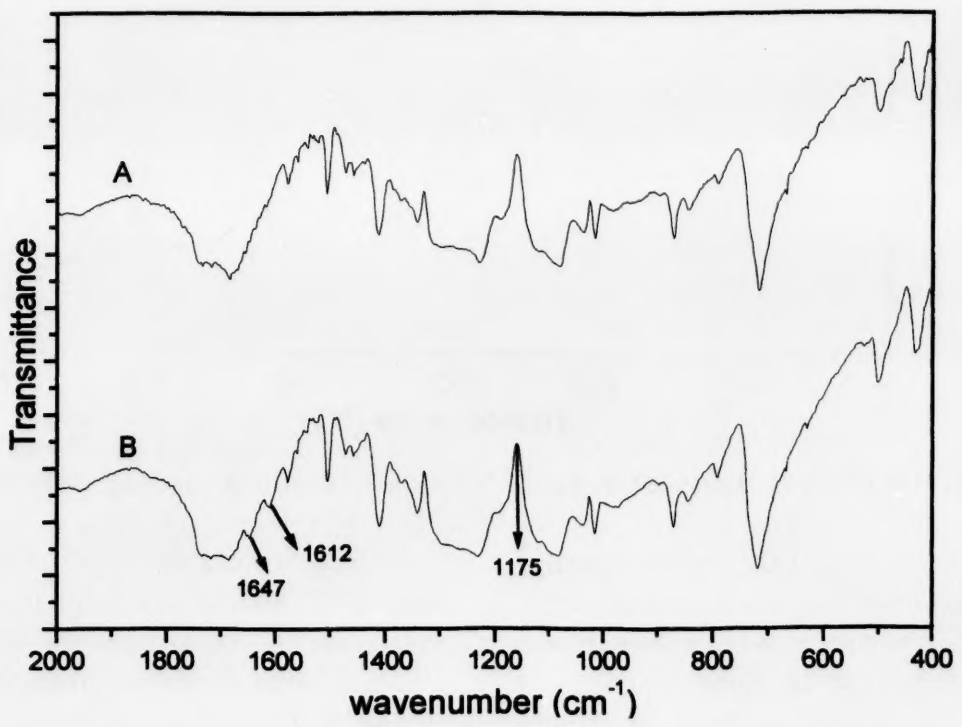

Fig. 3. FTIR spectra of non-modified (A) and *N*,*N*-dimethylacrylamide modified (B) PET fiber (obtained in KBr pellets).

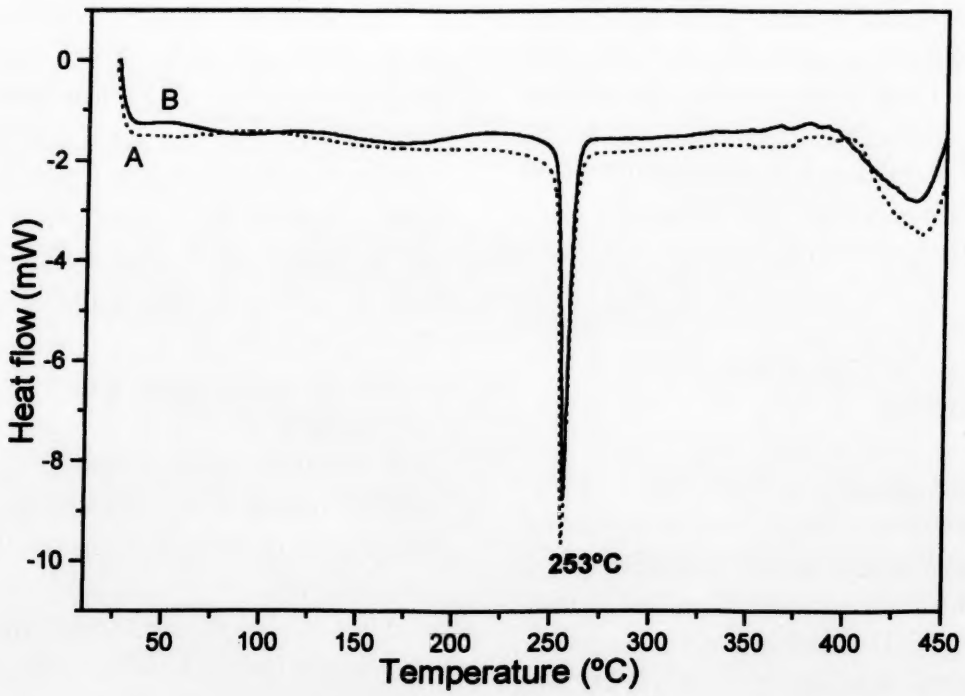

Fig. 4. DSC curves of non-modified (A) and *N*,*N*-dimethylacrylamide modified (B) PET fiber.

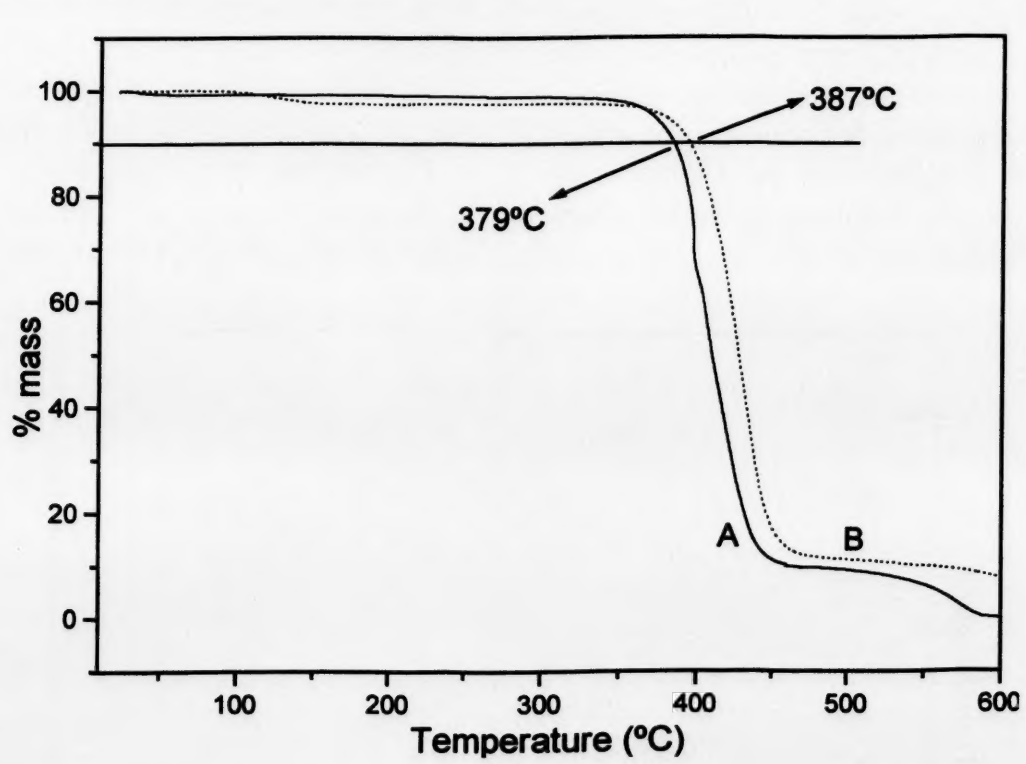

Fig. 5. TGA curves of non-modified (A) and *N*,*N*-dimethylacrylamide modified (B) PET fiber.

to the factorial design 2^3 of the *N*,*N*-dimethylacrylamide modified fiber that corresponds to the experiments designed as test 1–8 in Tables 1 and 2. Another group is related to eight experiments carried out with non-modified PET fiber, described as test 9–16 in Tables 1 and 2.

Table 3 shows the main effect and the interaction effect of the variables involved in the factorial design, described as test 1–8, for the *N*,*N*-dimethylacrylamide modified fiber in Tables 1 and 2. From data in Table 3 can be observed that the dyeing time presents a higher main effect

on the amount of incorporated dye. A significant interaction effect between dyeing time and temperature variables is also observed. These data match very well with the dyeing conditions data from literature [4,5,21–23] and can be understood considering that when the *N*,*N*-dimethylacrylamide is used to modify PET fiber, the surface as well as the fiber bulk were in perfect dyeing condition as pointed out by Needles and Walker [21], Bendak and El-Marsafi [4,5] and Sicardi and collaborators [23]. For example they showed that even though the surface of PET was very crystalline, the interior regions are less crystalline [18] and they also showed that the treatment of the fiber with organic solvents such as dimethylformamide decreases the crystalline appearance of the surface, making the dyeing easier [3–5]. Sicardi and collaborators [23] showed that the diffusion coefficients and solubility of disperse dyes in PET, during impregnation with a supercritical fluid, increase with increasing temperature. They attributed this result to the increase in flexibility of the polymeric chains due to the temperature. They also found that rising the pressure results in a small increase in the diffusion coefficient and these findings were justified based on the CO_2 plasticizing effect. Based on our results and from data of the literature [4,21,23] it can be emphasized that the modifier *N*,*N*-dimethylacrylamide plasticize and swell the PET fibers increasing the chain flexilbility promoting the SCF-assisted dye infusion. In this way, it should be emphasized that the amount of dye that can be incorporated in a PET fiber is limited by the dyeing time and longer dyeing times increase the dye uptake of the fibers.

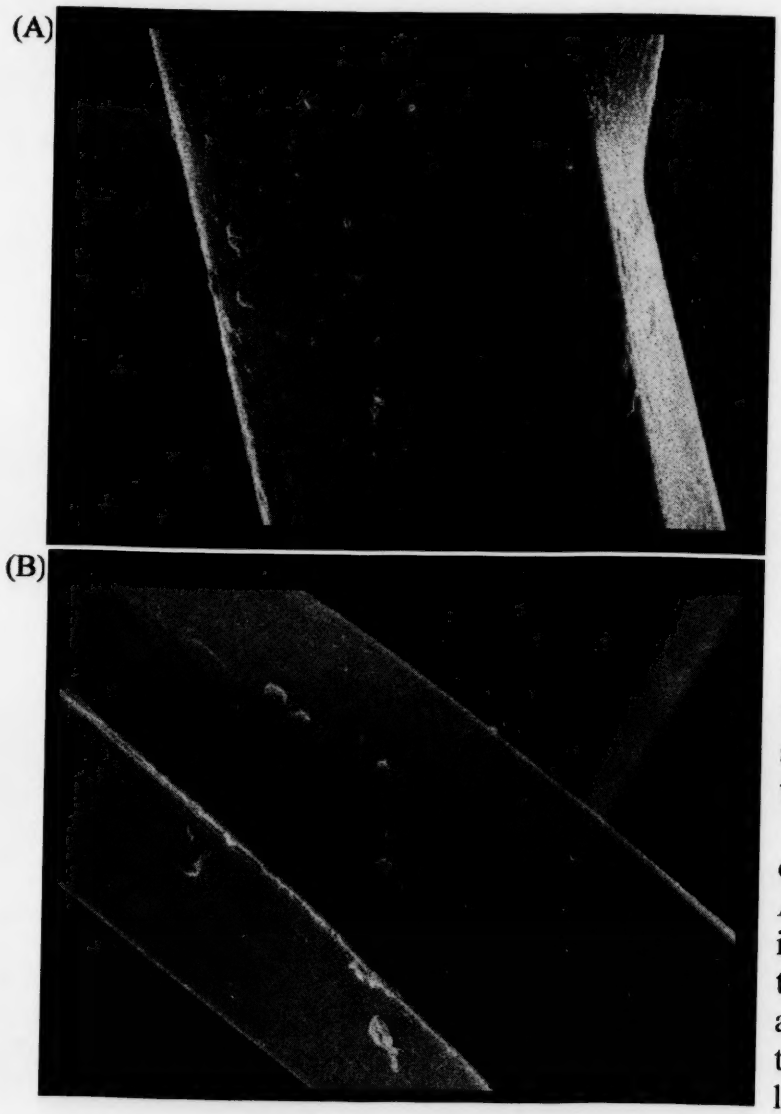

Fig. 6. Scanning electron microphotographs of non-modified (A) and *N*,*N*-dimethylacrylamide modified (B) PET fiber. Magnification, 3000 × .

On the other hand, to have a good dyeing of a non modified PET fiber we need, at first, to achieve the optimum SF-CO_2 dyeing conditions. Table 4 shows the main effect and the interaction effect of the variables involved in the factorial design, described as test 9–16, for the non-modified fiber in Tables 1 and 2. The results show a main analogous effect of the pressure and temperature on the amount of incorporated dye. These results are consistent with the data from other systems in which a semicrystalline polymer is annealed by plasticization with CO_2 allowing polymer chains to reorient to more thermodynamically favorable positions, forming crystallites [24–27]. For example, Lambert and Paulaitis [26] and Baldwin and Suh [27] observed maxima in the time-dependent sorption studies of CO_2 in PET. The decrease in CO_2 solubility and absorption at long times is attributed to an increase in crystallinity of PET.

By comparing the data of Table 2, it was shown out that when the fibers are submitted to the *N*,*N*-dimethylacrylamide treatment (test 1–8), it incorporates, on average, 3.8 times more dye than the non-modified PET fibers (test 9–16). From the above discussion it may pointed out that the treatment of PET fiber with *N*,*N*-dimethylacrylamide decreases the crystallinity of PET. The dyeing of such fibers using CO_2 in supercritical conditions is easier than the non modified PET fibers.

Table 2
Ratio of mass of absorbed dye and mass of fiber according to the 2^4 factorial design described on Table 1

Test	Mass of absorbed dye (M_a) (g) $\times 10^4$	Mass of fiber (M_f) (g)	Ratio $M_a/M_f \times 10^3$
1	0.649	0.0983	0.66
2	2.531	0.1122	2.26
3	2.243	0.1072	2.09
4	2.635	0.1164	2.26
5	0.466	0.0803	0.58
6	3.001	0.0989	3.03
7	2.112	0.1131	1.87
8	11.338	0.1343	8.44
9	0.309	0.1059	0.29
10	0.518	0.1150	0.45
11	0.309	0.0990	0.31
12	0.701	0.1208	0.58
13	0.832	0.2133	0.39
14	0.597	0.1192	0.50
15	2.008	0.1329	1.51
16	2.583	0.1228	2.10

Table 3
Main effect and interaction effects of the variables involved on the factorial design, described as test 1–8, in Tables 1 and 2

Variable	Main effect
Dyeing time	2.7×10^{-3}
Dyeing pressure	2.1×10^{-3}
Dyeing temperature	1.7×10^{-3}

Interaction effects

Dyeing time × dyeing pressure	Dyeing time × dyeing temperature	Dyeing pressure × dyeing temperature
0.70×10^{-3}	1.8×10^{-3}	1.3×10^{-3}

Table 4
Main effect and interaction effects of the variables involved on the factorial design, described as test 9 to 16, in Tables 1 and 2

Variable	Main effect
Dyeing time	0.28×10^{-3}
Dyeing pressure	0.71×10^{-3}
Dyeing temperature	0.72×10^{-3}

Interaction effects

Dyeing time × dyeing pressure	Dyeing time × dyeing temperature	Dyeing pressure × dyeing temperature
0.15×10^{-3}	0.70×10^{-3}	0.64×10^{-3}

4. Conclusion

The pre-treatment of the PET fibers using *N*,*N*-dimethylacrylamide as modifier increases the amount of incorporated dye 3.8 times, in average. Such process does not present damages to the environment, once (i) the modifier is a non toxic agent and it can be easily recovered; (ii) the dyeing process does not produce liquid effluents, but liberates only CO_2 as waste product. In this way, the dyeing of PET fibers, using supercritical CO_2, is an alternative technique for the incorporation of dispersed dye in PET.

References

[1] M.M. Shashin, Structure-property relationships in polyester fiber, Polym. Test. 14 (1995) 243–251.
[2] M.M. Shashin, Structure-property relationships in polyester fiber, Polym. Test. 14 (1995) 243–251.
[3] H.L. Needles, M.J. Park, The effect of *N*,*N*-dimethylformamide and polymer grafting on the morphology of polyester fibers in fabric substrate, J. Appl. Polym. Sci. 59 (1996) 1683–1698.
[4] A. Bendak, S. Elmarsafi, Some evaluations of the dyeing properties of modified polyester fibers, Ann. Chim-Rome 81 (1991) 141–154.
[5] A. Bendak, S. Elmarsafi, Penetration behavior of disperse dyes into modified polyester fibers, Ann. Chim-Rome 82 (1992) 603–613.

[6] R.M. Stinson, S.K. Obendorf, Simultaneous diffusion of a disperse dye and a solvent in PET film analyzed by Rutherford backscattering spectrometry, J. Appl. Polym. Sci. 62 (1996) 2121–2134.
[7] A.N. Saligram, S.R. Shukla, M. Mathur, Dyeing of polyester fibers using ultrasound, J. Soc. Dyers Colour 109 (1993) 263–266.
[8] D. Knittel, W. Saus, E. Schollmeyer, Water-free dyeing of textile accessories using supercritical carbon dioxide, Indian J. Fibre Text. Res. 22 (1997) 184–189.
[9] L.T. Taylor, Supercritical Fluid Extraction, Wiley, New York, 1996.
[10] J. Valldeperas, Possibilidades atuais e tendências futuras no tingimento por esgotamento, QuímicaTêxtil 19 (1996) 38–48.
[11] S.N. Joung, K.P. e Yoo, Solubility of disperse anthraquinone and azo dyes in supercritical carbon dioxide at 313.15 to 393.15 and from 10 to 25 MPa, J. Chem. Eng. Data 43 (1998) 9–12.
[12] A.T. Almeida, A.A.A Queirós, E.R. Barrak, O.Z. Higa, 'Estudo por TMA do PDMS após modificação por radiação ionizante para aplicação em bioengenharia', Proceedings of the 13°CBECIMAT, Curitiba-PR 4054-4060 (1998).
[13] S. Shamlou, J.P. Kennedy, R.P. Levy, Amphiphilic networks.10. Diffusion of glucose and insulin (and nondiffusion of albumin) through amphiphilic membranes, J. Biomed. Mater. Res. 35 (1997) 157–163.
[14] W.L.F. Santos, 'Filmes e Fibras de Poli(tereftalato de etileno) modificados com *N*,*N*-dimetil Acrilamida: Incorporação de corante disperso', Master Dissertation presented to Programa de Mestrado em Química Aplicada/UEM, 1999.
[15] W.L.F. Santos, M.F. Porto, E.C. Muniz, L. Olenka, M.L. Baesso, A.C. Bento, A.F. Rubira, Poly(ethylene terephthalate) films modified with *N*,*N*-dimethylacrylamide: incorporation of disperse dye, J. Appl. Polym. Sci. 77 (2000) 269–282.
[16] A.S. Ozcan, A.A. Clifford, K.D. Bartie, D.M. Lewis, Solubility of disperse dyes in supercritical carbon dioxide, J. Chem. Eng. Data 42 (1997) 590.
[17] C.B. Kautz, B. Wagner, G.M. Schneider, High-pressure solubility of 1,4-*bis*-(*n*-alkylamino)-9,10-anthraquinones in near- and supercritical carbon dioxide, J. Supercrit. Fluids 13 (1998) 43.
[18] D. Tuma, G.M. Schneider, High-pressure solubility of disperse dyes in near- and supercritical fluids: measurements up to 100 Mpa by a static method, J. Supercrit. Fluids 13 (1998) 37.
[19] C.J. Pouchert, The Aldrich Library of Infrared Spectra, third ed., Aldrich Company Inc, Milwaukee, 1981, p. 435.
[20] A.A. Ershov, V.L. Tsailingol'd, O.P. Lopatina, L.I. Gandurin, O.K. Kozlova, Interaction of acrylic copolymers with polyester fibers, Zhurnal Prikladnoi Khimii 64 (1991) 613–617.
[21] H.L. Needles, C. Walker, Characterization of the internal morphology of heat- and solvent-modified polyester fibers, J. Appl. Polym. Sci. 47 (1991) 249–262.
[22] J.V. Schnitzler, R. Eggers, Mass transfer in polymers in a supercritical CO_2-atmosphere, J. Supercrit. Fluids 16 (1999) 81.
[23] S. Sicardi, L. Manna, M. Banchero, Diffusion of disperse dyes in PET films during impregnation with a supercritical fluid, J. Supercrit. Fluids 17 (2000) 187–194.
[24] J.-J. Shim, S.-H. Chang, S.-C. Park, Phase equilibria of supercritical fluid-polymer systems, J. Supercrit. Fluids 13 (1998) 113.
[25] D. Bourbon, Y. Kamiya, K. Mizoguchi, Sorption and dilation properties of poly(para-phenylene sulfide) under high-pressure carbon-dioxide, J. Polym. Sci., Polym. Phys. Ed. 28 (1990) 2057.
[26] S.M. Lambert, M.E. Paulaitis, Crystallization of poly(ethylene terephthalate) induced by carbon dioxide sorption at elevated pressures, J. Supercrit. Fluids 4 (1991) 15–23.
[27] D.F. Baldwin, N.P. Suh, Viscoelastic behavior of microcellular plastics, Proceedings of SPE-ANTEC, 1503, 1992.

ELSEVIER

Journal of Supercritical Fluids 19 (2001) 187–198

THE JOURNAL OF Supercritical Fluids

www.elsevier.com/locate/supflu

Solubilities and diffusion coefficients of carbon dioxide in poly(vinyl acetate) and polystyrene

Yoshiyuki Sato, Tadao Takikawa, Shigeki Takishima, Hirokatsu Masuoka *

Department of Chemical Engineering, Hiroshima University, 1-4-1 Kagamiyama, Higashi-Hiroshima 739-8527, Japan

Received 11 March 2000; received in revised form 24 June 2000; accepted 11 September 2000

Abstract

Solubilities of carbon dioxide in poly(vinyl acetate) (PVAc) were measured at temperatures from 313.15 to 373.15 K and pressures up to 17.5 MPa. Diffusion coefficients of carbon dioxide in PVAc were also measured at 313.15 K and pressures up to 7 MPa. Solubilities and diffusion coefficients of carbon dioxide in molten polystyrene (PS) were studied at temperatures from 373.15 to 473.15 K and pressures up to 20 MPa. An apparatus using a magnetic suspension balance (MSB) was constructed for the measurements. The solubilities in the PVAc and the PS were in good agreement with literature data. The solubility in both polymers were correlated with the Sanchez and Lacombe equation of state to within an average relative deviation of 3.6 and 1.6% for PVAc and PS systems, respectively. The diffusion coefficients in PS were correlated with free volume theory of Kulkarni and Stern to within 10% of relative average deviation. © 2001 Elsevier Science B.V. All rights reserved.

Keywords: Solubility; Diffusion coefficient; CO_2; Polystyrene; Poly(vinyl acetate)

1. Introduction

Polymeric foams are widely used as heat insulators, food trays, and support materials, because of their many advantageous characteristics such as low thermal conductivity, light weight, and high impact strength. CFC-11 (trichlorofluoromethane) and CFC-12 (dichlorodifluoromethane) had been used as physical blowing agents for these types of industrial foaming processes. However, since production of these gases has been prohibited, new environmentally benign alternative blowing agents such as carbon dioxide and nitrogen are being considered. For effective process design, solubility and diffusivity of these gases in polymers are necessary.

Solubility and diffusivity of carbon dioxide in molten or thermally softened polymer systems have been investigated by several authors. Newitt and Weale [1] studied the solution and diffusion of hydrogen, nitrogen, carbon dioxide, and ethylene in polystyrene (PS) at temperatures up to 463 K and over the pressure range of 8–30 MPa. Durrill and Griskey [2,3] investigated a number of gas + polymer systems at temperature of 461.5 K Sato et al. [4,5] studied the solubility of carbon dioxide and nitrogen in PS, polypropylene, high-

* Corresponding author. Tel./fax: +81-824-247721.
E-mail address: masuoka@hiroshima-u.ac.jp (H. Masuoka).

0896-8446/01/$ - see front matter © 2001 Elsevier Science B.V. All rights reserved.
PII: S0896-8446(00)00092-9

density polyethylene at 313–473 K and up to 20 MPa. Takishima et al. [6] investigated the solubility and swelling caused by dissolution of CO_2 in poly(vinyl acetate) (PVAc) at 313 and 323 K and up to 9 MPa.

The pressure decay method is popular, because the apparatus is simple and construction cost is not expensive. However, it is difficult to apply at high temperatures especially for polymer melts, because pressure sensors, which have suitable accuracy and a small inner volume, are not available. Furthermore, in the pressure decay method, a large amount of the sample (about 5 g) is needed, which results in long measurement times in the molten state. The electrobalance method, which has many advantages such as a small amount of sample (short measurement times) and a high sensitivity, is also popular in the solubility measurement at near room temperature [7,8]. In the electrobalance method, several researchers used a microbalance placed in a pressure vessel. For this case, however, measurements were limited to temperatures below 125°C due to the microbalance operating conditions. New type gravimetric apparatus, in which temperatures of the balance and sample can be controlled independently, have been proposed for solubility measurements at high temperatures [9,10]. These type apparatus, however, can only be used for gases whose density is such that natural convection effects are tolerable. Study of polymer melts with dense carbon dioxide in its supercritical state ($\rho_c = 467$ kg/m^3) would be expected to present experimental difficulties. Kleinrahm and Wagner [11] developed a unique balance, so-called a magnetic suspension balance (MSB), for accurate measurements of fluid densities. The MSB has many advantages similar to microbalances except that the sample and the balance are isolated. This type instrument is expected to be suitable for measurement of the gas solubility and diffusivity in polymer at high temperatures and high-pressures. Loockemann et al. [12] and Schnitzler and Eggers [13,14] developed the apparatus using the MSB for the solubility and diffusivity of gas in solid polymer. In this work, a new apparatus based on the MSB was developed for measurements of solubility and diffusion coefficient of gas in molten polymer and solubilities and diffusion coefficients of carbon dioxide in PS and PVAc were measured to confirm the applicability. Furthermore, new data of diffusivity of carbon dioxide in PS were studied.

2. Experimental

2.1. Materials

Polystyrene (PS, $T_g = 381.4$ K, $\bar{M}w = 3.30 \times 10^5$, $\bar{M}n = 1.07 \times 10^5$) was supplied by Asahi Chemicals Inc. (Kawasaki). Poly(vinyl acetate) (PVAc, $T_g = 303$ K, $\bar{M}n = 1.67 \times 10^5$) was purchased from Aldrich. All the characteristics of the polymers were reported by the suppliers. Carbon dioxide ($> 99.5\%$ purity) was obtained from Iwatani Industrial Gases Corp. (Hiroshima). All chemicals were used as received.

2.2. Apparatus and methods

Solubility and diffusion coefficient of carbon dioxide in the polymers were measured by a MSB. Schematic diagram of the MSB [11] (Rubotherm Präzisionsmeβtechnik GmbH, Germany) is shown in Fig. 1. An electronically controlled magnetic suspension coupling is used to transmit the measured force from the sample enclosed in a pressure vessel to a microbalance. The suspension magnet, which is used for the transmitting the force, consists of a permanent magnet, a sensor core and a device for decoupling the measuring-load. An electromagnet, which is attached at the underfloor weighing hook of a balance, maintains the freely suspended state of the suspension magnet via an electronic control unit. Using this magnetic suspension coupling, the measuring force is transmitted contactlessly from the measuring chamber to the microbalance, which is located outside the chamber under ambient atmospheric conditions.

The distinct merit of the MSB is that the microbalance can be tared and calibrated during measurements. This zero-point correction and calibration of sensitivity of the microbalance is important for measuring the gas solubilities accurately, because long sorption times are gener-

ally needed. The MSB offers the possibility of lowering the suspension magnet in a controlled way to a second stationary position (Fig. 1b) a few millimeters below the measuring position. At this position, a sample basket is set down on a support by the suspension magnet's descent, and the sample is decoupled from the balance. This so-called 'zero-point position' allows a taring and calibration of the balance at any time, even while recording measurements.

In this work, the MSB was used for measurement of gas solubility and diffusivity in polymer. The MSB can be used at pressures up to 35 MPa and temperatures up to 523 K. Resolution and accuracy of the microbalance (Mettler AT261, Switzerland) are 0.01 mg and 0.002%, respectively. The amount of dissolved gas, W_g (g) was obtained following equation considering gas buoyancy:

$$W_g = W_F(P, T) - W_0(0, T) + \rho(P, T)[V_P(P, T)\{1 + S_w(P, T)\} + V_B] \quad (1)$$

where W_F and W_0 are readout of the balance at temperature, T and pressure, P and at zero pressure, respectively, ρ is the gas density (g/cm^3) and was obtained from the equation of state of Angus et al. [15]. The V_P and the V_B (cm^3) are volumes of the polymer sample and a sample basket (including a Petri dish, a sample holder, and the measuring load decoupling device, about 1 cm^3), respectively. V_B was determined by buoyancy measurements with an accuracy of $\pm 0.06\%$ using high-pressure CO_2 and N_2 at temperatures of 373.15, 423.15, and 473.15 K and pressures up to 20 MPa. The V_P was obtained from sample mass and specific volume, v_P (cm^3/g). The v_P was obtained from the Tait [16] parameters reported by Rodgers [17] for PVAc. The Tait parameters for PS were determined in this work using literature data of Zoller and Walsh [18] as follows:

$$v_P = v_0\left\{1 - 0.0894 \ln\left[1 + \frac{P}{B(T)}\right]\right\} \quad (2)$$

where

$$v_0 = 0.7884 \exp(5.790 \times 10^{-4} T) \quad (3)$$

$$B(T) = 887.2 \exp(-4.323 \times 10^{-3} T) \quad (4)$$

The degree of swelling of polymer, S_w, is caused by gas sorption. Since it is difficult to measure S_w

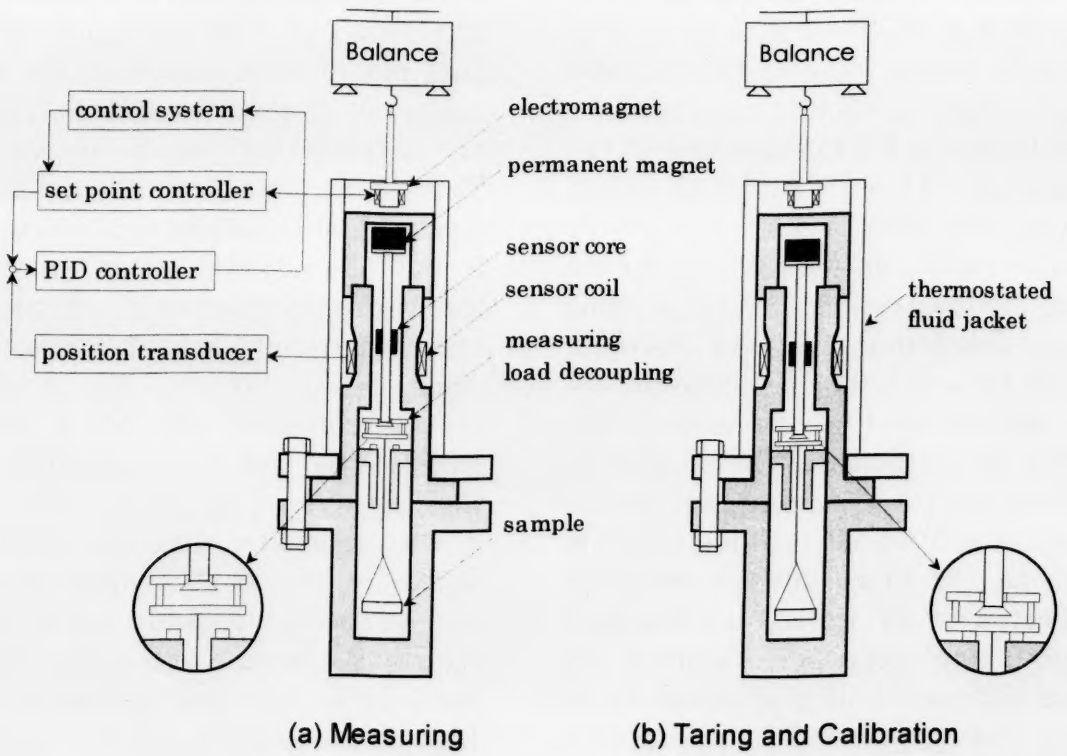

Fig. 1. MSB.

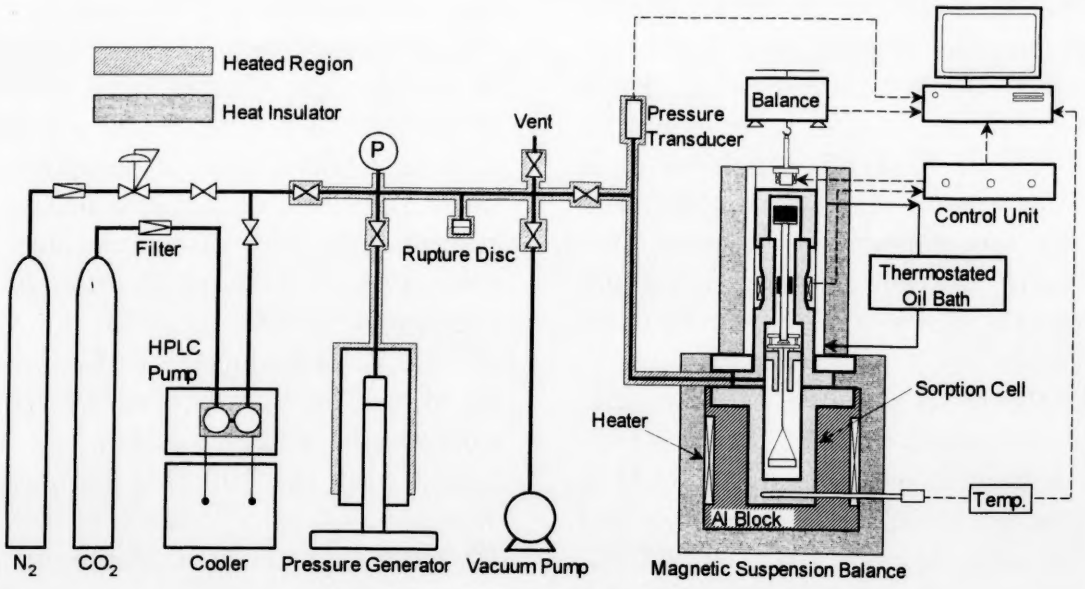

Fig. 2. Schematic diagram of solubility and diffusivity apparatus.

of molten polymer, we used predicted value of S_w by the Sanchez–Lacombe equation of state (S–L EOS) [19,20]. S_w is defined as follows

$$S_w = \frac{(1+S)v(P,T,S)}{v(P,T,0)} \tag{5}$$

where S (g-gas/g-polym) is the solubility and v (cm^3/g) is the specific volume of the polymer calculated by the S–L EOS. Since S_w is a function of solubility, it is necessary to solve Eqs. (1) and (5) simultaneously. Sato et al. [21] reported that the S_w predicted by the S–L EOS agreed with the experimental data for CO_2 + PVAc [6] to within an average relative deviation of 3.5%.

Mutual diffusion coefficients of gas in polymers were determined by measuring W_g versus time curves during gas dissolution. We used following four assumptions to determine the diffusion coefficient. First, we assumed Fick's second law. Second, the diffusion coefficient D was treated as being independent of gas concentration during each stepwise gas dissolution. Third, the diffusion was assumed to be one-dimensional in the polymer sample sheet with all diffusing substances entering through a single face plane. Fourth, the thickness of the polymer L was assumed to be constant during the sorption. The appropriate solution of the diffusion equation may be written [22] as

$$\frac{W_g(t) - W_g(0)}{W_g(\infty) - W_g(0)} = 1 - \frac{8}{\pi^2} \sum_{n=0}^{\infty} \frac{1}{(2n+1)^2} \exp\left[\frac{-(2n+1)^2\pi^2 Dt}{4L^2}\right] \tag{6}$$

where $W_g(t)$ is amount of gas in polymer at time t. Polymer sample was mounted in a Petri dish (ϕ 25 × 4 mm) to keep the sample form constant by melt molding the sample in the Petri dish. It is important to keep the sample form constant during sorption for the diffusivity measurements. This leads to reliable mathematical analysis of the results. The diffusion coefficient was determined from fitting sorption curves during about 0.5 MPa stepwise pressure changes to minimize the effect of concentration dependence on diffusion coefficient. L was obtained by dividing the sample volume corrected with S_w at average value between initial and final pressures by area of the Petri dish.

The schematic diagram of the apparatus is shown in Fig. 2. The apparatus consisted of a section for high-pressure gas supply, a section for mass measurement, and a data acquisition system. Pressure of gas was generated by means of a high-performance liquid chromatography (HPLC) pump (Jasco 880PU) for condensable gas and a pressure generator (High Pressure Equipment 87-

6-5) for uncondensable gas. The pressure was measured with Paroscientific pressure transducer (46KR, 41.4 MPa F.S., accuracy 0.01% F.S.). Tubes, the high-pressure generator, and the pressure transducer were thermostated to avoid condensation of the gas. The sorption cell, in which the sample basket was enclosed, was surrounded by an aluminum block. The aluminum block was mounted with a band heater and was surrounded with heat insulation. Temperature of the sorption cell was measured with an accuracy of ± 0.05 K using a Pt 100 Ω RTD probe inserted in the sorption cell wall as well as a thermometer (Hart Scientific 1502) and was controlled with a PID controller and the heater. The RTD probe as well as the thermometer was calibrated against an intelligent standard thermometer (Kaye Instruments, X0860, accuracy, ± 0.01 K).

A sample mounted in the apparatus was degassed about 10 h in vacuum at a given temperature, then carbon dioxide was introduced into the sorption cell to get the solubility or diffusivity. The readings of the balance, temperature, and pressure were acquired by a computer until equilibration was accomplished (it took about 10 min to 4 h depending on the diffusivity). Subsequent measurements were repeated to get isothermal solubility data. Pressure change of carbon dioxide was carried out stepwise. The pressure changes were about 2–4 MPa for the solubility measurements and about 0.5 MPa for simultaneous measurements of the diffusivity and solubility.

The mass of polymer used in the experiments was 0.1 to 0.2 g for PVAc and about 0.35 g for PS. Stability of the MSB depends on density fluctuation, because fluid buoyancy affects readout of the MSB. Fluctuations of the mass, temperature, and pressure were less than ± 0.13 mg, ± 0.025 K, and ± 0.003 MPa, respectively.

3. Results and discussion

3.1. Solubility

The solubility of CO_2 in PVAc is shown in Fig. 3 and Table 1. The solubilities increased with increasing pressure and decreased with an increase in temperature. These temperature and pressure dependence of the solubility were usually observed in condensable gas and polymer systems. The solubilities obtained in this work were compared with literature data. Our results were in good agreement with experimental data obtained by using an electrobalance method [23] to within an average relative deviation of 4.0% and to within 1.6% for measurements [24] made using a volumetric method [21]. The solubility of Takishima et al. [6] at 313.2 K agreed with our results to within 8.5% average relative deviation.

Error analysis was carried out for CO_2 + PVAc system. Uncertainty of solubility was estimated less than 4% at 313 K and at pressures between 0.5 and 7 MPa. However, this uncertainty does not include S_w error, because it is hard to estimate

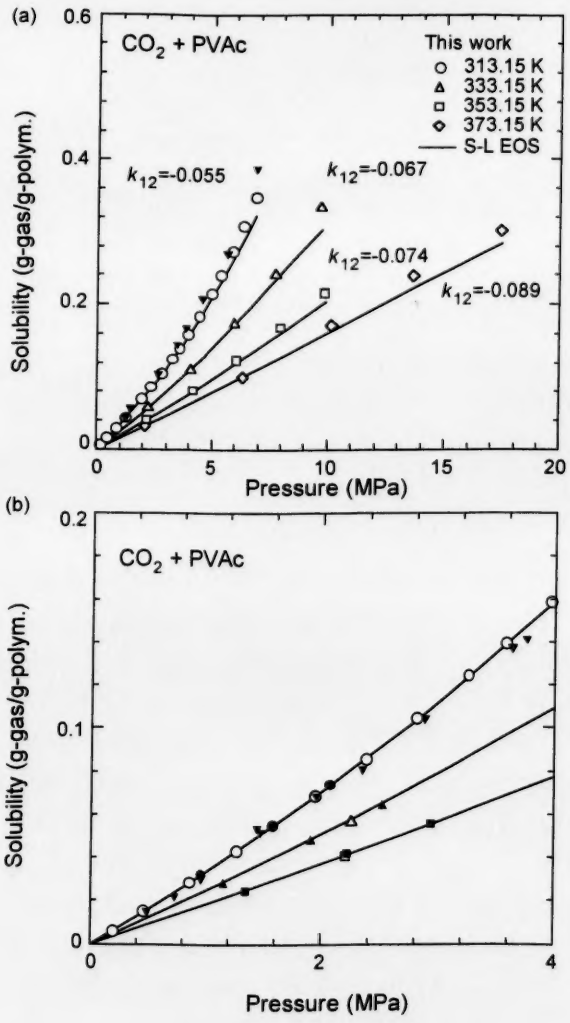

Fig. 3. Solubility of carbon dioxide in PVAc, (a) Takishima et al. (1990), ▼, 313.2 K; (b) Matsuura (1998), ▼, 313.2 K, Fukusako (1997), ●, 313.2 K, ▲, 333.2 K, ■, 353.2 K.

Table 1
Experimental solubility of carbon dioxide in PVAc

Temperature (K)	Pressure (MPa)	Solubility without S_w correction (g-gas/kg-polym)	Solubility with S_w correction (g-gas/kg-polym)	Swelling S_w (S–L EOS)
313.15	0.199	5.49	5.51	0.006
	0.459	14.55	14.65	0.016
	0.858	27.80	28.20	0.031
	1.271	41.84	42.75	0.047
	1.949	65.92	68.22	0.075
	2.375	81.63	85.22	0.094
	2.818	98.53	103.87	0.115
	3.260	115.99	123.54	0.137
	3.589	129.44	139.01	0.154
	3.979	145.78	158.19	0.176
	4.449	166.11	182.74	0.204
	4.978	189.95	212.59	0.238
	5.407	209.92	238.65	0.268
	5.916	234.51	272.35	0.306
	6.375	257.33	305.68	0.345
	6.876	283.40	346.92	0.393
333.15	2.263	53.93	56.08	0.064
	4.104	100.34	108.55	0.124
	6.010	150.18	171.37	0.197
	7.772	195.87	239.26	0.277
	9.694	241.96	332.41	0.387
353.15	2.211	38.47	39.92	0.047
	4.199	73.70	79.59	0.094
	6.110	107.63	121.79	0.144
	8.015	139.42	167.24	0.199
	9.876	166.01	214.30	0.256
373.15	2.157	29.46	30.51	0.037
	6.389	86.55	97.89	0.120
	10.194	134.41	170.00	0.209
	13.688	162.58	237.68	0.293
	17.449	167.00	299.25	0.369

the uncertainty of swelling, S_w, predicted by S–L EOS. Hence, we assumed that S_w had a relative uncertainty of 5%. Uncertainty of the solubility including the S_w error was estimated to be 6.0% at 7 MPa and 313.15 K. At 17 MPa and 373.15 K, the uncertainties for neglecting and including swelling, S_w, error were estimated to be a maximum of 7 and 20%, respectively. The S_w value affects solubility determination considerably.

The solubility of CO_2 in PS is shown in Fig. 4 and Table 2. Although PS was in its glassy state below its glass transition temperature of 381.4 K at atmospheric pressure, dual mode sorption behavior [7] was not observed at 373.15 K and over 2.068 MPa. In this experimental temperature and pressure range, PS was in its rubbery state, because the glass transition concentration of CO_2 at 373.15 K estimated with Chow's method [25] was 4.84 g-gas/kg-polym. In the Fig. 4, data of Sato et al. [4] obtained by using a pressure decay method at 373.2 K is also shown and agrees well with those of this work.

The swelling, S_w, predicted by the S–L EOS are given in Tables 1 and 2. The S_w showed a linear dependence on solubility for both the systems. High solubilites result in large degrees of swelling in the PVAc system. Although the swelling is not so high in the PS system, the relative S_w correction of the PS system was comparable with the PVAc system at the same temperature and pressure.

Fig. 5 shows the temperature dependence Henry's constant, K_P (kg·MPa/cm^3 (STP)) for CO_2 in PS and PVAc obtained in this work along with literature data. The reciprocal Henry's constants, $1/K_P$ in PS of this work agreed with previous data. Data for PVAc of Takishima et al. [6] were 4.6% higher than those of this work. Since literature data of Matsuura [23] and Fukusako [24] were excellently agreed (1.3 and 1.8% average relative deviations) with those of this work, we did not show them in the figure. We formulated a new correlation equation for the Henry's constants by using data of Sato et al. [4] and this work for PS and using the data of this work for PVAc. In the formulation, a least-squares method was used to determine a linear relationship between $\ln(1/K_P)$ and $(T_c/T)^2$.

CO_2 + PS system.

$$\ln\frac{1}{K_P} = 6.400 + 2.537\left(\frac{T_c}{T}\right)^2 \tag{7}$$

CO_2 + PVAc system.

$$\ln\frac{1}{K_P} = 6.914 + 2.924\left(\frac{T_c}{T}\right)^2 \tag{8}$$

These equations could represent the experimental Henry's constants to within average relative deviations of 2.5% for PS and 1.0% for PVAc.

Experimental solubility data were correlated with the Sanchez and Lacombe equation of state (S–L EOS) [19,20]:

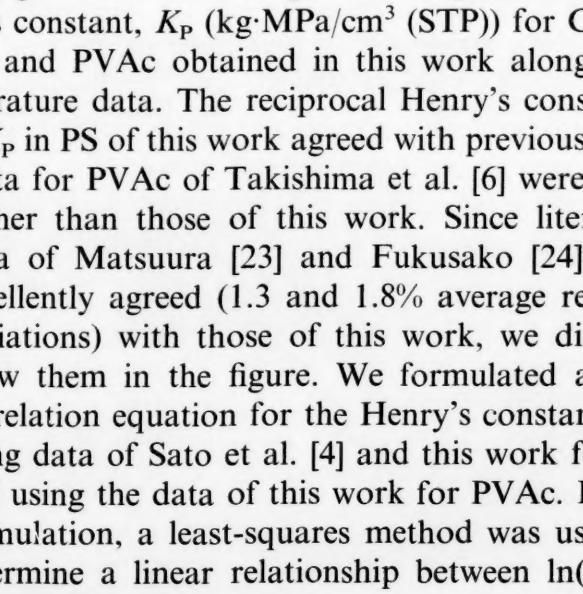

Fig. 4. Solubility of carbon dioxide in PS.

$$\tilde{P} = -\tilde{\rho}^2 - \tilde{T}\left[\ln(1-\tilde{\rho}) + \left(1-\frac{1}{r}\right)\tilde{\rho}\right] \tag{9}$$

$$\tilde{P} = \frac{P}{P^*}, \quad \tilde{\rho} = \frac{\rho}{\rho^*}, \quad \tilde{T} = \frac{T}{T^*}, \quad r = \frac{MP^*}{RT^*\rho^*} \tag{10}$$

where characteristic parameters, P^*, ρ^*, and T^* of the S–L EOS for mixture were evaluated with the following mixing rules.

$$P^* = \sum_i\sum_j \phi_i\phi_j P^*_{ij} \tag{11}$$

$$P^*_{ij} = (1-k_{ij})(P^*_i P^*_j)^{0.5} \tag{12}$$

$$T^* = P^*\sum_i \frac{\phi^0_i T^*_i}{P^*_i} \tag{13}$$

$$\frac{1}{r} = \sum_i \frac{\phi^0_i}{r^0_i} \tag{14}$$

$$\phi^0_i = \frac{(\phi_i P^*_i/T^*_i)}{\sum_j(\phi_j P^*_j/T^*_j)} \tag{15}$$

$$\phi_i = \frac{(w_i/\rho^*_i)}{\sum_j(w_j/\rho^*_j)} \tag{16}$$

In Eqs. (11)–(16), T^*_i, P^*_i, ρ^*_i, and r^0_i refer to the characteristic parameters of component i in the pure state and k_{ij} is a binary interaction parameter determined by fitting the equation to the experimental data. The pure component parameters used are given in Table 3. In the calculation of the solubilities, it was assumed that the polymer was monodisperse and that it did not dissolve in the vapor phase.

The binary interaction parameter, k_{ij}, in Eq. (12) was determined so as to minimize the relative deviations between experimental and calculated solubilities at each temperature. Correlation results are shown as solid lines in Figs. 3 and 4. The Sanchez–Lacombe EOS could correlate solubilities to within an average relative deviation of 3.6% for PVAc and 1.6% for PS. The k_{12} varied almost linearly with temperature. In both the systems, the deviation in the correlation became larger at the higher solubilities. This deviation may be attributed to two reasons. First, S_w correction might be overestimated. Second, the S–L EOS and its mixing rules might be not suitable for these systems.

Table 2
Experimental solubility of carbon dioxide in PS

Temperature (K)	Pressure (MPa)	Solubility without S_w correction (g-gas/kg-polym)	Solubility with S_w correction (g-gas/kg-polym)	Swelling S_w (S–L EOS)
373.15	2.068	12.31	12.74	0.014
	2.627	15.42	16.13	0.018
	4.093	23.50	25.29	0.029
	4.629	26.38	28.71	0.032
	6.038	33.39	37.53	0.042
	6.502	35.54	40.40	0.045
	8.054	42.04	49.83	0.056
	8.585	44.27	53.29	0.060
	12.105	54.35	74.16	0.083
	12.631	55.33	77.21	0.087
	16.059	59.56	98.68	0.110
	20.067	58.47	121.84	0.136
423.15	2.159	8.72	9.04	0.011
	2.689	10.80	11.30	0.014
	4.073	15.93	17.09	0.022
	4.732	18.23	19.81	0.025
	6.049	22.69	25.32	0.032
	6.530	24.32	27.42	0.034
	8.071	28.98	33.80	0.042
	8.566	30.41	35.88	0.045
	12.046	38.52	49.63	0.062
	12.593	39.59	51.79	0.064
	16.143	44.29	64.46	0.080
473.15	2.167	6.88	7.14	0.010
	2.884	9.02	9.48	0.013
	4.232	12.91	13.90	0.020
	4.795	14.45	15.73	0.022
	6.108	17.99	20.09	0.028
	6.685	19.48	21.99	0.031
	8.027	22.75	26.41	0.037
	8.813	24.61	29.05	0.041
	12.165	31.13	39.60	0.055
	12.659	32.08	41.29	0.057
	16.040	36.71	51.36	0.071
	20.151	39.88	62.31	0.085

3.2. Diffusion coefficient

In Fig. 6, the relationship between the relative amount of dissolved CO_2 in PVAc and elapsed time at 313.15 K is shown as an example. The solid line in the figure denotes calculation results of Eq. (6). For this case, a diffusion coefficient of 1.09×10^{-10} m^2/s was obtained.

Mutual diffusion coefficients of CO_2 in PVAc at 313.15 K are shown in Fig. 7 and Table 4. The diffusion coefficient exhibited strong concentration dependence and increased with increasing solubility. Literature data of Sasaki et al. [27] obtained by using a pressure decay method also shown in the figure. Although the diffusion coefficients of this work agreed with the literature data in the lower concentration region, our measurements in the higher concentration region were an order of magnitude higher than those of Sasaki et al. [27].

Uncertainty of the diffusivity for CO_2 + PVAc system at 313.15 K was estimated to be less than 28%, which includes an assumption of 5% in the S_w uncertainty. It was found that uncertainty of

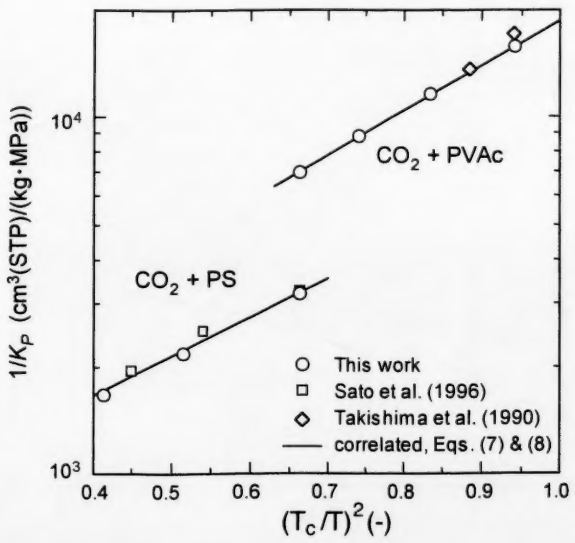

Fig. 5. Henry's constant for carbon dioxide in PS and PVAc.

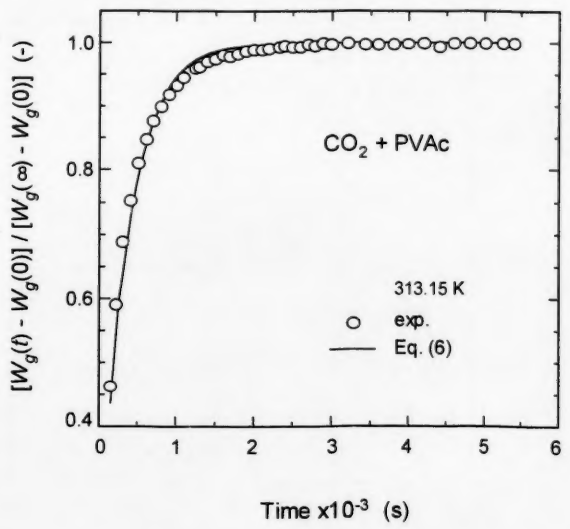

Fig. 6. Example of sorption curve for carbon dioxide and PVAc system pressure, 3.589–3.979 MPa; solubility, 139.0–158.2 g-gas/kg-polym; diffusion coefficient, 1.09×10^{-10} m²/s.

polymer thickness, L caused a large uncertainty in the diffusion coefficient.

Mutual diffusion coefficients of CO_2 in PS are shown in Fig. 8 and Table 5. The mutual diffusion coefficients of CO_2 in PS were correlated with the free volume model of Kulkarni and Stern [28]. The self-diffusion coefficient D_{self} is given by the expression [29]:

$$D_{self} = RTA_d \exp\left[\frac{-B_d}{v_f}\right] \quad (17)$$

where R is gas constant, T the absolute temperature, and A_d and B_d are characteristic parameters. The v_f is volume fraction of the free volume of the system comprised of gas and polymer was defined as follows [28]:

$$v_f(T, P, \phi_1) = v_{fs}(T_g, P_s, 0) + \alpha(T - T_g) - \beta(P - P_s) + \gamma\phi_1 \quad (18)$$

where v_{fs} is the free volume fraction at the glass transition temperature and atmospheric pressure, α the thermal expansion coefficient, β the compressibility γ the concentration coefficient of the free volume, T_g the glass transition temperature, P_s the standard pressure ($=0.1$ MPa), and ϕ_1 is the volume fraction of gas. The value for v_{fs} was fixed at 0.025 for amorphous polymers and α was fixed at 4.8×10^{-4} per K. These values were investigated by Williams et al. [30] in the temperature range of $T_g < T < T_g + 100$. The compressibility was determined from the following equation [28]:

$$\frac{\beta}{1 - v_f^*} = \beta' = -\frac{1}{V}\left(\frac{\partial V}{\partial P}\right)_T \quad (19)$$

where β' is the isothermal compressibility of the pure polymer obtained from PVT data [18]. The v_f^* in Eq. (19) is the free volume of polymer at temperature, T and pressure, P_s and was calculated from the following equation.

Table 3
Characteristic parameters for Sanchez–Lacombe EOS

Substance	P^* (MPa)	ρ^* (kg/m³)	T^* (K)	References
Carbon dioxide	720.3	1580	$208.9 + 0.459T - 7.56 \times 10^{-4}T^2$	[26]
PVAc	504.2	1282	592.0	[17]
PS	387.0	1108	739.9	[4]

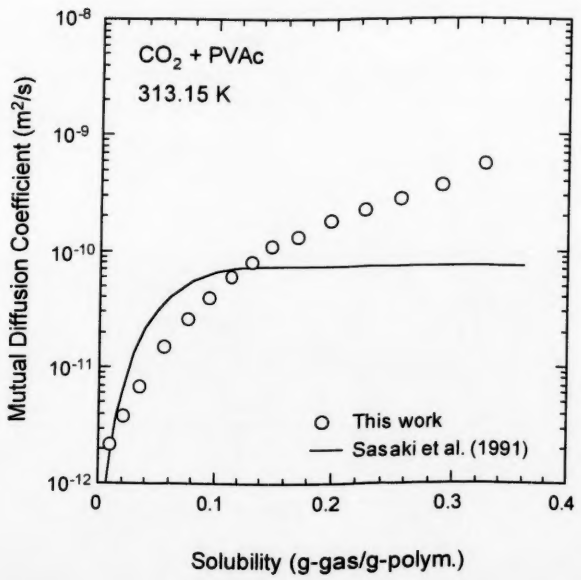

Fig. 7. Mutual diffusion coefficient of carbon dioxide in PVAc.

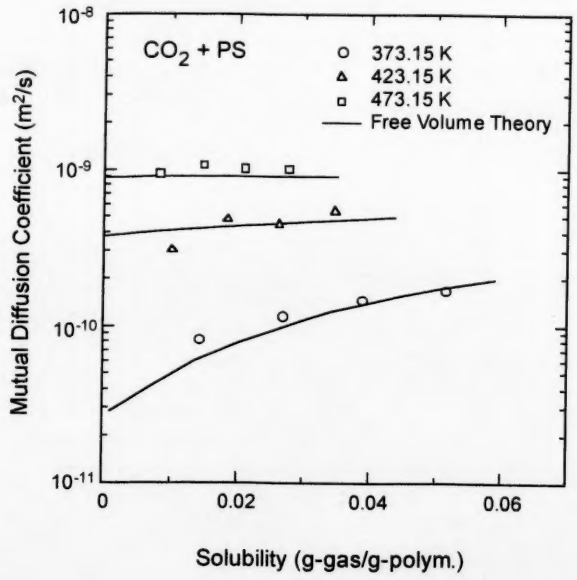

Fig. 8. Mutual diffusion coefficient of carbon dioxide in PS.

$$v_f^* = v_{fs} + \alpha(T - T_g) + \beta P_s = \frac{v_{fs} + \alpha(T - T_g) + \beta' P_s}{1 + \beta' P_s} \quad (20)$$

The relationship between self-diffusion coefficient D_{self} and mutual-diffusion coefficient D_{mtl}, was obtained from [31]:

$$D_{mtl} = \frac{D_{self} x_2}{RT}\left(\frac{\partial \mu_1}{\partial \ln x_1}\right)_{T,P} \quad (21)$$

where x_i is mole fraction of i, μ_1 was chemical potential of gas in polymer. $\bar{M}n$ was used for the calculations of x_i. The chemical potential gradient of the gas in Eq. (21) was obtained from numerical calculation using the S–L EOS. To develop a correlation for the mutual diffusion coefficients (Eq. (21)), the characteristic constants A_d and B_d, in Eq. (17) and γ in Eq. (18) were used as fitting parameters to represent the experimental diffusion coefficients. The fitting parameters determined were $A_d = 1.004 \times 10^{-12}$ m²·mol/(s·J), $B_d =$

Table 4
Experimental diffusion coefficient of carbon dioxide in PVAc at 313.15 K

Pressure range (MPa)	Average pressure (MPa)	Average solubility (g-gas/kg-polym.)	Diffusion coefficient of $CO_2 \times 10^{12}$ (m²/s)
0.199–0.459	0.329	10.08	2.15
0.459–0.858	0.659	21.43	3.76
0.858–1.271	1.065	35.48	6.81
1.271–1.949	1.610	55.49	14.7
1.949–2.375	2.162	76.72	25.9
2.375–2.818	2.597	94.55	39.4
2.818–3.260	3.039	113.7	60.9
3.260–3.589	3.425	131.3	81.3
3.589–3.979	3.784	148.6	109
3.979–4.449	4.214	170.5	131
4.449–4.978	4.714	197.7	182
4.978–5.407	5.193	225.6	223
5.407–5.916	5.662	255.5	279
5.916–6.375	6.146	289.0	366
6.375–6.876	6.626	326.3	554

Table 5
Experimental diffusion coefficient of carbon dioxide in PS

Temperature (K)	Pressure range (MPa)	Average pressure (MPa)	Average solubility (g-gas/kg-polym)	Diffusion coefficient of $CO_2 \times 10^{10}$ (m^2/s)
373.15	2.068–2.627	2.348	14.44	0.81
	4.093–4.629	4.361	27.00	1.14
	6.038–6.502	6.270	38.97	1.46
	8.054–8.585	8.320	51.56	1.67
423.15	2.159–2.689	2.424	10.17	3.01
	4.073–4.732	4.403	18.45	4.72
	6.049–6.530	6.290	26.37	4.42
	8.071–8.566	8.319	34.84	5.33
473.15	2.167–2.884	2.526	8.31	9.24
	4.232–4.795	4.514	14.82	10.5
	6.108–6.685	6.397	21.04	10.0
	8.027–8.813	8.420	27.73	9.90

0.1017, $\gamma = 0.6895$. Correlation results of the mutual diffusion coefficients are shown by the solid lines in Fig. 8. The free volume theory could correlate the diffusion coefficients to within 11% average relative deviation.

4. Conclusions

Solubilities of diffusion coefficients of carbon dioxide in PS and PVAc were measured with a new apparatus using a MSB technique. Experimental solubility data in PVAc and PS were correlated with the Sanchez and Lacombe equation of state to within an average relative deviation of 3.6 and 1.6%, respectively. Experimental diffusion coefficients in PS were correlated with the free volume model of Kulkarni and Stern to within an average relative deviation of 11%.

Acknowledgements

The authors wish to acknowledge Asahi Chemical Industry Co. Ltd. (Kawasaki) for supplying the PS, A. Sorakubo for his assistance with experiments, and Bel Japan Inc. (Osaka) for maintenance of the MSB. This work was supported through a grant-in-aid for Scientific Research (Project No. 09305053) by the Ministry of Education, Science, Sports and Culture, Japan and through the 'Research for the Future' program (Project No. JSPS-PFTF 96P00401) by the Japan Society for the Promotion of Science.

References

[1] D.M. Newitt, K.E. Weale, Solution and diffusion of gases in polystyrene at high pressures, J. Chem. Soc. (London), (1948) 1541.
[2] P.L. Durrill, R.G. Griskey, Diffusion and solution of gases in thermally softened or molten polymers; part I. Development of technique and determination of data, Am. Inst. Chem. Eng. J. 12 (1966) 1147.
[3] P.L. Durrill, R.G. Griskey, Diffusion and solution of gases in thermally softened or molten polymers; part II. Relation of diffusivities and solubilities with temperature pressure and structural characteristics, Am. Inst. Chem. Eng. J. 15 (1969) 106.
[4] Y. Sato, M. Yurugi, K. Fujiwara, S. Takishiam, H. Masuoka, Solubilities of carbon dioxide and nitrogen in polystyrene under high temperature and pressure, Fluid Phase Equilib. 125 (1996) 129.
[5] Y. Sato, K. Fujiwara, T. Takikawa, Sumarno, S. Takishima, H. Masuoka, Solubilities and diffusion coefficients of carbon dioxide and nitrogen in polypropylene, high-density polyethylene, and polystyrene under high pressures and temperatures, Fluid Phase Equilib. 162 (1999) 261.
[6] S. Takishima, K. Nakamura, M. Sasaki, H. Masuoka, Dilation and solubility in carbon dioxide + poly(vinyl acetate) system at high pressure, Sekiyu Gakkaishi (J. Jpn. Petrol. Inst.) 33 (1990) 332.
[7] Y. Kamiya, K. Mizoguchi, Y. Naito, T. Hirose, Gas sorption in poly(vinyl benzoate), J. Polym. Sci.: Part B: Polym. Phys. 24 (1986) 535.

[8] B. Wong, Z. Zhang, Y.P. Handa, High-precision gravimetric technique for determining the solubility and diffusivity of gases in polymers, J. Polym. Sci.: Part B: Polym. Phys. 36 (1998) 2025.
[9] Y. Kamiya, K. Mizoguchi, K. Terada, Y. Fujiwara, J.-S. Wang, CO_2 sorption and dilation of poly(methyl methacrylate), Macromolecules 31 (1998) 472.
[10] J.G. Lee, R.W. Flumerfelt, Nitrogen solubilities in low-density polyethylene at high temperatures and high pressures, J. Appl. Polym. Sci. 58 (1995) 2213.
[11] R. Kleinrahm, W. Wagner, Measurement and correlation of the equilibrium liquid and vapour densities and the vapour pressure along the coexistence curve of methane, J. Chem. Thermodyn. 18 (1986) 739.
[12] C.A. Lockemann, T. Riede, P. Magin, An experimental method to determine the sorption and swelling behavior of solids at high pressures, in: P.R. von Rohr, C. Trepp (Eds.), High Pressure Chemical Engineering, Elsevier, Amsterdam, 1996, p. 547.
[13] J. von Schnitzler, R. Eggers, Mass transfer phenomena in polymers during treatment in a supercritical CO_2-atmosphere, in: M. Perrut, P. Subra (Eds.), Preceedings of the Fifth Meeting on Supercritical Fluids, Nice, 1998, p. 93.
[14] J. von Schnitzler, R. Eggers, Mass transfer in polymers in a supercritical CO_2-atmosphere, J. Supercrit. Fluids 16 (1999) 81.
[15] S. Angus, B. Armstrong, K.M. de Reuck, International Thermodynamic Tables of Fluid State-3 Carbon Dioxide, IUPAC Project Center, Pergamon Press, London, 1976.
[16] V.S. Nanda, R. Simha, Equation of state of polymer liquids and glasses at elevated pressures, J. Chem. Phys. 41 (1964) 3870.
[17] P.A. Rodgers, Pressure–volume–temperature relationships for polymeric liquids; a review of equations of state and their characteristic parameters for 56 polymers, J. Appl. Polym. Sci. 48 (1993) 1061.
[18] P. Zoller, D. Walsh, Standard Pressure–Volume–Temperature Data for Polymers, Technomic Publishing, Basel, Switzerland, 1995.
[19] I.C. Sanchez, R.H. Lacombe, An elementary molecular theory of classical fluids. Pure fluids, J. Phys. Chem. 80 (1976) 2352.
[20] I.C. Sanchez, R.H. Lacombe, Statistical thermodynamics of polymer solutions, Macromolecules 11 (1978) 1145.
[21] Y. Sato, T. Iketani, S. Takishima, H. Masuoka, Solubility of hydrofluorocarbon (HFC-134a, HFC-152a) and hydrochlorofluorocarbon (HCFC-142b) blowing agents in polystyrene, Polym. Eng. Sci. 40 (2000) 1369.
[22] J. Crank, The Mathematics of Diffusion, second ed., Oxford University Press, Oxford, 1975, p. 238.
[23] K. Matsuura, Solubility and diffusivity of ethylene in LLDPE (in Japanese), M.S. thesis of Engineering, Hiroshima University, Japan, 1998.
[24] T. Fukusako, Solubility of condensable gases in polymers (in Japanese), M.S. thesis of Engineering, Hiroshima University, Japan, 1997.
[25] T.S. Chow, Molecular interpretation of the glass transition temperature of polymer–diluent systems, Macromolecules 13 (1980) 362.
[26] N.-H. Wang, K. Hattori, S. Takishima, H. Masuoka, Measurement and prediction of vapor–liquid equilibrium ratios for solutes at infinite dilution in CO_2 + polyvinyl acetate system at high pressure (in Japanese), Kagaku Kogaku Ronbunshu 17 (1991) 1138.
[27] M. Sasaki, S. Takishima, H. Masuoka, Modeling for extraction of benzene from poly(vinyl acetate) by supercritical carbon dioxide (in Japanese), Kagaku Kogaku Ronbunshu 16 (1990) 1029.
[28] S.S. Kulkarni, S.A. Stern, The diffusion of CO_2, CH_4, C_2H_4, and C_3H_8 in polyethylene at elevated pressures, J. Polym. Sci. Polym. Phys. Ed. 21 (1983) 441.
[29] H. Fujita, Diffusion in polymer–diluent systems, Fortschr. Hochpolym. Forsch. 3 (1961) 1.
[30] M.L. Williams, R.F. Landel, J.D. Ferry, The temperature dependence of relaxation mechanisms in amorphous polymers and other glass-forming liquids, J. Am. Chem. Soc. 77 (1955) 3701.
[31] J.S. Vrentas, J.L. Duda, Diffusion in polymer–solvent systems. II. A predictive theory for the dependence of diffusion coefficients on temperature, concentration, and molecular weight, J. Polym. Sci.: Polym. Phys. Ed. 15 (1977) 417.

ELSEVIER

Journal of Supercritical Fluids 19 (2001) 199–207

THE JOURNAL OF Supercritical Fluids

www.elsevier.com/locate/supflu

Attempt to explain the changes in solvation of polystyrene in supercritical CO_2/ethanol mixtures using infrared and Raman spectroscopy

P. Lalanne [a,b], S. Rey [b], F. Cansell [b], T. Tassaing [a], Marcel Besnard [a,*]

[a] *Laboratoire de Physico-Chimie Moléculaire, CNRS (UMR 5803), Université de Bordeaux I, 351 Cours de la Libération, 33405 Talence, Cedex, France*

[b] *Institut de Chimie et de la Matière Condensée de Bordeaux, CNRS (UPR 1048), 87, A. Schweitzer, 33608 Pessac, Cedex, France*

Received 11 March 2000; received in revised form 24 July 2000; accepted 11 September 2000

Abstract

The polystyrene//CO_2/ethanol system has been investigated in the supercritical domain using infrared absorption (FTIR) and Raman scattering spectroscopies. The pressure and temperature were fixed in the range 20–35 MPa at 423 K for CO_2/ethanol mixtures with proportion in weight from (70/30) to (58/42). These conditions are those used in our previous study concerning the fractionation of this macromolecule. A surprising finding reported before was that the CO_2/ethanol mixture made of two non-solvents of PS at ambient conditions is able to dissolve PS chains under high temperature and pressure. In the present article, this question will be addressed at a microscopic level from a discussion of the intermolecular interactions between the polymer and the medium and between the CO_2 and ethanol components provided by the analysis of the spectra. © 2001 Elsevier Science B.V. All rights reserved.

Keywords: Polystyrene; CO_2/ethanol mixtures; Raman spectroscopy

1. Introduction

The fractionation and the purification of polymers using supercritical fluids (SCF) is a well established approach in material science processing [1–4]. In this context, we have recently applied this technique to fractionate two chemically different polymers, namely poly(ethylene oxide) (PEO) and polystyrene (PS), with a supercritical mixture made of carbon dioxide (CO_2) and ethanol [5,6]. An interesting result came out from the study of PS. Indeed, both CO_2 and ethanol are non-solvents of this macromolecule at ambient conditions ($T = 298$ K; $P = 0.1$ MPa). However, although at high pressure and temperature CO_2 remains a non-solvent, the addition of amount of ethanol allows to dissolve PS chains. More precisely, we have shown that, at 35 MPa and 423 K,

* Corresponding author. Tel.: +33-55-6848402; fax: +33-55-6846357.

E-mail address: marcel@loriot.lsmc.u-bordeaux.fr (M. Besnard).

0896-8446/01/$ - see front matter © 2001 Elsevier Science B.V. All rights reserved.

PII: S0896-8446(00)00095-4

a binary mixture CO_2/ethanol with proportions in weight ranging from (70/30) to (58/42) is able to solvate chains having molar masses, which are, respectively, 3800 and 8000 g mol^{-1}. The results obtained so far in this study have clearly provided an insight on the solvation process at the macroscopic level. However, this study has also raised an issue concerning the nature of the interactions involved in the complex PS//CO_2/ethanol system in order to have a better understanding of the solvation process on a microscopic scale.

It is noteworthy that studies in this research area are scarce. For instance, in vibrational spectroscopy, only few works based upon infrared absorption (FTIR) have been undertaken to study the solvent CO_2/alcohol (generally, the percent in weight of alcohol does not exceed 5%) under supercritical conditions. The aim was to measure the degree of intermolecular hydrogen bonding between methyl alcohol-d in supercritical CO_2. In this fluid, the equilibrium between the free monomer and hydrogen bonded oligomers (mostly tetramers) has been assessed under pressure and temperature conditions ranging from 30 to 40 MPa and from 313 to 353 K. In addition, a weak complex between CO_2 and methanol-d has been put in evidence [7]. Another FTIR study has reinforced this point of view concerning the existence of an interaction between CO_2 and methanol [8].

The goal of this article is to perform a study of the PS//CO_2/ethanol system using Raman and infrared spectroscopies. The first section will be devoted to the study of the pure components (CO_2, ethanol) and to the presentation of the results concerning the characterisation of the CO_2/ethanol mixtures. The experimental conditions have been fixed to those used in our previous fractionation experiments, namely at 423 K, in the pressure range 20–35 MPa and with (58/42) and (70/30) CO_2/ethanol weight proportions. In the second section, we will present a study of PS in the binary mixture, under the same experimental conditions. In a preliminary work, we have investigated solutions of PS in a series of solvents (tetrahydrofuran, cyclohexane, carbon tetrachloride...) at ambient temperature and pressure, in order to identify the vibrations of PS, which are the more sensitive probes of the solvation. Finally, we will discuss in the last section the solvation process on the ground of the interactions existing between the polymer chains and its environment and those between ethanol and CO_2.

2. Experimental details

2.1. Materials

CO_2 is provided by Air Liquide. Ethanol is a Prolabo product (99.9% purity) and other organic solvents originates from Aldrich (purity, > 99%). Critical temperatures and pressures of CO_2/ethanol mixtures have been determined by Kiran and co-workers [9].

The PS sample comes from Polymer Expert. It is characterised by a broad molar mass distribution, $\bar{M}_n = 5000$ g mol^{-1}; $\bar{M}_w = 8800$ g mol^{-1}; $I = 1.7$ (where $\bar{M}_n$ is the number average molar mass; $\bar{M}_w$ the average molar mass in weight; and I the molar mass distribution).

2.1.1. Mid-infrared spectroscopy

The measurements were performed on a Biorad interferometer (type FTS-60A) equipped with a globar source, a KBr beam splitter and a DTGS detector. Single beam spectra recorded in the spectral range 400–6000 cm^{-1} with a 2 cm^{-1} resolution were obtained by the Fourier transformation of 100 accumulated interferograms.

We have used a special inconel cell, which has four cylindrical sapphire windows, two for the infrared absorption measurements with a pathlength of 12 mm (which can be varied from 3 to 25 mm) and the others for direct observation of the solution using a video camera to insure that there is no demixing in the sample. The optical cell has been shown in detail in [10]. In order to be sure that the solution was at the equilibrium, mixing was performed with a stirrer put in the cell and the acquisition of the spectra was performed 10 min after a pressure change. The sealing was obtained using the unsupported area principle. All windows were positioned on the flat surface of the inconel plug with a 100-μm gold foil placed between the window and the plug in order to com-

pensate for imperfections at the two surfaces. Flat copper seals were used to insure sealing between the plug and the cell body. The heating of the cell was performed by four cartridge heaters, which were disposed in the body of the cell in which two thermocouples were placed, the first one was located close to one cartridge to achieve the temperature control and the second was kept close to the sample area in order to insure a good temperature regulation with an accuracy of about $\Delta T \pm 2$°C. The cell was connected via a long stainless steel capillary to an hydraulic pressurising system, which permits to control the pressure up to 1000 bar with an absolute uncertainty of ± 1 bar plus a R.E. of $\pm 0.3\%$. The lower part of the cell was loaded with an excess of polystyrene powder over that needed for saturation and the cell was evacuated under vacuum. Then, it was filled with ethanol at the requested weight percent concentration. The cell was heated up to 423 K and CO_2 was then added up to the desired pressure.

2.1.2. Raman spectroscopy

The Raman spectra were collected on a DILOR Omars 89 double monochromator spectrograph equipped with a charged coupled device (CCD) detector. The source was a Spectra Physics argon ion laser operating at a wavelength of 514.5 nm with a power of 600 mW. The polarised $I_{vv}(\bar{\nu})$ spectra were recorded in the spectral range 3400–3800 cm^{-1} with a resolution of 2 cm^{-1} using the standard 90° scattering geometry. The Raman cell used here was made of titanium and had the same geometry and sealing principle as the infrared cell. However, in this case, the entrance and exit windows were made of fused silica in order to perform proper spectroscopic polarisation observation.

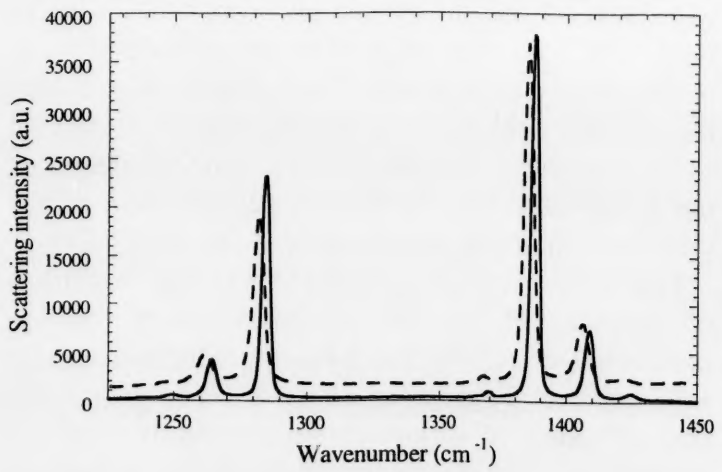

Fig. 1. Comparison of the Raman spectra of CO_2 in the CO_2/ethanol mixture ((58/42), – –) and in pure CO_2 (—) at 423 K and 20 MPa.

3. Results and discussion

3.1. Investigation of the supercritical CO_2/ethanol mixture

3.1.1. Raman scattering

We have performed Raman scattering measurements on the supercritical CO_2/ethanol mixture at various ethanol concentration (0, 30 and 42 wt.%) at 423 K for pressures ranging between 15 and 35 MPa. Two spectral domains are of particular interest here, namely, the spectral range between 800 and 1450 cm^{-1}, which is related to the Fermi resonance of the CO_2 internal modes (see below) and the 2700–3800 cm^{-1} region associated with the OH stretch of the ethanol molecule.

3.1.1.1. Spectral range 800–1450 cm^{-1}. We have reported in Fig. 1 the spectra of pure CO_2 compared with that of the supercritical (58/42) CO_2/ethanol mixture at 423 K and 20 MPa. The Raman spectra of the pure CO_2 displayed two narrow bands observed at about 1285 and 1388 cm^{-1}, which were due to a Fermi resonance between the harmonic $2\nu_2$ of the bending mode and the symmetric stretch ν_1 [11]. Additional very weak bands were also observed, which were assigned to a Fermi resonance between the modes $2\nu_2$ and ν_1 of the isotope derivatives C^{13}–O^{16} and C^{12}–O^{18} and between $\nu_1 + \nu_2$ and $3\nu_2$ [12]. These very weak bands will not be further considered in the following. The comparison of these spectra exhibited some noticeable differences. In the mixtures, we observed that the bands were shifted to lower wavenumbers compared with that of pure CO_2. Moreover, this shift increases with ethanol concentration ranging from 1 cm^{-1} for the (70/30) mixture up to 2.5 cm^{-1} for the (58/42) solution. This result might be associated with the

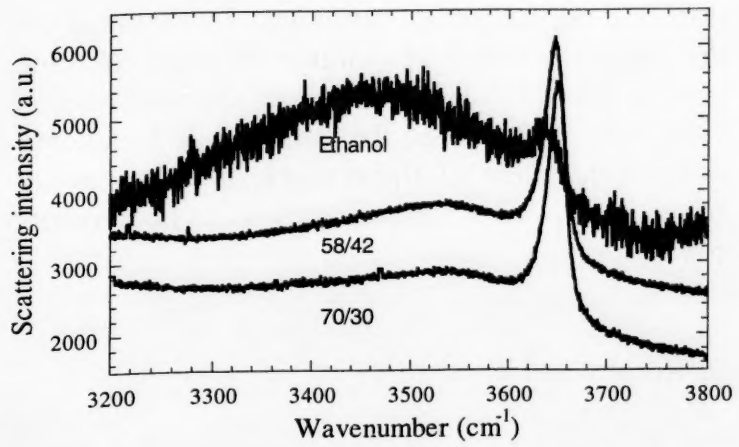

Fig. 2. Comparison of the Raman spectra of ethanol in the (70/30) and (58/42) CO_2/ethanol mixture with pure ethanol at 423 K and 35 MPa. For clarity, the two upper curves have been shifted upwards (arbitrary unit).

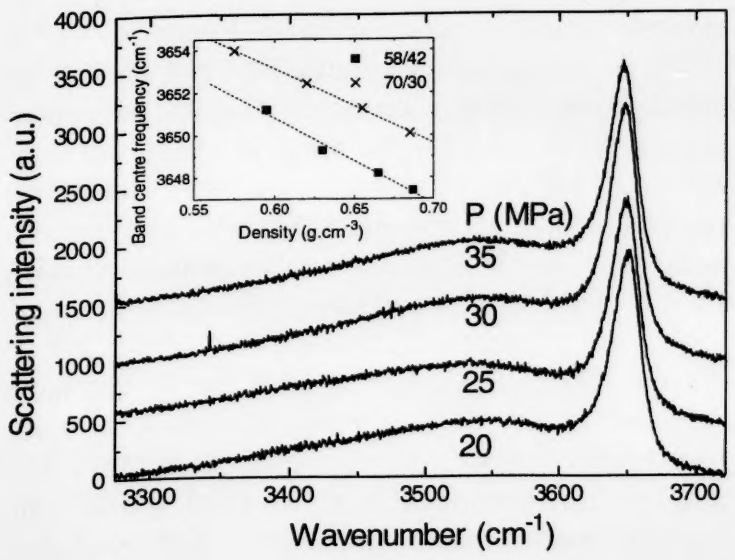

Fig. 3. Evolution of Raman spectra of ethanol as a function of pressure in the (58/42) CO_2/ethanol mixture at 423 K. For clarity, the three upper curves have been shifted upwards (arbitrary unit).

existence of an interaction between CO_2 and ethanol. Finally, we found that in a CO_2/ethanol mixture of fixed composition, when the pressure was increased from 15 to 35 MPa, the shifts of the CO_2 Fermi diads were less than 1 wavenumber. For neat CO_2 when the pressure was increased in the same range, the shift of the Fermi diads was also less than 1 wavenumber. For this reason, we can say that there is no noticeable effect of the pressure on the mixture [13].

3.1.1.2. Spectral range of the OH stretching mode of ethanol. Fig. 2 displays the Raman spectra of CO_2/ethanol mixtures at various ethanol concentration (0, 30 and 42 wt.%) at 35 MPa and 150°C). The spectrum associated with the OH stretching mode of pure ethanol at 423 K and 35 MPa was composed of a narrow band centred at about 3640 cm^{-1} assigned to monomeric ethanol together with a broad band centred at lower wavenumber (about 3450 cm^{-1}) corresponding to the ethanol molecules, which were hydrogen-bonded aggregated [14]. This spectrum was not affected by a pressure variation between 10 and 35 MPa [13]. Upon addition of CO_2 in the mixture, there was a strong modification of the shape of the spectra as it can be seen in Fig. 2 for both (70/30) and (58/42) mixtures. The intensity of the broad profile associated with alcohol oligomers decreased at the expenses of the narrow band associated with monomeric ethanol. Therefore, we can infer that the state of aggregation of the alcohol molecules is a function of the mixture composition and is displaced towards the formation of monomers as the CO_2 concentration increases in the medium [7,15]. Moreover, we observe also that the narrow band associated with the monomeric ethanol is red shifted at decreasing concentration of CO_2 in the mixture. Indeed, the peak maximum was, respectively, observed at 3637, 3647 and 3650 cm^{-1} on going from the pure ethanol to the (58/42) and (70/30) CO_2/ethanol mixtures. Clearly, the ν_{OH} vibration of the 'free' ethanol molecules probes mostly the attractive part of the intermolecular potential due to both CO_2 and ethanol surrounding molecules. It is very likely that in the electrostatic interaction, the dipolar field of surrounding ethanol molecule (let's emphasise that the 'free' ethanol molecule is not H-bonded) lead to greater perturbation of the vibration than the quadrupole field of the CO_2.

For a given composition (58/42), the variation of pressure in the 20–35 MPa range has no noticeable effect on the broad profile associated with ethanol aggregates (Fig. 3). Therefore, the concentration of oligomers in the mixture is not sensitive to pressure variations in this range. In contrast, the band associated with monomeric species was shifted towards lower frequencies when the pressure increased from 20 to 35 MPa

(Fig. 3). Attractive forces may be involved to explain this trend. Indeed, in a Van der Waals mean field approximation, it can be shown that the attractive forces lead to a red shift of the band centre, which is a linear function of the density (see insert in Fig. 3) [16]. Therefore, as before we may conclude that the monomer is in interaction with surrounding CO_2 and ethanol molecules and that the strength of the attractive interaction increases with the pressure [7,8,15].

3.1.2. Infrared absorption

The strong absorption of the CO_2/ethanol mixture precludes to obtain information about internal modes of CO_2 and ethanol in the spectral range between 500 and 4000 cm^{-1}. This drawback can be circumvented by looking at the combination modes of CO_2 and ethanol in the spectral range 4000–5000 cm^{-1} although they are weaker than the internal modes. We have used deuterated ethanol (CD_3CD_2OD), which will allow to observe in the PS/CO_2/ethanol mixture the internal modes of the benzene ring of polystyrene in the 3000–3100 cm^{-1} spectral range. We have optimised the pathlength of the cell (12 mm) to detect with a good accuracy the combination modes of CO_2 in the range 4700–5200 cm^{-1}.

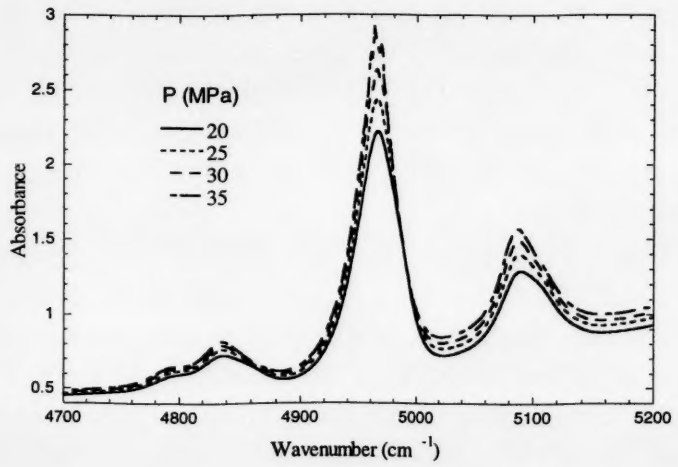

Fig. 4. Evolution of the combination bands of CO_2 as a function of pressure (20 —, 25 —, 30 — and 35 MPa —) in the (58/42) CO_2/ethanol mixture at 423 K.

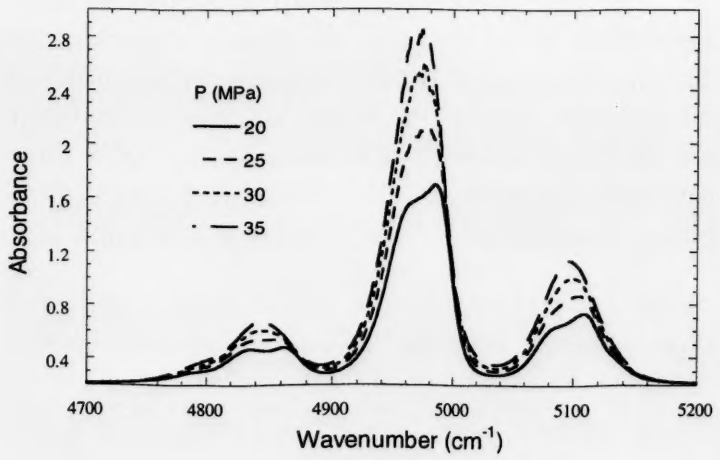

Fig. 5. Evolution of the combination bands of pure CO_2 as a function of pressure at 423K.

3.1.2.1. The CO_2/ethanol mixture. We have reported in Fig. 4 the spectra of the three combination bands of CO_2 in the (58/42) CO_2/ethanol mixture at 423 K and pressure ranging between 20 and 35 MPa. These bands observed at about 4840, 4960 and 5100 cm^{-1} are, respectively, assigned to the combination modes $4\nu_2 + \nu_3$, $\nu_1 + 2\nu_2 + \nu_3$ and $2\nu_1 + \nu_3$ [11]. Clearly, it appears that the pressure has no appreciable effect on the shape and the band centre of the three bands. The intensity enhancement observed when the pressure was raised was ascribed to the increase of the density of the medium. These measurements have also been performed on pure CO_2 under the same temperature and pressure conditions. The results reported in Fig. 5 show that all the three profiles are now sensitive to the pressure variation. Indeed, we notice that the band shapes are modified and that their intensity increases when the pressure is raised. In contrast, there is no noticeable variation of the band centre. The variation of the band shape can be qualitatively explained as follows. At low pressure, each band has the shape of the P–R vibrational–rotational transition envelop characteristic of a parallel transition of a linear molecule [11]. As the pressure is increased, the doublet structure collapses leading to a single profile centred at the mean frequency of the doublets. These modifications are well known in the spectroscopy of gaseous state [17]. Indeed, increasing the pressure, molecular collisions are more frequent and therefore, the rotation of CO_2 molecules are more perturbed [7,18,19]. The enhancement of the intensity is related to the increase of the medium density. Finally, in order to estimate the influence of the ethanol addition to

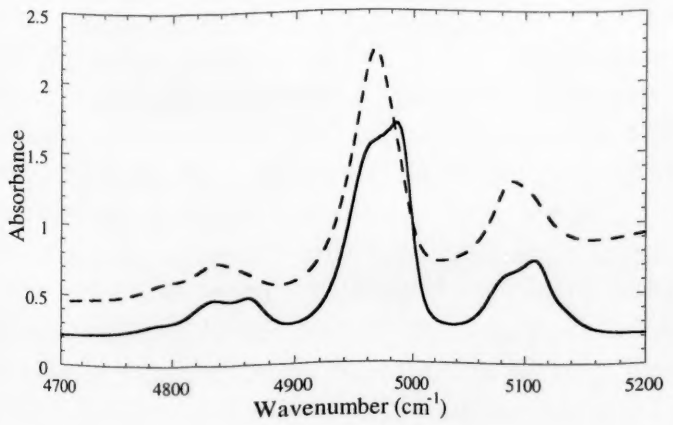

Fig. 6. Comparison of the combination bands of CO_2 in the (58/42) CO_2/ethanol mixture (– –) with that of pure CO_2 (—) at 423 K and 20 MPa.

pure CO_2, we have compared the spectrum of pure CO_2 with that of the (58/42) CO_2/ethanol mixture under the same experimental conditions (Fig. 6). Clearly, the three bands observed for the mixture are always shifted to lower frequencies compared with that of pure CO_2. This shift varies approximately from 5 cm^{-1} for the (70/30) CO_2/ethanol mixture up to 9 cm^{-1} for the (58/42) solution. The main result concerns the shape of the profiles. Indeed, comparing these two spectra, we remark that the 'doublet' structure observed for pure CO_2 on the three bands vanishes when ethanol is added in solution. All these observations allow to infer that an interaction exists between ethanol and CO_2, which leads to an hindrance of the CO_2 molecule rotation.

3.2. *Polystyrene/solvents*

3.2.1. *PS in solvents at ambient conditions*

In all the experiments performed in the following, we have used a polydisperse polystyrene sample with a broad molar mass distribution (see Section 2.1). In order to test if the molecular weight of the polystyrene sample has any influence on the infrared and Raman spectra, we have performed vibrational spectroscopic measurements on a monodisperse polystyrene sample dissolved in CS_2. No difference was observed between the spectra associated with the two samples. Such result is not puzzling. Indeed, vibrational spectroscopy is mainly sensitive to the local structure around a specific oscillator.

3.2.1.1. Raman scattering. We have performed Raman spectroscopic measurements on PS dissolved in a number of selected liquid solvents in view of their various solvation power, namely, in tetrahydrofuran (THF) (1 mol of monomer per l), in carbon disulfide (CS_2) (10^{-2} mol of monomer per l), and in chloroform (10^{-2} mol of monomer per l). In view of the low concentration of the solute, we have been able to detect only the symmetric breathing mode of the benzene ring of PS, centred at 1000 cm^{-1}. We observe that there is no dependence of the mode with the nature of the solvent.

3.2.1.2. IR spectroscopy. The same methodology has been used here. The solvents have been chosen in order to detect a maximum number of PS vibrational modes. We have analysed the following solutions, PS//THF (10^{-1} and 1 mol of monomer per l); PS//CS_2 (10^{-2} and 10^{-1} mol of monomer per l); PS//1,4-dioxan (10^{-2} and 10^{-1} mol of monomer per l); and PS//carbon tetrachloride (CCl_4) (10^{-1} mol of monomer per l). Among the observed modes, that centred at 699.9 cm^{-1} associated with the out of plane benzene ring deformation is slightly dependent on the nature of the solvent (Table 1). If we compare the band centre frequency with that reported for a PS film, we detect a shift of about 3 and 1.5 cm^{-1} to higher frequencies in the case of 1,4-dioxane and

Table 1
Solvent effect on the PS band (the out of plane benzene ring deformation), centred at 699.9 cm^{-1} (PS concentration, 10^{-1} mol of monomer per l)

CS_2 (cm^{-1})	Cyclohexane (cm^{-1})	CCl_4 (cm^{-1})	PS film (cm^{-1})	THF (cm^{-1})	1,4-Dioxane (cm^{-1})
698.5	698.5	699.6	699.9	701.2	702.7

Table 2
Solvent effect on the PS bands (CH stretch of the benzene ring) centred at 3026.4 and 3060 cm^{-1} (PS concentration, 10^{-1} mol of monomer per l)

PS film (cm^{-1})	CS_2 (cm^{-1})	1,4-Dioxane (cm^{-1})	THF (cm^{-1})	Cyclohexane (cm^{-1})	CCl_4 (cm^{-1})
3026.4	3026.4	3027.4	3028.4	3028.4	3029
3060	3060.6	3061.4	3062	3063.3	3065.3

THF, respectively, whereas a shift to lower frequencies of about 1.5 cm^{-1} is observed in CS_2 or cyclohexane. In CCl_4, the band position is the same than that reported for the PS film. The bands of PS centred at 1454, 1494 cm^{-1} and in the spectral range 2900–3000 cm^{-1} are hampered by strong absorption of the solvents. However, we have detected in the spectral range between 3000 and 3100 cm^{-1} two bands centred respectively at 3026.4 and 3060 cm^{-1}, which are assigned to CH stretching modes of the benzene ring of the PS molecule [20]. Taking the frequency reported for the PS film as a reference, we observe small frequency shifts to higher frequencies of about 1–3 cm^{-1} for PS dissolved in THF, cyclohexane, CCl_4 and 1,4-dioxane and we notice that CS_2 does not influence the band position (cf. Table 2). Finally, the polymer concentration does not affect the spectroscopic observations (band centre and width). Using these measurements of PS dissolved in liquid solvent at ambient conditions, we were able to calculate the molar absorption coefficient of the band centred at 3026.4 cm^{-1} from its integrated area; The value is 580 l mol^{-1} cm^{-2} and found to be independent on the nature of the solvent within experimental uncertainties.

3.2.2. PS in CO_2/deurated ethanol mixture

It's challenging to record the PS spectra in the CO_2/ethanol mixture. Indeed, in view of the low solubility of the PS in the solution, the spectrum is very weak and obscured by the absorption of CO_2/ethanol mixture. The only accessible spectral range is limited to the CH stretching of the PS benzene ring (3000–3100 cm^{-1}) and only if deuterated ethanol is used. Knowing the solubility of PS in the mixture as reported in previous studies [6], we have optimised the pathlength of the cell (12 mm) to detect with a good accuracy the CH stretching mode of the benzene ring of polystyrene at about 3030 cm^{-1}. We have measured the spectra of PS in the spectral domain 3000 and 3100 cm^{-1} at 423 K and 35 MPa for PS in the (58/42) and (70/30) mixtures (Fig. 7). It is found that the band centre of the CH stretch is at about 3030 cm^{-1} whatever the ethanol concentration in the medium is. This value is in the range of those reported for PS dissolved in liquid solvents at ambient conditions (Table 2). We note also that it is in the CO_2/ethanol mixture that the greater blue shift (compare with PS film) is observed. This finding is difficult to rationalise. Indeed, we know that the shift of the band centre frequencies observed in vibrational spectroscopy results from a subtle competition between attractive and repulsive forces. A glance to Table 2 shows that it's difficult to assign the spectral shifts observed to a specific molecular properties. Indeed, it's not obvious to correlate multipole moment, which gives some insight about attractive forces as well as the molecular shape (linear,

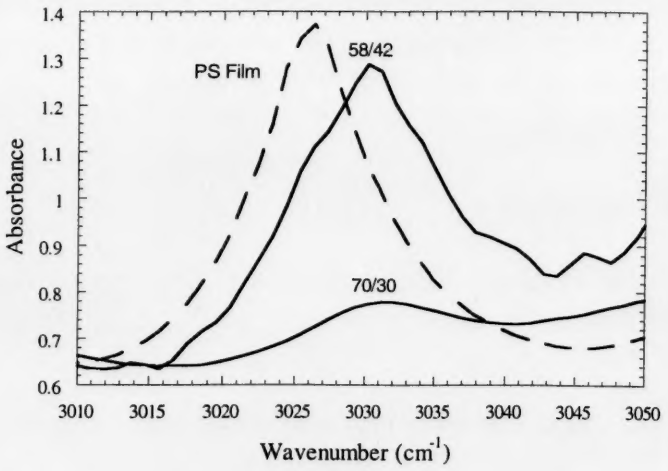

Fig. 7. Evolution of the CH stretching vibration mode of the benzene ring of PS in the (70/30) and (58/42) CO_2/ethanol mixture at 423 K and 35 MPa. The spectra of PS film is reported for comparison.

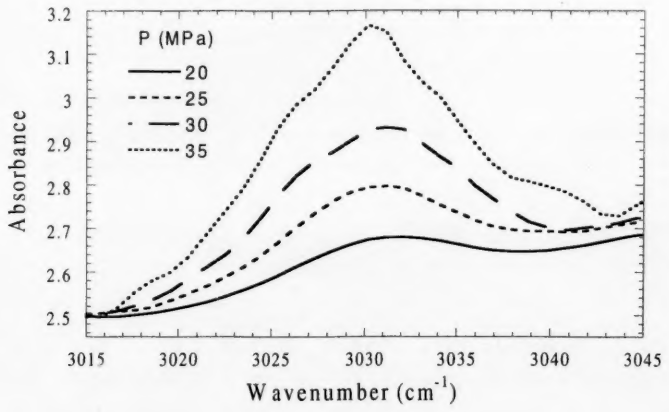

Fig. 8. Evolution of the CH stretching vibration mode of the benzene ring of PS in the(58/42) CO_2/ethanol mixture as a function of pressure at 423 K.

planar or spherical), which influences the repulsive interactions. In the absence of information on the structure and dynamics involved in these complicated mixtures, any attempt in these analyses seems to us extremely questionable. We have also performed some measurements at constant ethanol concentration as a function of pressure (see Fig. 8). From this set of data, it is possible to calculate the PS concentration in the (58/42) CO_2/ethanol mixture using the value of the molar extinction coefficient, which has been evaluated above. The results are reported in Table 3 and compared with those evaluated using UV spectroscopy [6]. An overall good agreement was observed for the two sets of data (within 15% of errors), which ensured the validity of the present and previous results and showed that the current experimental condition to obtain a good equilibrium of the solutions was achieved.

4. Conclusion

We summarise here the main findings coming out from the investigation of the PS//CO_2/ethanol mixture. The study of the CO_2/ethanol solvent reveals that ethanol is partitioned between monomers and H-bonded aggregates for which the relative concentration depends only upon the CO_2 concentration. Moreover, a weak interaction between the CO_2 and ethanol molecules has been put in evidence. These results corroborate experimental investigations on CO_2/methanol [7,8,21] and CO_2/ethanol [22]. The nature of the interaction might be of the Lewis acid–base type in which CO_2 carbon atom and the oxygen atom of the ethanol play, respectively, the role of the electron acceptor and donor. This conclusion is supported by ab initio theoretical work on the H_2O–CO_2 system [23,24] and from experimental studies on polymer impregnation with CO_2 [25]. Therefore, the PS//CO_2/ethanol system is composed of several species, namely, PS chains, monomeric ethanol molecules interacting with CO_2, aggregated ethanol molecules and finally CO_2 molecules. The ethanol is in large excess compared with the polymer. Estimations indicate that there is, respectively, about 1000 and 4000 ethanol molecules per styrene unit in the SC (70/30) and (58/42) mixtures. Therefore, even if ethanol molecules are partly aggregated, there is still a large amount of ethanol monomers, which can participate to the solvation process of PS chains. If we turn out to PS, we have shown that it may locally interact with the solvent medium as indicated by the perturbation of the CH benzene vibrations. It seems that the benzene ring is likely to be involved in the solvation process. It is noteworthy from our previous works on PS fractionation that ethanol is responsible of the PS solvation in the supercritical CO_2/ethanol mixture. Therefore, an interaction between benzene rings of the PS and the ethanol molecule may explain the solvation process.

Table 3
Concentrations of PS in the (58/42) CO_2/ethanol mixture at 423 K

P (MPa)	20	25	30	35
C_t^s (g monomer per g) IR	3.5×10^{-4}	7.1×10^{-4}	1.1×10^{-3}	1.9×10^{-3}
C_t^s (g monomer per g) UV	4.2×10^{-4}	6.1×10^{-4}	8×10^{-4} (28.8 MPa)	–

The present investigation has also revealed the stringent limitations encountered in experimental studies of polymer diluted in supercritical binary mixtures using vibrational spectroscopy. Indeed, the low solubility of the polymer, which leads to a low absorption or scattering and the fact that the strong contribution of the solvent leaves few accessible spectral range to the investigations of the solute, are very severe constraints.

Finally, much more theoretical works remain to be done in order to obtain information on the intermolecular interaction at a microscopic level from the spectroscopic shift and band shapes.

Acknowledgements

This work was performed under the auspices of the 'programme pluri-formation no. 971022' entitled 'Etude spectroscopique de fluides dans le domaine supercritique' from the University of Bordeaux I.

References

[1] P.M. Gallagher, M.P. Coffey, V.J. Krukonis, Supercritical fluid processing of polymers, Polym. Prep. 31 (1990) 668.
[2] I. Yilgör, J.E. McGrath, Novel supercritical fluid techniques for polymer fractionation and purification, Polym. Bull. 12 (1984) 491.
[3] J.J. Watkins, V.J. Krukonis, P.D. Condo, D. Pradhan, P. Ehrlich, Fractionation of high density polyethylene in propane by isothermal pressure profiling and isobaric temperature profiling, J. Supercrit. Fluids 4 (1991) 24.
[4] J.A. Pratt, M.A. McHugh, Supercritical-fluid fractionation of poly(ethylene-co-acrylic acid), J. Supercrit. Fluids 9 (1996) 61.
[5] S. Rey, F. Cansell, Universal supercritical binary mixture for polymer fractionation, Polym. J. 30 (1998) 863.
[6] S. Rey, F.J. Cansell, Supercrit. Fluids, submitted for publication.
[7] J.L. Fulton, G.G. Yee, R.D. Smith, Hydrogen bonding of methyl alcohol-d in supercritical carbon dioxide, J. Am. Chem. Soc. 113 (1991) 8327.
[8] J.T. Reilly, C.P. Bokis, M.D. Donohue, An experimental investigation of Lewis acid–base interactions of liquid carbon dioxide using Fourier transform infrared (FT-IR) spectroscopy, in: I.S.A.S.F (Ed.), Thermodynamics and Physical–Chemical Properties, 1994, pp. 209–222.
[9] H. Pöhler, E. Kiran, Volumetric properties of carbon dioxide + ethanol at high pressures, J. Chem. Eng. Data 42 (1997) 384.
[10] S. Rey, Ph.D. thesis, University Bordeaux I, 1999.
[11] G. Herzberg, Molecular spectra and molecular structure II. Infrared and Raman Spectra of Polyatomic Molecules, Lancaster Press, 1956, pp. 273–277.
[12] S. Monteron, Raman intensities of fermi diads. I. Overtones in resonance with nondegenerate fundamentals, J. Chem. Phys. 79 (1983) 4091.
[13] P. Lalanne, Ph.D. thesis, University Bordeaux I, in preparation.
[14] W.A.P. Luck, Infrared fundamental region, in: W.A.P. Luck (Ed.), Structure of Water and Aqueous Solutions, Hans Richarz Publikationservice, 1974, pp. 221–245.
[15] J.L. Fulton, G.G. Yee, R.D. Smith, Hydrogen bonding of simple alcohols in supercritical fluids, in: E. Kiran, J.F. Brennecke (Eds.), Supercritical Fluid Engineering Science, ACS Symposium Series, vol. 514, 1993, pp. 175–187.
[16] D. Ben-Amotz, M.R. Lee, S.Y. Cho, D.J. List, Solvent and pressure-induced perturbations of the vibrational potential surface of acetonitrile, J. Chem. Phys. 96 (1992) 8781.
[17] A.I. Burshtein, S.I. Temkin, Spectroscopy of Molecular Rotation in Gases and Liquids, Cambridge University Press, Cambridge, 1994.
[18] L.E. Bowman, B.J. Palmer, B.C. Garrett, J.L. Fulton, C.R. Yonker, D.M. Pfund, S.L. Wallen, Infrared and molecular dynamics simulation study of D_2O rotational relaxation in supercritical CO_2 and Xe, J. Phys. Chem. 100 (1996) 18327.
[19] M. Buback, J. Schweer, H. Tups, Near infrared absorption of pure carbon dioxide up to 3100 bar and 500 K, Z. Naturforsch 41a (1986) 505.
[20] D.I. Bower, W.F. Maddams, The Vibrational Spectroscopy of Polymers, Cambridge University Press, Cambridge, 1989, pp. 194–201.
[21] B. Hemmaplardh, A.D. King, Solubility of methanol in compressed nitrogen, argon, methane, ethylene, ethane, carbon dioxide, and nitrous oxide. Evidence for association of carbon dioxide with methanol in the gas phase, J. Phys. Chem. 76 (1972) 2170.
[22] S.K. Gupta, R.D. Lesslie, A.D. King, Solubility of alcohols in compressed gases. A comparison of vapor-phase interactions of alcohols and homomorphic compounds with various gases. I. Ethanol in compressed helium, hydrogen, argon, methane, ethylene, ethane, carbon dioxide, and nitrous oxide, J. Phys. Chem. 77 (1973) 2011.
[23] A.J. Cox, T.A. Ford, L. Glasser, Ab initio molecular orbital calculations of the infrared spectra of interacting water molecules. Part 4. Interaction energies and band intensities of the complexes of water with carbon dioxide and nitrous oxide, J. Mol. Struct. 312 (1994) 101.
[24] N.R. Zhang, D.D. Shillady, Ab initio equilibrium constants for H_2O–H_2O and H_2O–CO_2, J. Chem. Phys. 100 (1994) 5230.
[25] S.G. Kazarian, M.F. Vincent, F.V. Bright, C.L. Liotta, C.A. Eckert, Specific intermolecular interaction of carbon dioxide with polymers, J. Am. Chem. Soc. 118 (1996) 1729.

ELSEVIER

Journal of Supercritical Fluids 19 (2001) 209–215

THE JOURNAL OF Supercritical Fluids

www.elsevier.com/locate/supflu

Synthesis of barium titanate using supercritical CO_2 drying of gels

Zoran Novak, Zeljko Knez *, Irena Ban, Miha Drofenik

University of Maribor, Faculty of Chemistry and Chemical Engineering, Smetanova 17, SI-2000 Maribor, Slovenia

Received 13 March 2000; received in revised form 4 September 2000; accepted 27 September 2000

Abstract

$BaTiO_3$ powders from sol-gel derived gels were prepared using two different drying methods. In addition to the conventional drying of gels in air at 90°C the supercritical CO_2 drying method was also used. Results showed that the properties of $BaTiO_3$ powder produced by supercritical drying with CO_2 are better. The grain surface is less contaminated as a result of the supercritical drying and the microstructure development during sintering leads to a homogeneous fine-grained microstructure. © 2001 Elsevier Science B.V. All rights reserved.

Keywords: Barium titanate; Sol-gel synthesis; Supercritical CO_2; Ceramic powders

1. Introduction

An important area of investigation in the study of ceramic materials is related to ceramic powders with small grains, in particular the study of nano-sized powders, used during the preparation of electronic ceramics. Many different methods of synthesis for fine ceramic powders are well known, for example: co-precipitation, spray drying, spray freezing, hydrothermal synthesis and the sol-gel procedure [1–3]. Among these processes, the sol-gel procedure is particularly promising since it enables the control of the homogeneity and reactivity of the ceramic powders to a large extent. Sol-gel techniques are increasingly used for the production of high technology ceramics, due to superior electronic properties, mechanical stability and chemical purity. One of the important steps during powder synthesis, using the sol-gel procedure, is the drying of the gels. Many important powder properties, for example: the homogeneity, the size of the agglomerates and the extent of agglomeration are developed during this important step of powder synthesis. The drying of gels is certainly a key process when it comes to the final properties of the powder, this is particularly true when controlling the powder agglomeration. The essential electronic and mechanical properties, reflected in the microstructure, are determined to a large extent by the drying stage of the gels.

* Corresponding author. Tel.: +386-2-2294461; fax: +386-2-2516750.

E-mail address: zeljko.knez@uni-mb.si (Z. Knez).

0896-8446/01/$ - see front matter © 2001 Elsevier Science B.V. All rights reserved.
PII: S0896-8446(00)00090-5

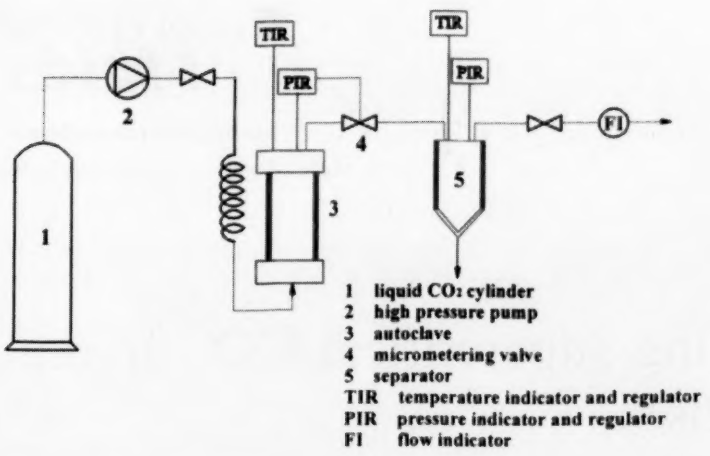

Fig. 1. Experimental apparatus for supercritical CO_2 drying.

Gels are usually dried for long times in air at elevated temperatures. In the course of our work we have prepared fine-grained powders by drying gels using supercritical CO_2 [4] and we have compared their properties with those of classically prepared powders.

2. Experimental

Different $BaTiO_3$ powders were prepared by two different drying methods for sol-gel derived $BaTiO_3$ gels. Besides the conventional drying of gels in air at 90°C (powder A) supercritical drying with CO_2 was also applied (powder B) to compare the properties of both $BaTiO_3$ powders.

2.1. Sol-gel synthesis

For the preparation of $BaTiO_3$ gels, titanium(IV) isopropoxide, $Ti[OCH(CH_3)_2]_4$, (ALFA, purity 99.99%) and barium ethoxide, $Ba(OCH_2CH_3)_2$, (ALFA, purity 99.99%, 10 wt.% solution in pure ethanol) were used in equimolar amounts (Ba:Ti = 1:1). The synthesis of Ba–Ti precursor alkoxide mixtures was performed in a glass reactor in a dry nitrogen atmosphere and stirred for 48 h at room temperature. After that, CO_2-free distilled water was injected into the precursor solutions in excess amounts (molar ratio $Ba:H_2O = 1:25$). The hydrolized solutions were aged for 30 days at room temperature.

2.2. Supercritical CO_2 drying

After the gelation was terminated, the gels were

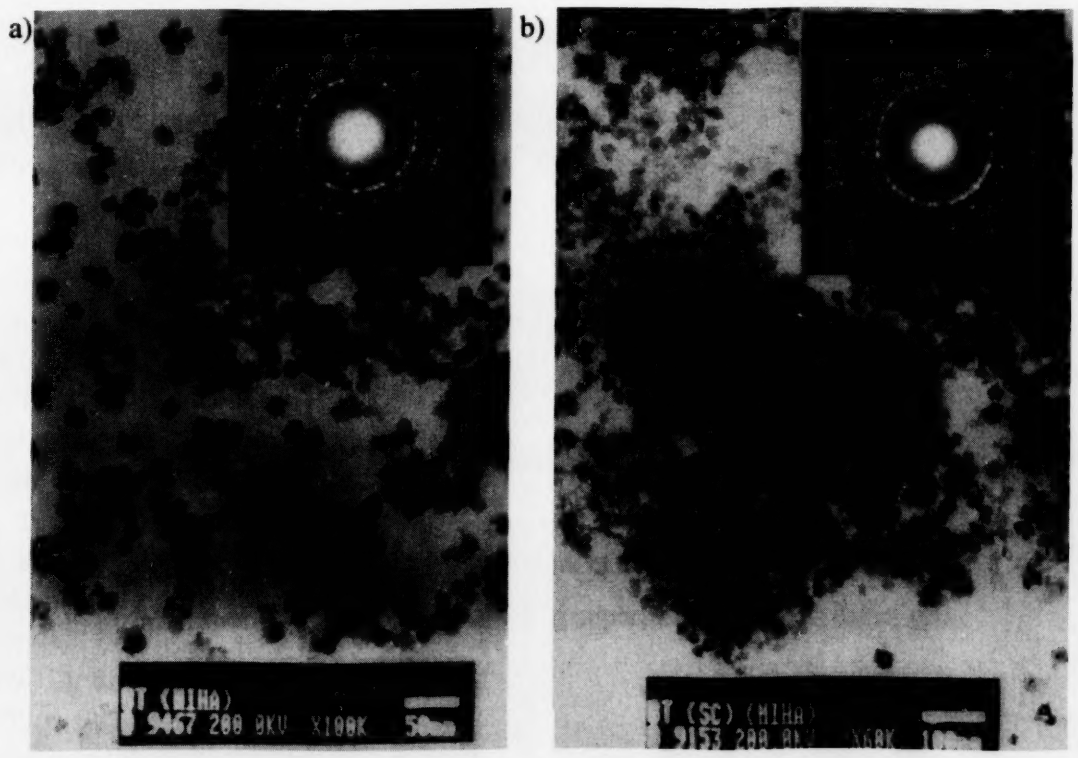

Fig. 2. TEM images of the $BaTiO_3$ powders: (a) prepared by drying of gels in air; (b) prepared by supercritical CO_2 drying.

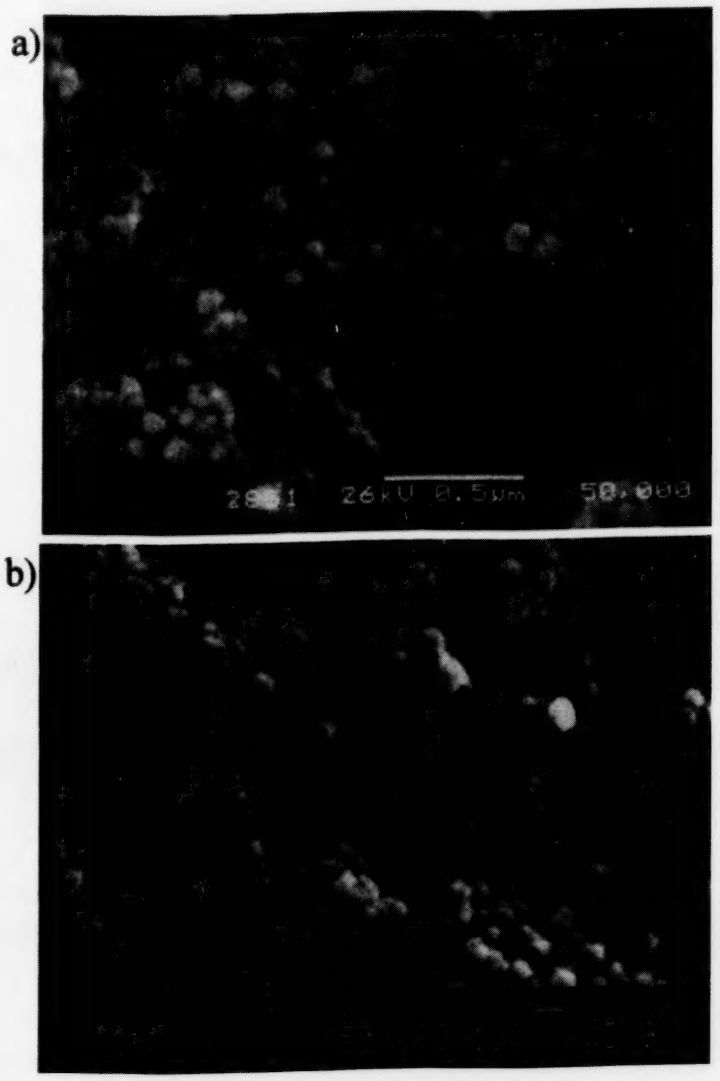

Fig. 3. SEM images of $BaTiO_3$ powders: (a) powder A prepared by drying in air; (b) powder B prepared by supercritical CO_2 drying.

dried in air at 90°C (powder A) and in supercritical CO_2 (powder B).

Aerogels, with their special properties, can only be produced when the solvent is removed in the absence of capillary forces in the gel pores, because even small capillary forces collapse the gel structure.

In supercritical carbon dioxide drying, alcohol is replaced by carbon dioxide at conditions above the critical conditions of CO_2 (T_C = 31.1°C, P_C = 7.36 MPa). All supercritical carbon dioxide drying experiments were performed at the temperature of 40°C and the pressure of 100 bar.

The extractor (Fig. 1) is completely filled with solvent (methanol) in order to minimize the evaporation of the solvent from the alcogel and to avoid cracks during pressure build up. CO_2 is pumped into the extractor to a pressure above its critical pressure. Before entering the extraction, CO_2 is heated to a temperature above its critical temperature. During drying, the flow of CO_2 to the extractor is constant, 0.54 kg/h, and controlled independently of pressure. In the separator, the solvent is separated from carbon dioxide. After 5 h, when the solvent is completely replaced, the pressure is slowly reduced ($\Delta P/\Delta t$ = 3 bar/min) to ambient pressure.

2.3. Characterization

The dried gels were then characterized. The powders were inspected with scanning electron microscopy (SEM) and transmission electron microscopy (TEM). The specific surface was measured using the BET method and X-ray powder diffraction patterns were taken. The crystallite size of $BaTiO_3$ was estimated using the Scherrer equation, from the (200) diffraction peak. The surface of powders eroded with argon and the impurities concentration depth profiles were analyzed using Auger electron spectroscopy (AES). The erosion rate was 1 nm/min. In addition, the shrinkage of the samples, prepared from both powders, was determined and the microstructure of polished and etched samples was investigated.

3. Results and discussion

Fig. 2 shows typical TEM images of the dried $BaTiO_3$ powders A and B. It can be seen that the synthesized powder is composed of crystallites whose size can be measured in nanometers.

In Fig. 3 the images of dried powders A (dried in air) and B (dried with SC CO_2) taken with a SEM are shown. In a comparison of both images one can see that powder A, which was dried in air, is more agglomerated.

The X-ray powder diffraction patterns of dried powders and of calcined powders A and B

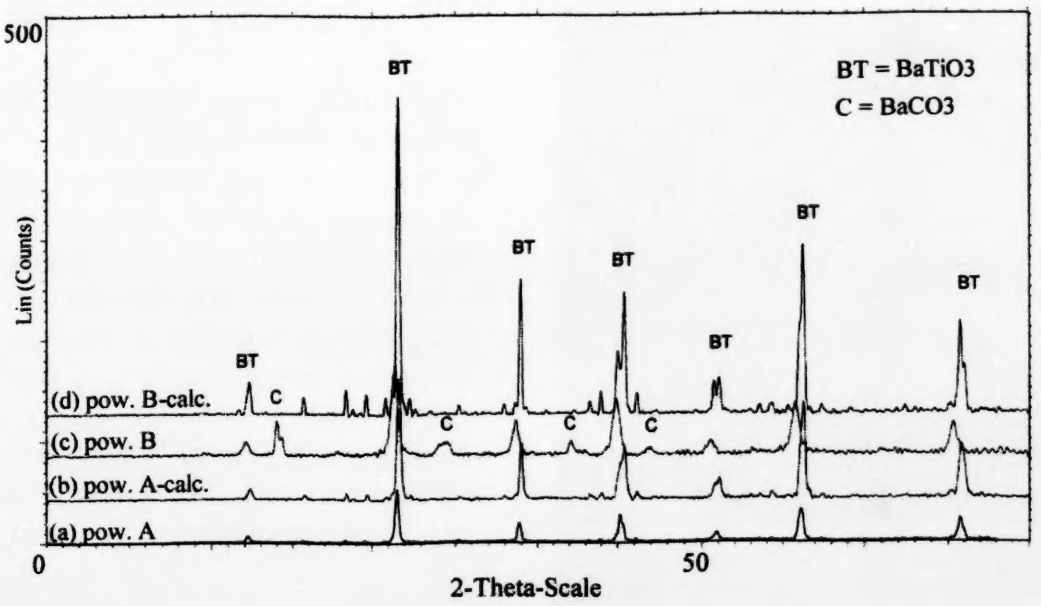

Fig. 4. X-ray diffraction patterns of synthesized $BaTiO_3$ powders; (a) powder A, dried in air, (b) calcined powder A, (c) powder B, dried with CO_2 and (d) calcined powder B.

are shown on Fig. 4. The X-ray diffraction pattern of powder A (dried in air and calcined) shows only the diffraction peaks of $BaTiO_3$, whereas the diffraction pattern of powder B (dried in SC CO_2) shows also the diffraction peaks of $BaCO_3$, which disappear after the calcination.

The $BaTiO_3$ crystallite size was determined by the Scherrer relation:

$$d_x = 0.94\lambda/\beta \cos\theta \quad (1)$$

where λ (1.5406 Å) is the characteristic wavelength, β is the true half peak width and θ half the diffraction angle of the centroid of the peak (in degrees).

The size of the crystallites obtained from the Scherrer equation is larger than that estimated from the specific surface area (S) for both powders. The differences in the average size between d_x and that obtained from the specific surface d_s, ($d_s = 6V_m/S$, where V_m is mole volume of $BaTiO_3$ and (S) is the measured specific surface) appear when the shapes of the crystallites can not be taken as perfect spheres.

After the calcination of powders A and B at 1100°C their specific surface decreases drastically from more than a hundred to some few square meters per gram (Tables 1 and 2). During the calcination the dense agglomerates are formed. In Fig. 5 the SEM images of calcined powders A and B are shown and it can be visually estimated that the average size of the agglomerates is around 150 nm for both powders.

However, when we estimate the size of the particles from the specific surface of powders A

Table 1
The specific surface area (S) and the average grain size d_x and d_s obtained from the diffraction data and from the specific surface measurements, respectively

Sample code	S (m^2/g)	d_x (nm)	d_s(nm)
Powder A	136.6	15.4	7.3
Powder B	147.5	16.6	6.7

Table 2
The specific surface area (S) of powders A and B calcined at 1100°C and the average grain size of particles estimated from the Scherrer relation and from the specific surface area, respectively

Sample code	S (m^2/g)	d_x (nm)	d_s (nm)
Powder A	6.4	50.3	155
Powder B	4.3	17.3	160

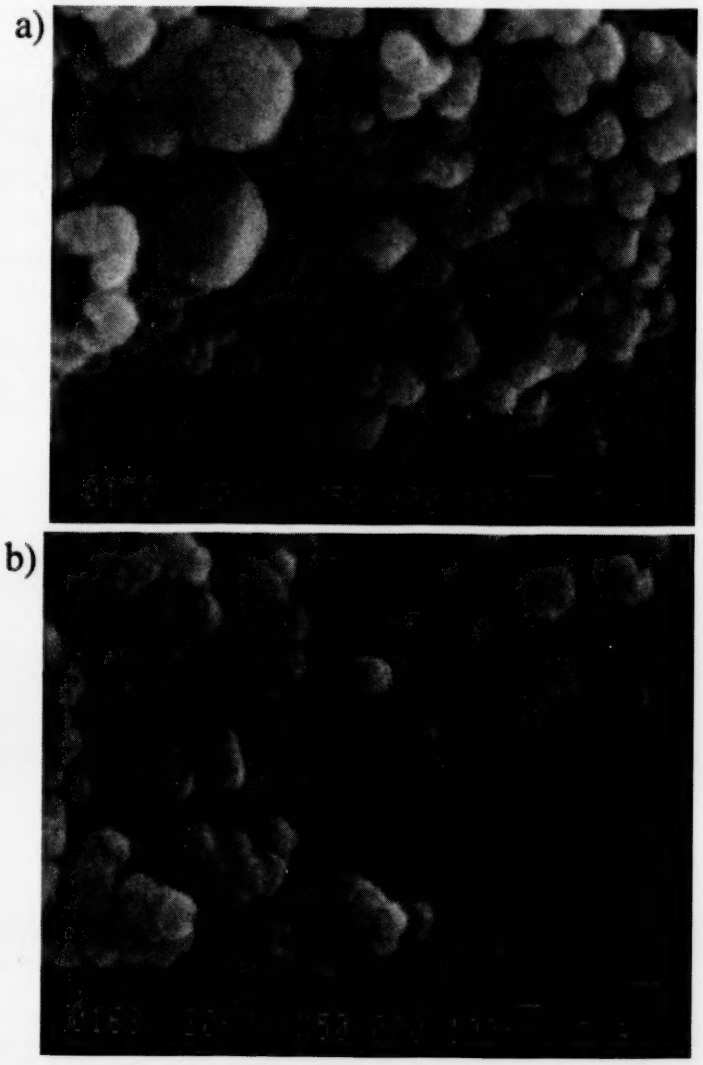

Fig. 5. SEM images of powders calcined at 1100°C for 2 h: (a) powder A obtained by drying of gels in air; (b) powder B dried by supercritical CO_2.

and B (Table 2), a similar value to the average grain size determined from the SEM images of calcined powders (Fig. 5a and b) is observed. On the other hand, the average crystallite size obtained from the powder diffraction data are 17.3 nm for powder A and 50.3 nm for powder B. On the basis of these findings it can be concluded that the calcined powders A and B are composed of dense agglomerates, which are composed of much smaller $BaTiO_3$ crystallites.

Both powders have a low tap density, approximately 0.97 g/cm^3 for powder A and 0.45 g/cm^3 for powder B. From powders A and B, pellets with a raw density of 45 and 50% respectively, were prepared by pressing the powder with a pressure of about 10^8 Pa. Both powders exhibited bad compressibility due to a low tap density.

In Fig. 6 the shrinkage and the shrinkage rate spectra of samples A and B during sintering are shown. Sample A shows the maximum shrinkage rate at 1200°C and a final shrinkage of 40%, while sample B shows a maximum shrinkage rate at 1229°C and a final shrinkage of 37%.

The final density of the samples after sintering in air, with respect to the theoretical density, was 95% for sample A and 91% for sample B. The microstructures of the samples after sintering are shown in Fig. 7a and b. The samples show a relatively dense microstructure with an average grain size of 40–50 μm for samples A and 10–20 μm for samples B. The difference in the final grain size is associated with the initial powder properties and could be explained in terms of the powder preparation procedure.

For $BaTiO_3$, discontinuous grain growth is the main process of microstructure development. In this process, a small fraction of the grains in a matrix of similar grains outgrow on account of neighboring grains. For this discontinuous grain growth to occur, firstly nucleus grains must be formed, which then grow much faster in comparison to the other grains in the matrix [5]. The final microstructure depends to a large extent on the number of these nucleus grains.

In the case of powder A, the impurities, i.e. the disintegration products formed during gelation, are deposited on the grain surface of powders A before the sintering. Because of this, the grain growth during sintering is retarded since the mass transport between the neighboring grains is hindered. This has a consequence that less grains outgrow in the larger nucleus grains. The smaller number of large grains, which might act as nucleus grains and grow on account of other neighboring grains, has the consequence that the final grain size is large, Fig. 7a. In the case of powder B, the grain surface is less contaminated as a result of drying in supercritical carbon dioxide. CO_2 dissolves and washes away the organic disintegration products formed dur-

ing gelation, which would otherwise retard the grain growth and/or the formation of the nucleus grains. A greater number of larger grains that might outgrow in the nucleus grains has the consequence that the final grain size is smaller, Fig. 7b.

The investigation of the grain surfaces of powders A and B by Auger electron microscopy (AEM) confirms such an explanation. Powder A contains more carbon rich impurities on the grain surfaces, which are the remains of the disintegration products formed during the gelation and drying, Fig. 8a. The amount of carbon rich disintegration products on the grain surfaces of powder B is smaller Fig. 8b, i.e. the concentration profile of carbon vs. the ionic erosion is smaller.

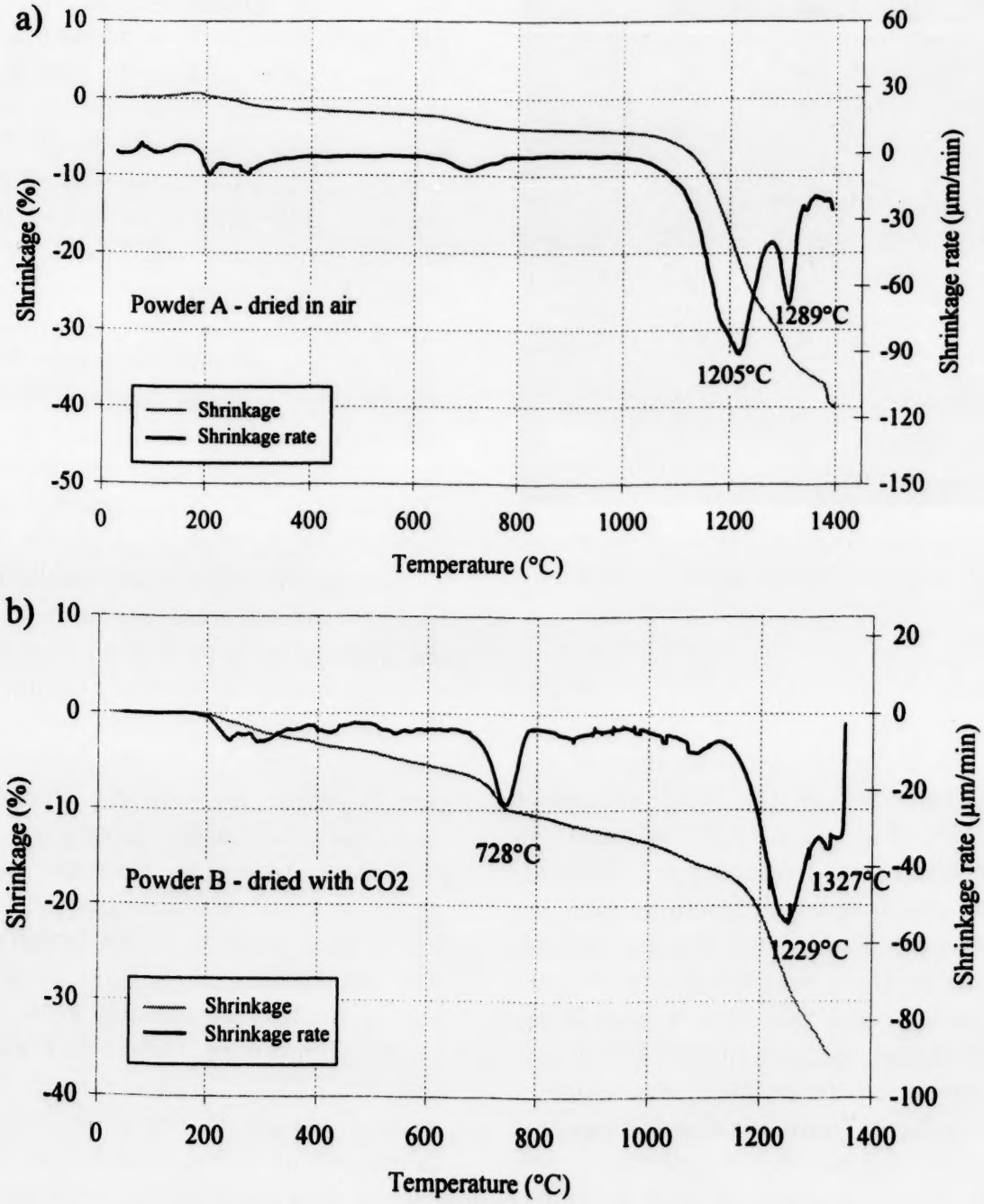

Fig. 6. The shrinkage spectra of powders: (a) powder A obtained by drying of gels in air; (b) powder B dried by supercritical CO_2.

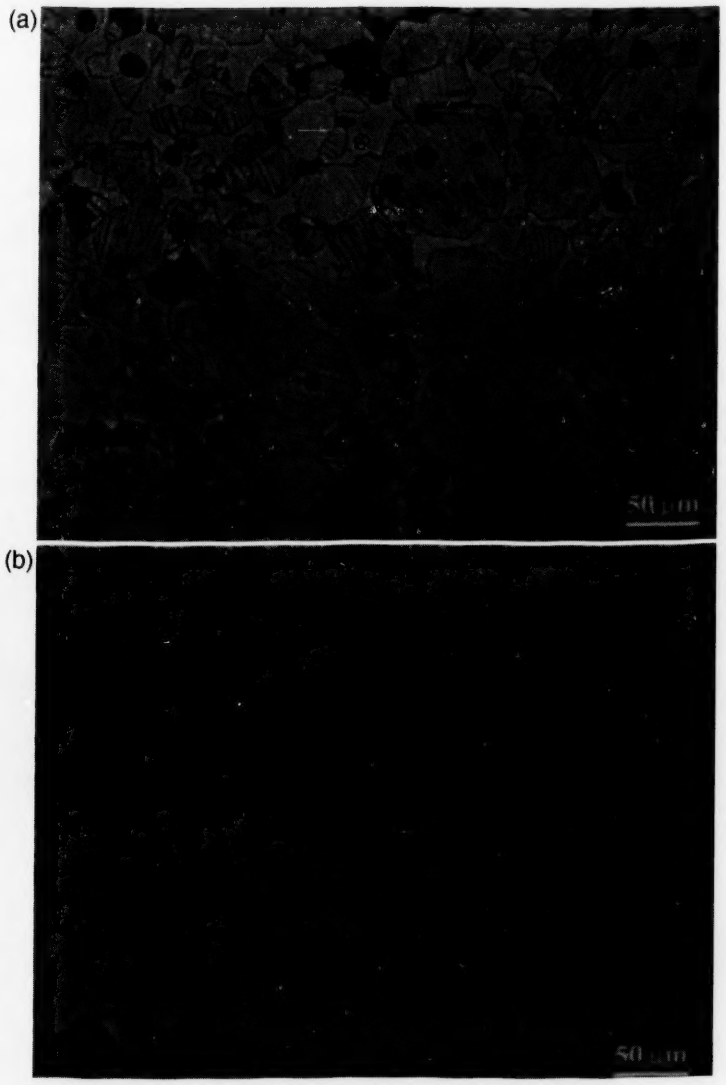

Fig. 7. Microstructure of $BaTiO_3$ powders: (a) dried in air; (b) dried by supercritical CO_2.

4. Conclusions

The investigations have shown that there is a link between the method of drying the gels, the powder properties and the microstructure development. The differences in the morphology of the powders due to the preparation technique influence the microstructure development during the sintering of $BaTiO_3$ powders. The application of supercritical CO_2 during the treatment of the gels of $BaTiO_3$ was found to be effective. However, CO_2 reacts with unreacted BaO and forms ingredients of $BaCO_3$. Thus, the use of some other supercritical fluid, which does not react with BaO, would in this case be more convenient.

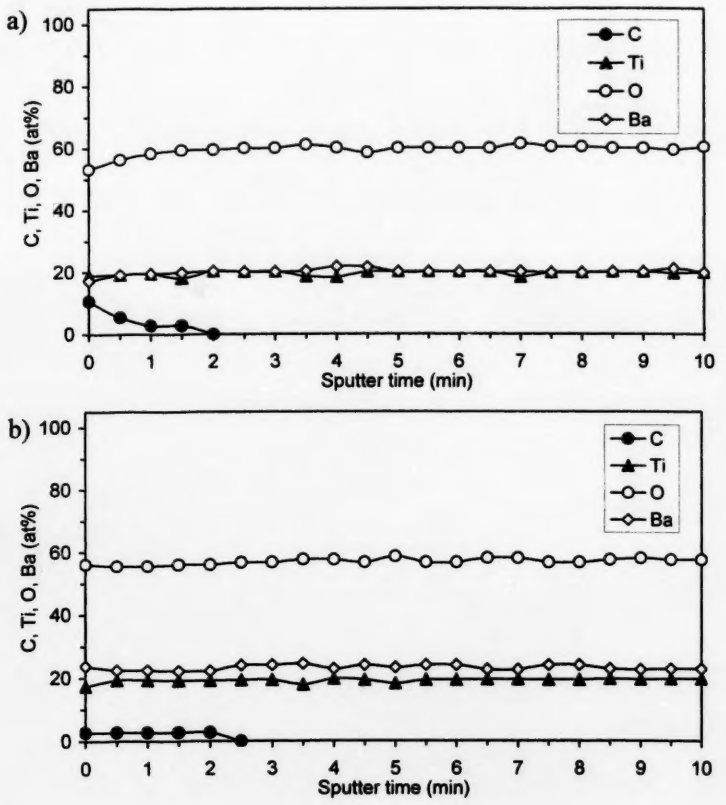

Fig. 8. Concentration depth profile of carbon on the surface of powders: (a) powder A; (b) powder B.

Acknowledgements

The authors would like to thank B. Pracek for the AES analyses.

References

[1] D. Hennings, S. Schreinemacher, Characterization of hydrothermal barium titanate, J. Eur. Ceram. Soc. 9 (1992) 41.
[2] P. Nanni, M. Leoni, V. Buscaglia, G. Aliprandi, Low-temperature aquenous preparation of barium metatitanate powders, J. Eur. Ceram. Soc. 14 (1994) 85.
[3] S. Urek, M. Drofenik, The hydrothermal synthesis of $BaTiO_3$ fine particles from hydroxide-alkoxide precursors, J. Eur. Ceram. Soc. 18 (1998) 279.
[4] Z. Novak, Z. Knez, Diffusion of methanol–liquid CO_2 and methanol-supercritical CO_2 in silica aerogels, J. Non-Cryst. Solids 221 (1997) 163.
[5] W.D. Kingery, Introduction to Ceramics, Wiley, New York, 1960.

ELSEVIER

Journal of Supercritical Fluids 19 (2001) 217

THE JOURNAL OF Supercritical Fluids

www.elsevier.com/locate/supflu

Calendar

2001

Ninth International Conference on Properties and Phase Equilibria for Product and Process Design

May 20–25, 2001, Kurashiki/Kyoto, Japan
For further information contact:
Prof. Y. Miyano
Kurashiki University of Science and the Arts,
Department of Chemical Technology, 2640
Tsurajima-cho, Kurashiki 712-8505, Japan;
Tel: 8186 440 1069;
Fax: 8186 440 1062;
Webpage: http://www.kusa.ac.jp/chemconf/

* *Indicates a new entry*

Organizers of relevant meetings are invited to send details at an early stage, to ensure inclusion in the Calendar. This information should be sent to the Editor, or more preferentially directly to: Dr R. H. van den Berg. Elsevier Science B.V., Chemistry & Chemical Engineering Department, P.O. Box 330, 1000 Ah Amsterdam, The Netherlands

VOLUME V OF THE EXPERIMEMENTAL THERMODYNAMICS SERIES

Equations of State for Fluids and Fluid Mixtures

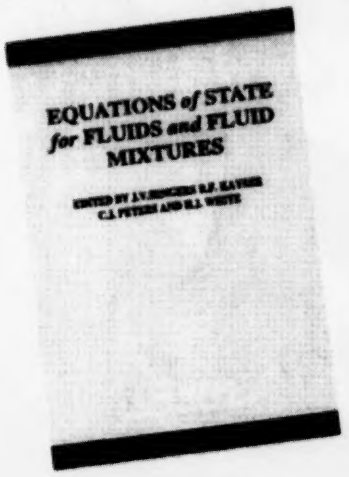

CONTENTS direct

Sign up today for **ContentsDirect**, the free e-mail service which delivers Elsevier Science book and journal tables of contents directly to your PC. Register online at:
www.elsevier.nl/locate/contentsdirect

ELSEVIER
an imprint of
Elsevier Science

Edited by
J.V.Sengers, *University of Maryland, MD, USA*
R.F. Kayser, *National Institute of Standards & Technology, MD, USA*
C.J. Peters, *Delft University of Technology, The Netherlands*
H.J. White Jr., *University of Maryland, MD, USA*

This book has been prepared under the auspices of Commission I.2 on Thermodynamics of the International Union of Pure and Applied Chemistry (IUPAC). The authors of the 18 chapters are all recognized experts in the field with the result that the book gives an up-to-date presentation of equations of state for fluids and fluid mixtures.

All principal approaches for developing equations of state are covered. The theoretical basis and practical use of each type of equation is discussed and the strengths and weaknesses of each are addressed. Topics addressed include the virial equation of state, cubic equations and generalized van der Waals equations, perturbation theory, integral equations, corresponding stated and mixing rules. Special attention is also devoted to associating fluids, polydisperse fluids, polymer systems, self-assembled systems, ionic fluids and fluids near critical points.

Equations of State for Fluids and Fluid Mixtures will be of interest to post graduate researchers in the fields of chemical engineering, mechanical engineering, chemistry and physics.

For further information, including a comprehensive contents list, visit the book's homepage at:
www.elsevier.com/locate/isbn/0444503846

Publication: October 2000
Hardbound, 928 pages (in 2 volumes)

ISBN: 0-444-50384-6
Price: NLG 525 (euro238.23) US$275

ORDER FORM

☐ Please send me ____ copy (ies) of **Equations of State for Fluids and Fluid Mixtures**
(ISBN: 0-444-50384-6) at NLG525 (euro238.23) / US$275

Order value subtotal NLG/US$ _____

Non-UK EU (European Union) residents must either:

State VAT number here _____

Or add VAT (or your countryis equivalent) @ _____ %

Total NLG/US$ _____

Name *(please print)* _____

Position _____

Department _____

Organisation _____

Address _____

Region/State _____

Post/Zip Code _____ Country _____

Tel _____ Fax _____

E-mail _____

NLG (Dutch Guilder) prices apply to customers in Europe and Japan. US$ prices apply to customers in all other countries. Prices and proposed publication dates are subject to change without prior notice

PAYMENT DETAILS

☐ Please send me a pro forma invoice.

☐ Cheque/bank draft/UNESCO coupon enclosed made payable to *Elsevier Science.*

☐ I wish to pay be credit card (accepted up to a maximum value of US$5,000.00/NLG 10,000.00). Your credit card will be debited including VAT when applicable.

☐ Visa ☐ American Express ☐ MasterCard

Issuing Bank *(for MasterCard only)* _____

Card No. _____

Exp. Date _____

Signature _____

Date _____

SEND YOUR ORDER TO:

For customers in the Americas:
Elsevier Science
PO Box 945, New York,
NY 10159-0945, USA
Tel: (+1) 212 633 3730
Fax: (+1) 212 633 3680
Toll-free for customers in the USA and Canada:
1-888-437-4636 3432
E-mail: usinfo-f@elsevier.com

For customers in other locations:
Elsevier Science
Marketing Department,
PO Box 211,
1000 AE Amsterdam,
The Netherlands
Tel: (+31) 20 485 3757
Fax: (+31) 20 485 3432
E-mail: nlinfo-f@elsevier.nl

☐ Please send me information about Elsevier and its products that may interest me.

☐ Please send me information about third parties whose products may interest me.

In all correspondence please quote reference
030-024-0

The FREE e-mail service which delivers Elsevier Science book and journal tables of contents directly to your PC

CONTENTS direct

Sign-up is simple!

1. ALL YOU HAVE TO DO IS VISIT THE CONTENTSDIRECT WEBSITE
2. FOLLOW THE INSTRUCTIONS TO REGISTER YOUR BOOK AND JOURNAL INTERESTS ONLINE
3. THEN SIT BACK AND ENJOY ADVANCE E-MAIL NOTIFICATION OF THE VERY LATEST RESEARCH IN YOUR AREAS OF INTEREST

REGISTER TODAY

www.elsevier.com/locate/contentsdirect

media@elsevier.co.uk

DISPLAY ADVERTISING

PRESENT YOURSELF STRAIGHT TO YOUR MARKET

Display advertising provides an interface between the commercial market and the scientific community. Offering an ever expanding range of services to enable the commercial sector to open up communication channels with potential customers and increase sales, we aim to provide the best possible means at cost effective prices.

Using display advertising to promote your products or services can:

- **Raise Market Awareness**
- **Enhance Brand Reputation**
- **Reach a Key Audience of Opinion Formers and Decision Makers**
- **Provide Association with Leading Research Publications**
- **Supply Exposure to International Readerships**

All Elsevier Science titles accept display advertising. For more information about how to promote your companies products or services in this, or any other journal please contact the address below.

CONTACT:

THE ADVERTISING DEPARTMENT
ELSEVIER SCIENCE
The Boulevard
Langford Lane
Kidlington
Oxford
OX5 1GB, UK
TEL: (44) 1865 843565
FAX: (44) 1865 843976

Email: media@elsevier.co.uk

ELSEVIER
SCIENCE

Choose from broad collections of primary journal literature and powerful secondary databases, all deliverable via the Internet or your local Intranet—building blocks for the digital library you need.

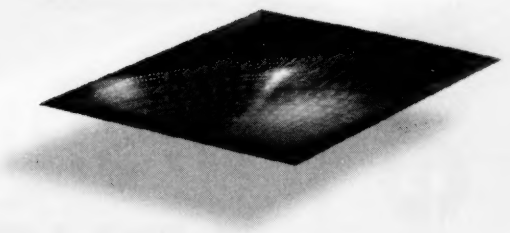

SCIENCE DIRECT®

For the Digital Library You Want

ScienceDirect offers desktop access to over 1 million articles published in nearly 1,200 journals spanning 16 fields of science and provides researchers with some 2 million bibliographic citations and abstracts. Access may also be provided to an additional 30 million abstracts via ScienceDirect's secondary databases.

Unprecedented content, navigability and customization options
Whether you choose the breadth of the ScienceDirect multi-publisher platform or one of our discipline or industry-focused solutions, you'll be providing your institution with a dynamic, efficient and integrated solution to access the world's critical STM literature.

- ScienceDirect Online
- ScienceDirect OnSite
- ScienceDirect Web editions
- ScienceDirect Gateway
- ScienceDirect Bibliographic Database Collection
- ScienceDirect Industry Solutions: Pharmaceutical
- ADONIS®
- ScienceServer®

www.sciencedirect.com

NEW YORK
+1 212 633 3809
usinfo@sciencedirect.com

AMSTERDAM
+31 20 485 3767
nlinfo@sciencedirect.com

SINGAPORE
+65 434 3716
sginfo@sciencedirect.com

TOKYO
+81 3 5561 5035
jpinfo@sciencedirect.com

RIO DE JANEIRO
+55 21 509 5340
brinfo@sciencedirect.com

0 097 056 1

INSTRUCTIONS TO AUTHORS

Submission of Manuscripts
Please submit the original and three copies of your manuscript to either the Editor-in-Chief, Dr. Erdogan Kiran, Department of Chemical Engineering, Virginia Tech, 133 Randolph Hall, Blacksburg, VA 24061-0211, USA; or to the Regional Editor, Dr. Gerd Brunner, Technische Universitaet Hamburg-Harburg, Arbeitsbereich Termische Verfahrenstechnik, Eissendorfer Strasse 38, D-21073 Hamburg, Germany. Instructions for the preparation of compuscripts are published in the Journal of Supercritical Fluids 11 (1997) 135. Enclose the original illustrations and three sets of copies. Submission of an article is understood to imply that the article is original and unpublished and is not being considered for publication elsewhere. Upon acceptance of an article by the journal, the author(s) will be asked to transfer the copyright of the article to the publisher. This transfer will ensure the widest possible dissemination of information.

Manuscript Preparation
The official language is English. The manuscript should be typewritten with double spacing and wide margins and start with the title followed by the name(s) of the author(s), their affiliations and an abstract of less than 500 words. An abstract is not requested for brief notes. IUPAC guidelines should be followed for terminology and choosing symbols and units as much as possible.

Illustrations
Illustrations should be numbered consecutively and referred to in the text. Drawings should be in a form suitable for reproduction, drawn in Indian ink on drawing paper or tracing paper. They should be completely lettered, the size of the lettering being appropriate to that of the drawings, but taking into account the possible need for reduction in size of 50%. The page format of the journal should be considered in designing the drawings. Photographs must be of good quality, printed on glossy paper. Figure captions should be supplied on a separate sheet.
Detailed suggestions and instructions to authors are published in the Journal of Supercritical Fluids 14 (1998) 83–86. A free reprint is available from the publisher upon request. (The instructions can also be found on the World Wide Web: access under http://www.elsevier.nl or http://www.elsevier.com)

Proofs
Proofs will be sent to the author, to be checked for printer's errors. in case of two or more authors please indicate to whom the proofs should be sent.

Reprints
Fifty reprints of each article will be supplied free of charge. Additional reprints can be ordered by the authors. An order form containing price quotations will be sent to the authors together with the proofs.

Electronic manuscripts. Electronic manuscripts have the advantage that there is no need for the rekeying of text, thereby avoiding the possibility of introducing errors and resulting in reliable and fast delivery of proofs. For the initial submission of manuscripts for consideration, hardcopies are sufficient. For the processing of **accepted papers,** electronic versions are preferred. After **final acceptance,** your disk plus three final and exactly matching printed versions should be submitted together. Double density (DD) or high density (HD) diskettes (3.5 or 5.25 inch) are acceptable. It is important that the file saved is in the native format of the word processor program used. Label the disk with the name of the computer and word-processing package used, your name, and the name of the file on the disk. Further information may be obtained from the Publisher.

Authors in Japan please note: Upon request, Elsevier Science Japan will provide authors with a list of people who can check and improve the English of their paper (*before submission*). Please contact our Tokyo office: Elsevier Science Japan, 1-9-15 Higashi-Azabu, Minato-ku, Tokyo 106-0044; Tel. (03)-5561-5032; Fax (03)-5561-5045. **Author enquiries:** For enquiries to the submission of articles (including electronic submission), the status of accepted articles through our Online Article Status Information System (OASIS), author Frequently Asked Questions and any other enquiries relating to Elsevier Science, please consult http://www.elsevier.com/locate/authors/

For specific enquiries on the preparation of electronic artwork, consult http://www.elsevier.com/locate/authorartwork/

Contact details for questions arising after acceptance of an article, especially those relating to proofs are provided when an article is accepted for publication

Advertising information. Advertising orders and enquiries can be sent to: **USA, Canada and South America:** Mr Tino DeCarlo, The Advertising Department, Elsevier Science Inc., 655 Avenue of the Americas, New York, NY 10010-5107, USA; phone: (+1) (212) 633 3815; fax: (+1) (212) 633 3820; e-mail: t.decarlo@elsevier.com. **Japan:** The Advertising Department, Elsevier Science K.K., 9-15 Higashi-Azabu 1-chome, Minato-ku, Tokyo 106-0044, Japan; phone: (+81) (3) 5561 5033; fax: (+81) (3) 5561 5047. **Europe and ROW:** Rachel Leveson-Gower, The Advertising Department, Elsevier Science Ltd. The Boulevard, Langford Lane, Kidlington, Oxford OX5 1GB, UK; phone: (+44) (1865) 843565; fax: (+44) (1865) 843976; e-mail: r.leveson-gower@elsevier.co.uk.

USA mailing notice: *Journal of Supercritical Fluids* (ISSN 0896-8446) is published nine times a year by Elsevier Science B.V. (P.0 Box 211, 1000 AE Amsterdam, The Netherlands). Annual subscription price in the USA US$656.00 (valid in North, Central and South America), including air speed delivery. Application to mail at periodical postage rate is pending at Jamaica, NY 11431.

USA POSTMASTER: Send address changes to *Journal of Supercritical Fluids*, Publications Expediting Inc., 200 Meacham Ave, Elmont, NY 11003

AIRFREIGHT AND MAILING in the USA by Publications Expediting Inc., 200 Meacham Ave, Elmont, NY 11003

***The Journal of Supercritical Fluids* has no page charges**

♻ The paper used in this publication meets the requirements of ANSI/NISO Z39.48-1992 (Permanence of Paper).

Printed in The Netherlands

THE JOURNAL OF SUPERCRITICAL FLUIDS

VOL. 19 NO. 2 **FEBRUARY 2001**

CONTENTS

(Abstracted/indexed in: Chemical Abstracts; Current Contents: ET&AS; Current Contents: PC&ES; Drexel Polymer Notes, Engineered Materials Abstracts; Polymer Contents)

Thermodynamics, Phase equilibria, Solubility

Comparison of the performance of the LCVM model (an EoS/G^E model) and the PHCT EoS (the Perturbed Hard Chain Theory Equation of State) in the prediction of the Vapor–Liquid Equilibria of binary systems containing light gases
C.J. Boukouvalas, K.G. Magoulas, D.P. Tassios and I. Kikic 123

High-pressure solubility data of the system resveratrol (3) + ethanol (2) + CO_2 (1)
A. Berna, A. Cháfer and J.B. Montón 133

Reactions

Enzymatic alcoholysis of palm kernel oil in *n*-hexane and $SCCO_2$
D. Oliveira and J.V. Oliveira 141

Extractions

Mathematical modeling of extraction of egg yolk oil with supercritical CO_2
W. Wu and Y. Hou 149

Modeling and simulation of the supercritical CO_2 extraction of vegetable oils
E. Reverchon and C. Marrone 161

Polymers

Incorporation of disperse dye in *N*,*N*-dimethylacrylamide modified poly(ethylene terephthalate) fibers with supercritical CO_2
W.L.F. Santos, M.F. Porto, E.C. Muniz, N.P. Povh and A.F. Rubira 177

Solubilities and diffusion coefficients of carbon dioxide in poly(vinyl acetate) and polystyrene
Y. Sato, T. Takikawa, S. Takishima and H. Masuoka 187

Attempt to explain the changes in solvation of polystyrene in supercritical CO_2/ethanol mixtures using infrared and Raman spectroscopy
P. Lalanne, S. Rey, F. Cansell, T. Tassaing and M. Besnard 199

Materials synthesis

Synthesis of barium titanate using supercritical CO_2 drying of gels
Z. Novak, Z. Knez, I. Ban and M. Drofenik. 209

Calendar 217

CONTENTS direct

This journal is part of **ContentsDirect**, the ***free*** alerting service which sends tables of contents by e-mail for Elsevier Science books and journals. You can register for **ContentsDirect** online at: **www.elsevier.nl/locate/supflu**

0896-8446(200102)19:2;1-2